

Physics and Application of Plasmas Based on Pulsed Power Technology

Edited by Eiki Hotta and Tetsuo Ozaki

December 21-22, 2010
National Institute for Fusion Science
Toki, Gifu, Japan

Abstract

The papers presented at the symposium on “Physics and Application of Plasmas Based on Pulsed Power Technology” held on December 21-22, 2010 at National Institute of Fusion Science are collected. The papers in this proceeding reflect the current status and progress in the experimental and theoretical researches on high power particle beams and high energy density plasmas produced by pulsed power technology.

Keyword: high power particle beams, high energy density plasma, pulsed power technology, z-pinch, soft x-ray, EUV, x-ray laser, pulsed discharge, high power micro wave, material processing, medical application

Preface

The symposium entitled “Physics and Application of Plasmas Based on Pulsed Power Technology” was organized as a part of the General Collaborative Research of National Institute for Fusion Science (NIFS) and held on December 21-22, 2010 at NIFS, Toki.

In the symposium, 23 papers were presented in two days, of which 22 papers are reported in this proceeding. The total number of participants was 47 including students and researchers from universities and companies.

The main objective of the symposium is to provide a place of discussion about the pulsed power technology, generation of plasmas by using pulsed power technology and its application. Therefore, the papers in this proceeding reflect the current status and progress in the experimental and theoretical researches on high power particle beams and high energy density plasmas produced by pulsed power technology in Japan. It is our great pleasure with the unexpectedness if the symposium was beneficial to the development of pulsed power technology.

We would like to express our sincere thanks to all of the participants, the authors and the staff of NIFS.

Thank you very much.

Eiki Hotta
Department of Energy Sciences
Tokyo Institute of Technology

Tetsuo Ozaki
National Institute for Fusion Science

List of Participants

K. Takaki	Iwate University
I. Yagi	Iwate University
H. Aoki	Iwate University
S. Ihara	Saga University
W. Jiang	Nagaoka University of Technology
G. Imada	Niigata Institute of Technology
K. Satoh	Niigata Institute of Technology
M. Onda	Niigata Institute of Technology
T. Kikuchi	Nagaoka University of Technology
S. Furuya	Gunma University (Present: Saitama Institute of Technology)
N. Tashiro	Gunma University
K. Masugata	University of Toyama
H. Ito	University of Toyama
H. Yamamoto	University of Toyama
Y. Ochiai	University of Toyama
H.M. Liu	Toyama University
T. Kawamura	Tokyo Institute of Technology
T. Ozawa	Tokyo Institute of Technology
K. Kamada	Kanazawa University
R. Ando	Kanazawa University
Y. Soga	Kanazawa University
K. Nose	Kanazawa University
K. Misawa	Kanazawa University
S. Yanagi	Kanazawa University
K. Kato	Kanazawa University
T. Kitamura	Kanazawa University
N. Yamada	Kanazawa University
M. Kato	Kanazawa University
T. Mimura	Kanazawa University
K. Horioka	Tokyo Institute of Technology
H. Sakai	Tokyo Institute of Technology
Y. Ogata	Tokyo Institute of Technology
A. Nakayama	Tokyo Institute of Technology

Y. Kuroda	Tokyo Institute of Technology
K. Takasugi	Nihon University
M. Nishio	Nihon University
H. Sakuma	Nihon University
M. Iwata	Nihon University
E. Hotta	Tokyo Institute of Technology
H. Kumai	Tokyo Institute of Technology
J. Li	Tokyo Institute of Technology
A. Tokuchi	Pulse Power Technology Lab.
T. Tazima	National Institute for Fusion Science
T. Ozaki	National Institute for Fusion Science
H. Akiyama	Kumamoto University
M. Akiyama	Kumamoto University
T. Ihara	Kumamoto University

Contents

Mechanism of Destruction on Ice Breaking Using Pulsed Power S. Ihara, Y. Kominato, K. Fukuda (Saga University), and S. Ushio (National Institute of Polar Research)	1
Experimental Study on Underwater Shock Wave Generated by Using Pulse Power Technology H. Yamamoto, Y. Nakaya, H. Ito, and K. Masugata (University of Toyama)	5
Discharge Phenomena in Supercritical Carbon Dioxide T. Ihara, T. Kiyon, S. Katsuki, M. Hara, and H. Akiyama (Kumamoto University)	9
Production of Metal Contained Carbon Plasma Using Shunting Arc Discharge for Composite Film Preparation H. Aoki, K. Takahashi, and K. Takaki (Iwate University)	13
Application of Triboluminescence to Roentgen Diagnosis N. Tashiro and S. Furuya (Saitama Institute of Technology)	18
Laser Target using Continuous Supersonic Jet Y. Ogata, K. Takahashi (Tokyo Institute of Technology), H. Kuwabara (IHI Corporation), M. Nakajima, and K. Horioka (Tokyo Institute of Technology)	22
Ion Acceleration Independent of the Direction of Electric Currents in Gas-puff Z-pinch M. Nishio, K. Takasugi, and H. Sakuma (Nihon University)	26
Characteristics of Nano-second Pulsed Discharge Using All Solid State Pulsed Power Generator I. Yagi, K. Takaki (Iwate University), T. Namihara (Kumamoto University), and R. Ono (The University of Tokyo)	30

Electrical Conductivity Measurements of Warm Dense Matter with Semi-rigid Vessel	36
H. Sakai, K. Iwasaki, M. Nakajima, T. Kawamura, and K. Horioka (Tokyo Institute of Technology)	
Pulsed Power Generator Using Solid-State LTD Modules	40
W. Jiang and A. Tokuchi (Nagaoka University of Technology)	
Development of MOS-FET Based Marx Generator with Self-Proved Gate Power	43
A. Tokuchi (Pulsed Power Japan Laboratory Ltd.), W. Jiang (Nagaoka University of Thechnology), K. Takayama, T. Arai, T. Kawakubo, and T. Adachi (High Energy Accelerator Research Organization (KEK))	
Design of Bragg Resonator for Free Electron Maser	48
K. Nose, K. Misawa, S. Yanagi, K. Kato, T. Kitamura, N. Yamada, Y. Soga, K. Kamada (Kanazawa University), M. Yoshida (High Energy Accelerator Research Organization), and N.S. Ginzburg (Institute of Applied Physics, Russian Academy of Science)	
Development of 100 GHz Interdigital Backward-Wave Oscillator	54
M. Kato, Y. Soga, T. Mimura, Y. Kato, K. Kamada (Kanazawa University), and M. Yoshida (High Energy Accelerator Research Organization)	
Longitudinal Bunch Compression Study with Induction Voltage Modulator	59
A. Nakayama, Y. Miyazaki (Tokyo Institute of Technology), T. Kikuchi (Nagaoka University of Technology), M. Nakajima, and K. Horioka (Tokyo Institute of Technology)	
Theoretical Study on Population Inversion of Hydrogen-like Nitrogen in Recombination Plasma	63
T. Ozawa, Y. Ishizuka, H. Kumai, E. Hotta, K. Horioka, and T. Kawamura (Tokyo Institute of Technology)	

- Analysis of Highly Ionized N Plasma Spectra under the Effect of an External Magnetic Field in Fast Capillary Discharge 67
H. Kumai, Y. Ishizuka, M. Watanabe and E. Hotta (Tokyo Institute of Technology)
- Counter-facing Plasma Guns for Efficient Extreme Ultra-Violet Plasma Light Source 73
Y. Kuroda, K. Hayashi (Tokyo Institute of Technology), H. Kuwabara (IHI Corporation), M. Nakajima, T. Kawamura, and K. Horioka (Tokyo Institute of Technology)
- Characterization of the Pulsed Ion Beam in a Plasma Focus Device for Al Surface Modification 77
H.M. Liu, D.X. Cheng, H. Ito, and K. Masugata (Toyama University)
- Characteristics of an Atmospheric Pulsed DBD Plasma Jet and Its Preliminary Application for Sterilization 82
J. Li, N. Sakai, M. Watanabe, E. Hotta, and M. Wachi (Tokyo Institute of Technology)
- Treatment of Zooplankton in Water by Pulsed Power -An Effect of NaHCO_3 Additive for Micro Bubble Production- 88
K. Satoh, M. Onda, S. Sakai, and G. Imada (Niigata Institute of Technology)
- Applications of Pulsed Intense Relativistic Electron Beam to Aquatic Conservation 93
T. Kikuchi, H. Kondo, T. Sasaki (Nagaoka University of Technology), H. Moriwaki (Shinshu University), G. Imada (Niigata Institute of Technology), and N. Harada (Nagaoka University of Technology)
- Development of Exploding Wire Ion Source for Intense Pulsed Heavy Ion Beam Accelerator 99
Y. Ochiai, T. Murata, H. Ito, and K. Masugata (University of Toyama)

Mechanisms of Destruction on Ice breaking using Pulsed Power

Satoshi Ihara, Yuichi Kominato, Kazuyuki Fukuda, Shuki Ushio*

Saga University

**National Institute of Polar Research*

ABSTRACT

In this research, investigation on breaking of ice using a pulsed power generator as a navigation of ice-breaker at ice-covered ocean, was described. In these experiments, pulsed arc discharge was formed by Marx generator. In order to investigate the dependence of input energy required for ice breaking on circuit parameters of generator, the capacitance of generator was changed. The input energy for ice-breaking was calculated from waveforms of electric power. It was found that the input energy for ice-breaking decreased as the peak power increased with decrease of the capacitance of generator.

Keywords

pulsed power, ice, shock wave

1. Introduction

The development of navigation systems for icebreakers on icebound sea has been important for the advancement of natural resources production, economic activities and so on. To make possible the navigation in ice-covered ocean, an icebreaker crushes the sea ice using the force generated by the ship's mass [1-3].

In this research, investigation on ice breaking using a pulsed power as a navigation of icebreaker at ice-covered ocean was carried out. In the previous researches, the ice breaking using Marx generator has been demonstrated experimentally [4-5]. In order to reduce the energy of ice breaking, understanding mechanisms of ice breaking is required.

Generally air bubbles is one of the very important parameters for strength of ice. In this paper, experimental result on influences of air bubbles in ice were described. The energy required to break specimen of ice was obtained on ice with and without air bubbles. Furthermore crack formation inside ice was observed by high speed camera.

2. Experimental Setup

Figure 1 shows a configuration of the experimental apparatus which consists of pulsed power generator, plastic water vessel, electrodes and measuring devices. A Marx generator, with six capacitors with a capacitance of 0.22 μF , was used as a pulsed power generator. The ice sample was placed in a plastic water vessel, which was filled with tap water. Electrodes were placed at 20 mm from surface of ice specimen as shown in Fig. 2. The electrodes were made of a dielectric material (polyethylene) and metal (copper). The distance between electrodes was 45 mm.

Figure 3 shows typical specimens of ice with size of 7x7x13cm, used in the experiments. Two kinds of ice with and without bubbles as shown in Fig. 3 were tested. At thin ice specimen, specimen is destructed in only one shot of generator. The number of shot for breaking increase with thickness of specimen. Fig. 4 shows the typical broken specimen after several shots.

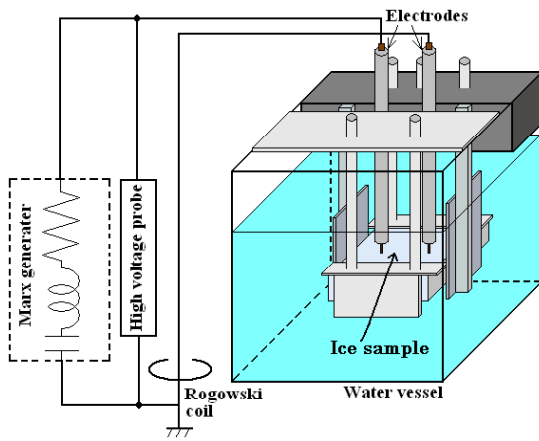


Fig. 1. Configuration of the experimental apparatus.

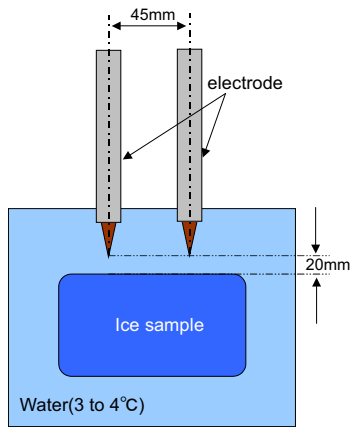


Fig. 2. Setting of ice specimen and electrodes.



(a) Clear ice



(b) Ice with bubbles

Fig. 3. Typical specimens of ice.



Fig. 4. Typical specimen broken in testing.

3. Results and Discussion

3.1 Characteristics of energy for ice breaking

Figure 5 shows characteristics of energy for ice breaking on pressure of shock wave on clear ice and ice with bubbles when the charging energy was constant. The pressure of shock wave indicated at horizontal axis was estimated from Hugoniot's equation using velocity of shock wave. It is found that the E_{ib} decreases with increase of pressure of shock wave at the both types of ice, and E_{ib} was about 0.5 times lower when the ice with bubbles was used than when the clear ice was used. The decrease of E_{ib} suggests that efficient ice breaking was realized.

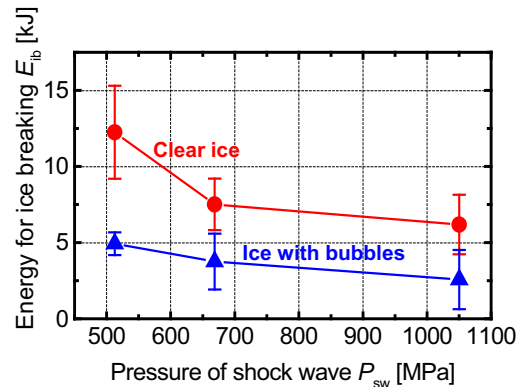


Fig. 5. Characteristics of energy for ice breaking on pressure of shock wave.

3.2 Observation of crack formation

Figure 6 shows the configuration of apparatus for taking photograph of crack formation at inside ice. High speed camera (SIMD16, Specialised Imaging Limited) was used for observation of crack.

Figure 7 show photographs and waveforms when the clear ice are used. First photograph of Fig. 7(a) shows the ice at no discharge, and photo 1, 2, 3 show the images at after 17.5, 24.0 and 30.5 μ s from onset

of discharge current, respectively. Gate pulses, which correspond to shutter timing, are shown in Fig. 7 (b) with voltage and current waveforms. In photo 1 cracks can be observed at upper side of ice, and the cracks propagated in ice.

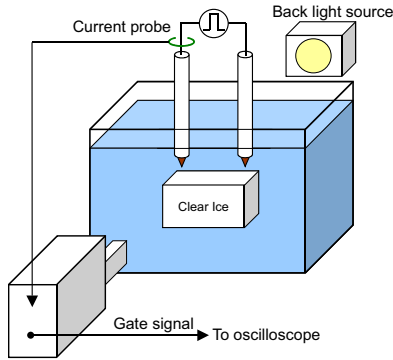
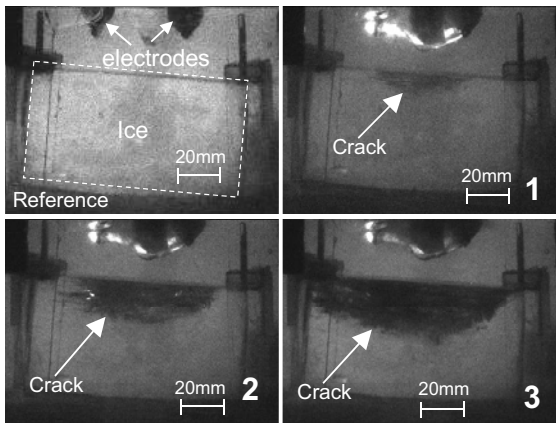
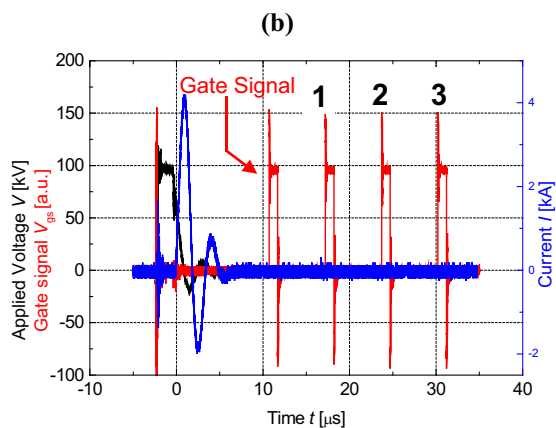


Fig. 6. Schematic diagram of apparatus for taking photograph of crack formation at inside ice.



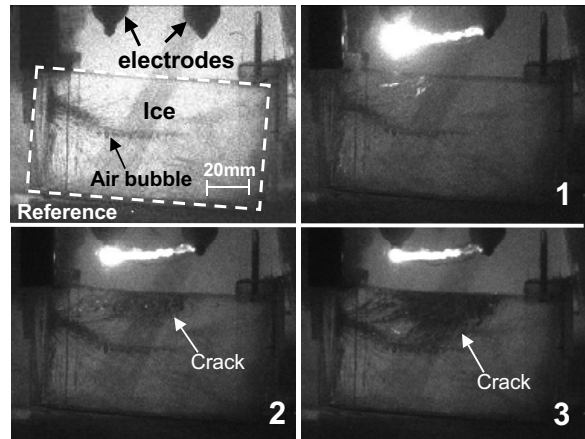
(a) Photographs of crack formation in clear ice.



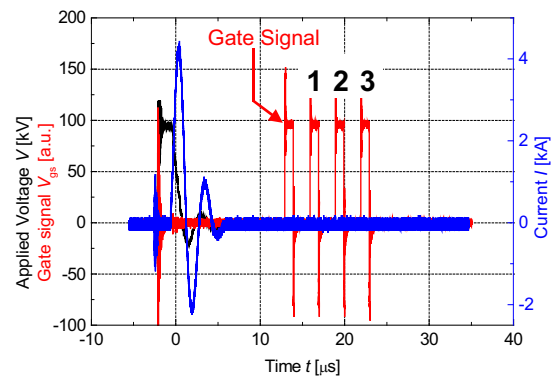
(b) Waveforms of voltage, current and gate signal of camera.

Fig. 7. Photographs and waveforms when the clear ice are used.

Figure 8 (a) and (b) show photographs of crack formation in ice with bubbles, and voltage, current and gate pulse waveforms. In photo 1 no cracks were found in ice. In photo 2 cracks can be observed, and propagated in ice. Fig. 9 shows detail of crack formation in ice. In these photos, it was found that cracks were formed along air bubbles. We can explain these phenomena as follows. When the shock wave propagates in ice, the wave refracts at air bubble. At that time the stress is applied to ice, and then the structure of ice is destructed locally, that lead to formation of cracks. It was found that crack formation is caused by air bubbles inside ice cause.



(a) Photographs of crack formation in ice with bubbles.



(b) Waveforms of voltage, current and gate signal of camera.

Fig. 8. Photographs and waveforms when the ice with bubbles are used.

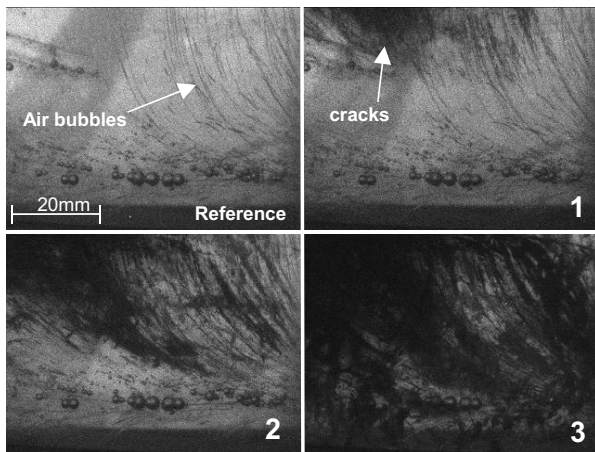


Fig. 9. Photographs and waveforms when the ice with bubbles are used.

4. Conclusions

In this research two kinds of ice, clear ice and ice with bubbles, were used to understand mechanisms of ice breaking by shock wave produced by pulsed power. It was found from results that larger energy for ice breaking was needed on clear ice than ice with air bubbles, and crack formation was caused by air bubbles.

References

- [1] K. Izumiya, A. Konno and S. Sakai: *Proc. 17th Int. Symposium Okhotsk Sea & Sea Ice*, Hokkaido, 2002, p. 267.
- [2] A. Konno and K. Izumiya: *Proc. 17th Int. Symp. Okhotsk Sea & Sea Ice*, Hokkaido, 2002, p. 275.
- [3] K. Ogiwara, N. Otsuka, K. Kanaami, S. Takahashi, K. Maida and H. Saeki: *Proc. 17th Int. Symp. Okhotsk Sea & Sea Ice*, Hokkaido, 2002, p. 290.
- [4] S. Ihara and C. Yamabe: *Jpn. J. Appl. Phys.* **42** (2003) L489.
- [5] S. Ihara and C. Yamabe: *Jpn. J. Appl. Phys.* Vol.43, No. 8A, 2004, pp. 5528-5532.

Experimental Study on Underwater Shock Wave Generated by Using Pulse Power Technology

H. Yamamoto, Y. Nakaya, H. Ito and K. Masugata

*Dep. of Electrical and Electronic Engineering, University of Toyama,
3190 Gofuku, Toyama 930-8555, Japan*

ABSTRACT

Applications of underwater shock waves have been extended to various industrial, medical and environmental fields. The underwater shock wave is easily generated by means of explosion of explosives or high voltage electric discharge in water. In order to generate the underwater shock wave with high pressure and good controllability, we have developed the underwater shock wave system utilizing the pulse power machine which consists of a Marx generator and a pulse forming line. Characteristics of the underwater shock wave generated by the pulsed electric discharge in water are studied by a polyvinyliden-difluoride pressure transducer. When the Marx generator was operated at 120 kV and the discharge gap distance was $d=7$ mm, the underwater shock with peak pressure of 122 MPa and average velocity of 2100 m/s and a half-width of 2.5 μ s was obtained at 30 mm downstream from the axis.

Keywords

Underwater shock wave, ultrasound wave, pulse power technology

1. Introduction

The subject of the generation of strong shock waves has already been of continuous interest for more than 100 years due to its important potential applications in basic and applied research related to equations of state, plasma and space physics. In a laboratory environment, there are several methods of shock wave generation, for instance, chemical explosions [1,2], laser irradiation of a target [3], the Z-pinch approach [4], and underwater electrical explosions of wires [5]. In the latter case, underwater shock waves with several tens of megapascals were generated using moderate pulsed power generators with stored energy of only several kilojoules. A high shock wave pressure in water is realized due to underwater explosion of explosives (wire) and/or quick release of high current at the high voltage electric power in water. The small compressibility of water and the relatively slight decay of a shock wave during its propagation make the shock wave attractive for various practical applications.

The pulsed power technology has been developed over the last two decades primarily for nuclear fusion and high energy density physics research. Advances in pulsed power technology have led us to a number of potential applications such as intense pulsed charged particle beam, discharge light source (EUV source), gas laser, pulsed ozonizer and exhaust gases cleaning. The developed high-voltage pulsed power generators can cause the electrical discharge breakdown in liquid medium, such as water and dielectric oil. The discharge in liquid follows some physical phenomena, such as an intense electric field at a tip of discharge column, a radical formation in discharge channel, an ultra violet radiation from discharge and a shockwave generation on boundary between plasma and liquid medium. These phenomena are very attractive for variety of industry, medical and environmental applications.

In using underwater shock wave for various applications, the control of strength and the pulse duration of the underwater shock wave are the most

important parameter. In order to generate the underwater shock wave with high pressure and good controllability, we have developed the underwater shock wave system utilizing the pulse power machine which consists of a Marx generator and a pulse forming line. In this paper, we report characteristics of the underwater shock wave measured by a polyvinyliden-difluoride pressure transducer.

2. Experimental Setup

Figure 1 shows a schematic configuration of experimental system for studies on the underwater shock wave. The system consists of a Marx generator with the stored energy of 1.65 kJ, a pulse forming line (PFL) and a stainless-steel vessel with a pair of discharge electrode for the shock wave. The Marx generator is comprised of six-stage incorporating capacitors ($C=220$ nF) charged up to 50 kV, charging resistors ($R=20$ k Ω) for the capacitors and SF₆-filled field-distortion gap switches. The PFL consists of a pair of coaxial cylinders, i.e., an inner electrode of 114 mm length by 1250 mm outer diameter and an outer electrode of 210 mm inner diameter. The designed parameters of the PFL are capacitance per unit length of 7 nF, inductance per unit length of 121 nH, characteristic impedance of 4.2 Ω , and electrical length of 45 ns. The PFL is filled with the deionized water as a dielectric and charged positively by the low inductance Marx generator with maximum output voltage of 300 kV.

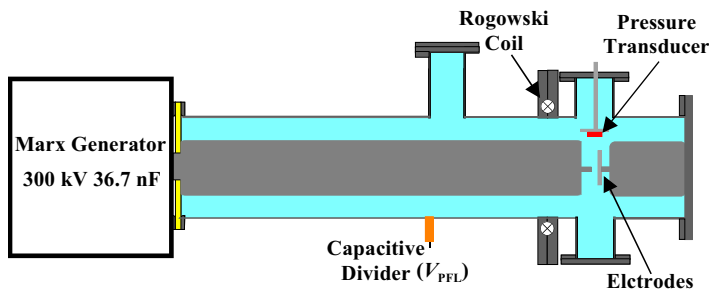


Fig.1 Experimental Setup

Underwater shock waves were generated by pulsed discharge in water (Conductivity: 1.5 μ S/cm). Figure 2 shows a photo of the discharge electrodes for the underwater shock wave. The rod to plane

geometry electrode was used as the discharge electrode in this experiment. The diameter of rod electrode and the area of plane electrode are 10 mm and 38.5×38.5 mm², respectively. The distance between the tip of rod electrode and plane electrode was changed from 2 to 11 mm.

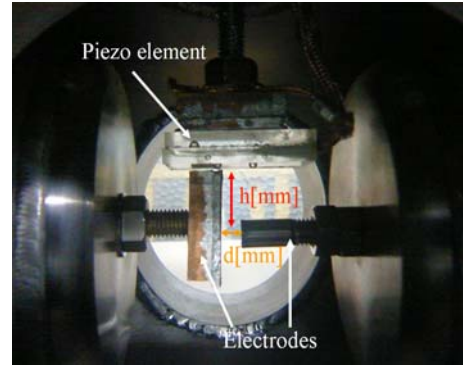


Fig.2 Photo of discharge electrode for underwater shock wave

The applied voltage (V_{PFL}) to and the discharge current (I_d) through the needle to plane electrodes were measured by the capacitive voltage divider and Rogowski coil, respectively. The values of applied voltage and discharge current were calculated by the ratio factor of the voltage divider (43000) and the coefficient of the Rogowski coil (87.7 kA/V). In addition, the polyvinyliden-difluoride (PVDF) pressure transducers with the coefficient of 0.15 MPa/V was used for measurement of the pressure of the underwater shock wave. The oscilloscope (TDS2024B, Tektronix) recorded the signal from the measurement devices.

3. Experimental Results

First, in order to evaluate the pulsed-power machine in which electrical energy, stored in a Marx generator, is switched into the PFL via inductance and in the presence of serial and parallel resistive losses, ringing-gain voltage waveforms were measured. Figure 3 shows the typical ringing-gain voltage waveform, where the charging voltage of the Marx generator was 20 kV. An equivalent circuit, which consists of lumped capacitors, inductors and resistors, was used

which allows the determination of three unknown electrical parameters from two decay constants and the frequency of an oscillatory component calculated from the ringing-gain waveform. As seen in Fig. 3, the ringing period is about 500 ns, which gives the lumped inductance of 892 nH. Taking the PFL's inductance of 152 nH into account, the Marx generator is estimated to be 740 nH. From two decay constants of ringing voltage waveform, serial and parallel resistances of the equivalent circuit are estimated to be 0.82 Ω and 130 Ω , respectively.

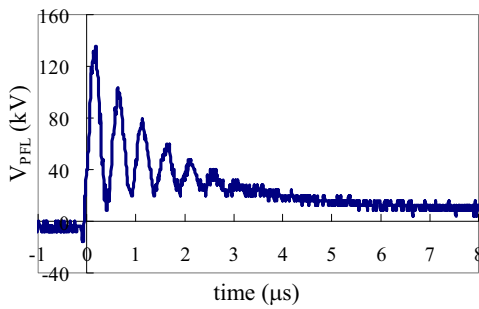


Fig. 3 Typical ringing voltage waveform

Figure 4(a) shows typical waveforms of applied voltage (V_{PFL}) and discharge current (I_d), where the Marx generator was operated at 120 kV and the discharge gap distance was $d=4$ mm. As seen in the figure, the applied voltage reaches the peak value of 110 kV at 180 ns and after the peak drops suddenly. On the other hand, the discharge current rises sharply with a sudden drop of the applied voltage, which suggests a discharge (breakdown) in water. Figure 4(b) shows a typical pressure waveform of the underwater shock wave measured by the PVDF pressure transducer placed at $h=60$ mm from the central axis of the discharge electrodes. Pressure measurements using the PVDF pressure transducer revealed that the underwater shock wave had a peak pressure of approximately 29 MPa with a half-width of approximately 2.5 μ s. As shown in Fig.4(a), it takes about 39 μ s for the underwater shock wave to reach the PVDF pressure transducer. The average velocity of the shock wave is estimated to be 1530 m/s, which is slightly faster than the acoustic velocity in water (1500 m/s).

Figure 5 shows the average velocity of the shock

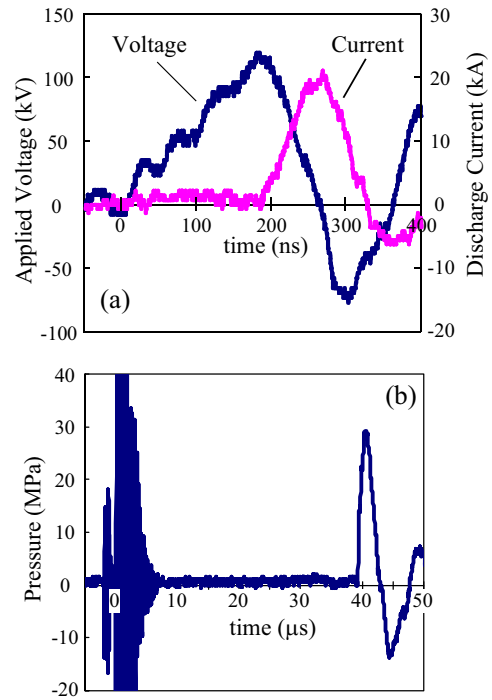


Fig. 4 Typical waveforms of applied voltage and discharge current (a) and pressure of underwater shock wave (b).

wave as a function of the distance between the central axis of the electrode and the pressure detector and the discharge gap length, where the output of Marx generator is 120 kV. Data from up to 5 shots are taken to average shot-to-shot variations and each data point in Fig. 5 is an average of 5 shots. As seen in Fig. 5, when the gap length was set to be 7 mm, the average velocity of 2100 m/s was obtained at 30 mm. Also for

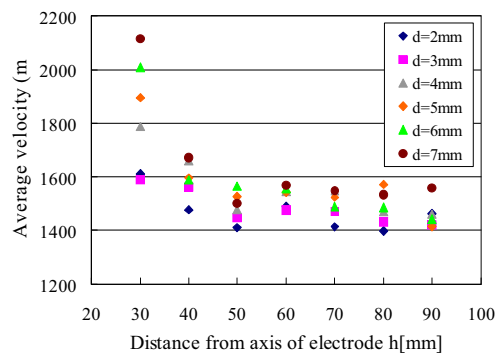


Fig.5 Average velocity of shock wave as a function of distance between central axis of electrode and pressure transducer and gap length.

other gap lengths, the average velocity observed in the vicinity of the axis is fast enough compared with the acoustic velocity in water which shows that the underwater shock wave is generated by the pulsed discharge. The velocity decreases by the acoustic velocity in water as the shock wave propagates away from the central axis. In future, we are planning to evaluate the local velocity of the shock wave in detail by a time of flight method.

Figure 6 shows the pressure of the shock wave measured by the PVDF pressure transducers as a function of the distance between the central axis of the electrode and the pressure detector and the discharge gap length, where the output of Marx generator is 120 kV. Data from up to 5 shots are taken to average shot-to-shot variations and each data point in Fig. 6 is an average of 5 shots. At the gap length of 7 mm, the underwater shock wave with the pressure of 122 MPa was obtained at $h=30$ mm downstream from the axis of the electrode. The pressure of the shock wave increases with the increase of the gap length, since the breakdown voltage increases, i.e., the deposited energy increases. As seen in Fig. 6(b), the pressure of the shock wave varies as $1/h^2$, which

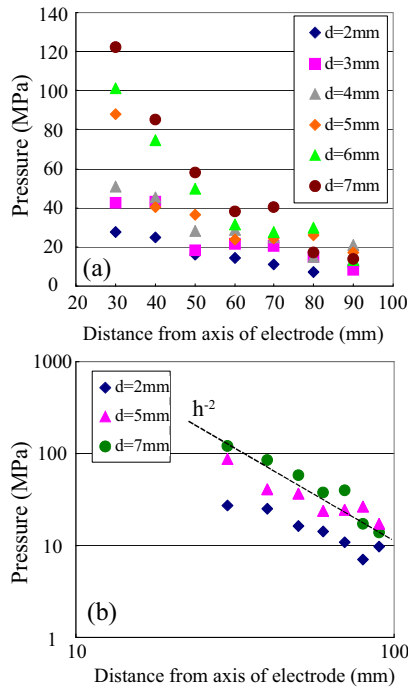


Fig.6 (a) Pressure of shock wave as a function of distance between central axis of discharge electrode and pressure transducer and gap length and (b) log-log graph.

shows that the shock wave propagates as the spherical wave.

4. Conclusions

In order to generate the underwater shock wave with high pressure and good controllability, we investigated the characteristic of the underwater shock wave generated by means of the pulsed discharge in water by the pulse power machine which consists of the Marx generator and the pulse forming line. When the Marx generator was operated at 120 kV and the discharge gap distance set to be $d=7$ mm, the underwater shock with peak pressure of 122 MPa, average velocity of 2100 m/s and half-width of $2.5 \mu\text{s}$ was measured by the PVDF pressure transducer placed at $h=30$ mm downstream from the central axis of the discharge electrode. We found from the propagation characteristic that the shock wave propagates as the spherical wave. In future, we need to investigate the behavior of the underwater shock wave in detail by a time of flight method and optical observations in order to realize the various industrial applications of underwater shock waves.

References

- [1] R.F. Flagg, I.I. Glass, “Explosive-driven, spherical implosion waves”, *Phys. Fluids* **11**, pp.2282–2284 (1968).
- [2] K. Terao, “Nuclear fusion reactor ignited by imploding detonation waves”, *Proc. Int. 35th Intersociety Energy Conversion Engineering Conference and Exhibit (IECEC)*, vol.2, pp. 915–924, Las Vegas, NV, USA (2000).
- [3] G.H. Miller, E.I. Moses, C.R. Wuest, “The National ignition facility: enabling fusion ignition for the 21st century”, *Nucl. Fusion* **44**, pp.S228–S238 (2004).
- [4] R.J. Leeper et al., “Z pinch driven inertial confinement fusion target physics research at Sandia National Laboratories”, *Nucl. Fusion* **39**, pp.1283–1294 (1999).
- [5] E.A. Martin, “Experimental investigation of a high-energy density, high-pressure arc plasma”, *J. Appl. Phys.* **31**, pp.255–267 (1960).

Discharge Phenomena in Supercritical Carbon Dioxide

Takeshi Ihara, Tsuyoshi, Kiyan, Sunao Katsuki, Masanori Hara and Hidenori Akiyama

Graduate School of Science and Technology, Kumamoto University

ABSTRACT

Pulsed streamers in highly pressurized carbon dioxide, including supercritical state were observed using the Schlieren method. The medium temperature and pressure were set to $T = 305$ K and $P = 7.5, 8.0$ MPa, respectively. The gap was a needle-to-plane: the gap length and the tip radius were $d = 7$ and 1 mm and 5 μm , respectively. Pulse voltages of positive/negative polarity generated by a magnetic pulse compression generator were applied to a needle electrode. The main results obtained can be summarized as follows: Positive streamers in a supercritical state are branched tree-like, associated with shock waves of spherical and cylindrical shapes; their average development velocity is in order of 60 km/s. Conversely, the negative corona shape in a supercritical state, a spherical shape without branches, differs greatly from the positive one. The spherical shock wave started from the needle tip at the corona onset. Appearances of positive/ negative discharge obviously differ.

Keywords

Key Words: Pulse streamer, supercritical fluids, carbon dioxide, polarity effect

1. Introduction

Discharge plasma in supercritical fluids has attracted much attention in new discharge plasma sciences [1]-[2]. Supercritical fluids (SCFs) exist at a state that is heated and pressurized above a critical point (fig.1). SCFs have very unique characteristics as an intermediate medium between a gas and a liquid. Supercritical carbon dioxide (scCO_2) in particular has been actively used as a generation field of discharge plasma.

Breakdown characteristics in scCO_2 have been investigated in previous research. T. Kiyan et al. have reported polarity effects on DC breakdown in needle-to-plane electrode geometry from high pressurized gas state to supercritical condition [1]. The results show that, only for negative polarity discharge and not for positive, breakdown voltage in sub- and supercritical state increased due to the occurrence of corona discharge before breakdown. The corona discharge caused relaxation of the electric field at the needle tip. T. Ihara et al. have reported on observation

of pulsed streamer discharge in scCO_2 [2]. The report for the first time indicated the appearance of streamers; these streamers had many branches, and spherical shock waves were confirmed along streamer channels.

This paper investigates polarity effects on pulsed pre-breakdown phenomena in supercritical using the laser Schlieren method.

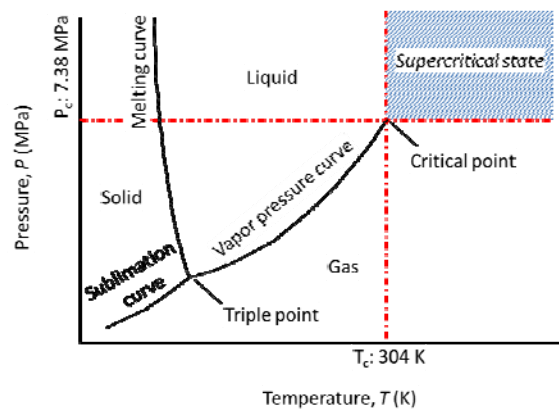


Fig. 1 Phase diagram of CO_2

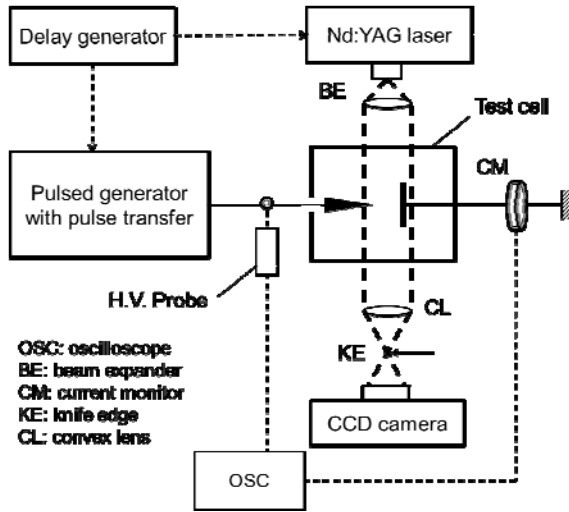


Fig. 2 Schematic of experimental setup

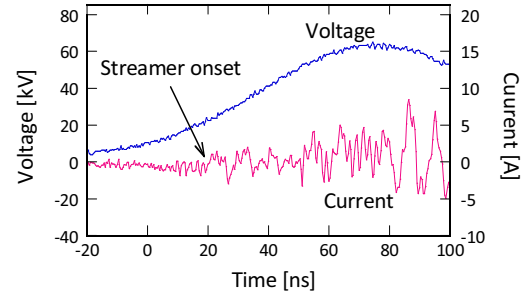
2. Experimental Setup

2.1 Test cell and medium setup

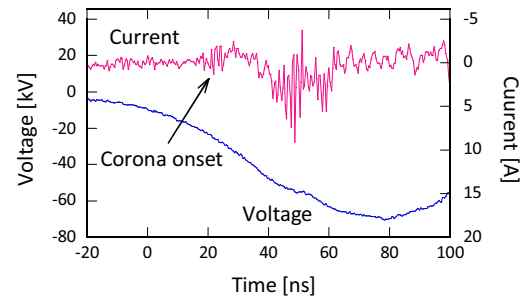
The experimental system including the laser schlieren method is shown in fig. 2. A test cell was prepared consisting of a stainless-steel vessel, two sapphire observation windows and PEEK insulator. Temperature and pressure resistances of the test cell were 373 K and 15 MPa, respectively. Experimental medium conditions were set by the operating temperature and pressure in the test cell. CO₂ conditions such as state and density conform to the state diagram calculated by equation of state [3]. In this experiment, medium conditions were set with the supercritical state at T=305 K, 7.8 MPa and 8 MPa.

2.2 Pulsed power and electrode system

A magnetic pulse compression circuit (MPC) equipped with a pulse transformer was employed to generate discharge plasma. A high-voltage pulse with a rise ratio of 0.75 kV/ns, a pulse width (FWHM) of 400 ns, and a maximum voltage of 90 kV was applied to the needle electrode. Fig 3 shows typical waveforms of voltage and current in both the positive and negative cases. The tip radius of the needle was fixed at 5 μ m by electrolytically polishing. Gap distances in the positive and negative cases were 5 mm and 1 mm, respectively.



(a) positive case



(b) negative case

Fig. 3 typical waveforms of voltage and current

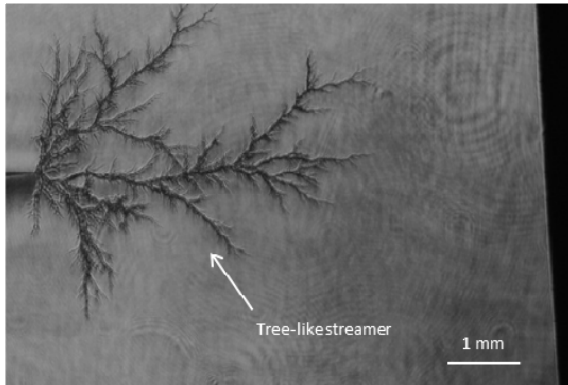
2.3. Schlieren system

The positive/negative discharge was observed using a time-resolved laser Schlieren method, which consists of a 5 ns pulsed Nd: YAG laser (MiniLite, Continuum, 532 nm) and a digital CCD image sensor (Nikon, 23.6 x 15.8 mm CCD sensor, total pixels: 10.75 million). The laser was triggered by a delay generator synchronized with the voltage applied to the electrodes.

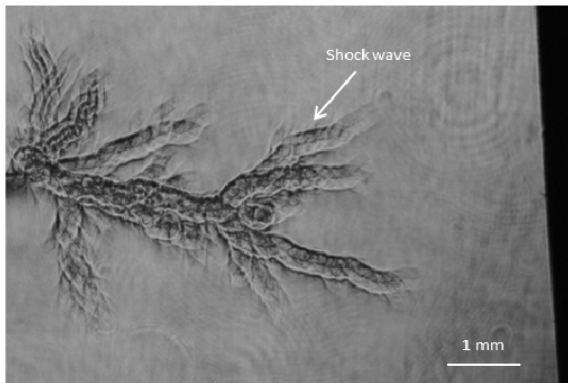
3. Results and Discussion

3.1 Positive pulsed discharge

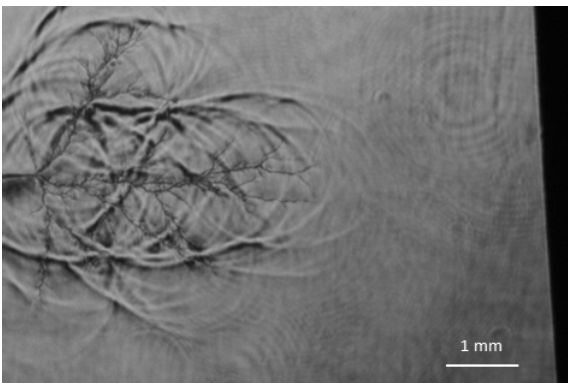
Fig. 4 shows typical Schlieren images in scCO₂ at a primary stage of streamer development and an expansion stage of shock waves, respectively. The time, Δt , is from the streamer onset to the laser radiation. The streamer development and the behavior of shock waves are summarized as follows: The tree-like streamer emerges from the tip of the point electrode when the field strength reaches approximately 9 MV/cm, which was estimated



(a) $\Delta t = 60-65$ ns



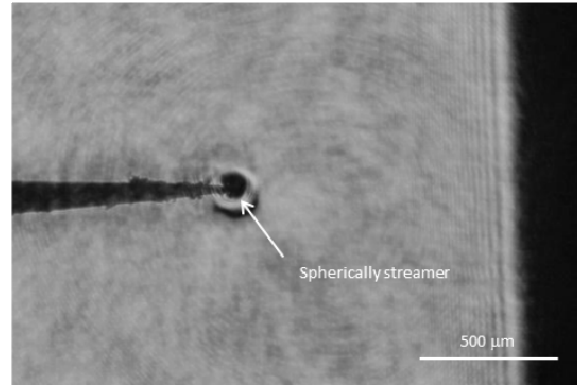
(b) $\Delta t = 560-565$ ns



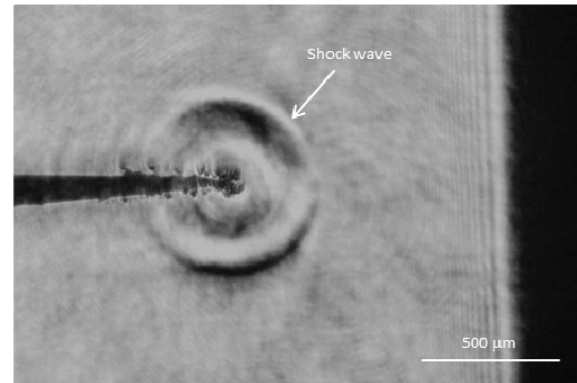
(c) $\Delta t = 3.2$ μ s

Fig. 4 Positive pulsed discharge (supercritical state, $T = 305$ K, $P = 7.8$ MPa, applied $V = 65$ kV)

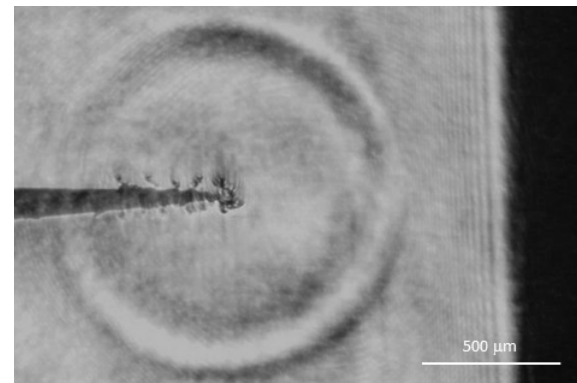
analytically assuming a hyperbolic shape of the needle tip. The streamer splits into several channels, most of which propagate towards the plane electrode. The average streamer velocity is estimated to be on the order of 60 km/s. The propagating streamer is accompanied by two kinds of shock waves: cylindrical and spherical, both originating from the propagating streamer channel.



(d) $\Delta t = 200-205$ ns



(e) $\Delta t = 940-945$ ns



(g) $\Delta t = 1930-1935$ ns

Fig. 5 Negative discharge (supercritical state, $T = 305$ K, $P = 8.0$ MPa, applied $V = 50$ kV)

The shock wave speed ranges between 300~700 m/s. The sound speed of scCO₂ under experimental conditions was calculated as 230 m/s by the equation of state for carbon dioxide^[3]. Though figures are not shown here, other discharge phenomena are summarized as follows: Streamer channels and shock waves decay with the time lapse. When the streamer channels collapse, neither bubble nor secondary

shock wave is observed, contrasting to the case in water. When the applied voltage increases to 70 kV, an arc discharge is triggered, and shock waves start newly from the arc channel. At the collapse stage of arc discharge, Rayleigh-Taylor instability was recognized along the channel.

3.2 Negative pulsed discharge

The experimental results as shown in fig. 5 are as follows: The negative discharge initiated field strength was about 14.5 MV/cm. The discharge appearance was small and spherical. The spherical shock wave was recognized at the tip of needle and developed with the corona onset; the development velocity of the shock wave was around at 350 m/s. In this experimental condition, though the applied voltage was increased to 90 kV, breakdown did not occur due to relaxation of the electric field at the needle tip caused by spherical corona occurrence.

Additional experiments were carried out by decreasing pressure to sub-critical state, or a high pressure gas, in order to clarify the breakdown mechanism in a supercritical state. The corona discharge changed from the smaller spherical shape to a short channel over time. The corona narrowed with growth of the channel when the pressure was decreased to a high pressure gas state. Negative discharge growth was obviously different from that of the positive.

4. Conclusions

Polarity effects on pulsed pre-breakdown phenomena were investigated by means of laser Schlieren method. The main results obtained can be summarized as follows. 1) The shape of positive streamers in supercritical state is a branched tree-like associated with shock waves of spherical and cylindrical shapes. The number of positive streamer branches decreases with decreasing fluid density. 2) The negative corona shape in supercritical state differs greatly from the positive one, and was a spherical shape without branching at the initial stage. The spherical shock wave started from the needle tip at the corona onset. Spherical corona causes

relaxation of electric field at tip of needle. The appearances of positive/ negative discharge obviously differ. Therefore, the discharge mechanism in supercritical state needs to be considered in the unique thermal and electrical properties related to supercritical state.

Acknowledgment

This work was supported financially in part by the Global COE program on Global Initiative Center for Pulsed Power Engineering from the Ministry of Education, Culture, Sports, Science and Technology (MEXT), Japan.

References

- [1] T. Kiyan et al., "Polarity Effect in DC Breakdown Voltage Characteristics of Pressurized Carbon Dioxide up to Supercritical Conditions", IEEE Trans. on Plasma Science, Vol. 36, no.3, pp. 821-827, (2008)
- [2] T. Ihara et al., "Positive Pulsed Streamer in Supercritical Carbon Dioxide", IEEE Trans. on Plasma Science, 10.1109/TPS.2011.2156816, in press
- [3] R. Span and W. Wagner, "A new equation of state for carbon dioxide covering the fluid region from the triple point temperature to 1100 K at pressures up to 800 MPa", J. Phys. Chem. Ref., Data 25, pp. 1509-1596 (1996)

Production of Metal Contained Carbon Plasma Using Shunting Arc Discharge for Composite Film Preparation

H. Aoki, K. Takahashi and K. Takaki

Iwate University, 4-3-5 Ueda, Morioka, Iwate 020-8551, JAPAN

ABSTRACT

Nitrogen and titanium contained plasmas were induced by a carbon shunting arc discharge. The carbon shunting arc was generated using a carbon rod which was held vertically between a pair of titanium plane electrodes. The titanium ions were supplied from the titanium plane electrodes during the shunting arc discharge. The nitrogen gas was injected into the vicinity of the carbon rod to produce nitrogen contained plasmas. It was confirmed from a spectroscopic observation that the produced plasma contained carbon and titanium ions without nitrogen injection. The spectra of nitrogen species were also confirmed at 10 Pa nitrogen gas injected into the discharge chamber. The electron density was measured using a double probe and was obtained as 10^{18} m^{-3} orders.

Keywords

PBII&D, DLC, Shunting arc, Arc discharge, Ion source, Ion density, Double probe.

1. Introduction

A shunting arc is a pulsed plasma source for solid-state materials such as titanium, tungsten, silicon and carbon [1-2]. The shunting arc is ignited by self-heating of the rod material to increase vapor pressure and/or emit thermo electrons around the material, which is connected to a current source such as a capacitor [3]. Since the shunting arc system consists of simple components, it has a potential to be a cost-effective technology. Moreover, the shunting arc can be easily generated in a wide gas pressure range from vacuum to atmospheric pressure by evaporation from a rod heated by a pulse current [4]. Accordingly, the shunting arc is a promising method to prepare droplet-free films [5].

Diamond-like carbon (DLC) based composite films have many superior properties such as high hardness and optical characteristics and are used in many industrial applications for surface modification. DLC films can be prepared using the shunting arc discharge employing a carbon rod as a solid material [5]. DLC-based composite films can also be prepared

using the carbon shunting arc with addition of reactive gases [6-7]. For example, a nitrogen-containing DLC film is prepared using a magnetically driven carbon shunting arc in nitrogen gas [7].

DLC films containing metals such as titanium and tungsten stir up interest in various application fields owing to their excellent tribological properties, high electrical conductivity, and so on. These superior properties are suitable for many kinds of sensors such as electro-catalytic sensors. The titanium-containing DLC film with a few hundreds of nanometer thickness is prepared as a low friction coating using the sputtering procedures.

The shunting arc discharge in various electrode materials may be capable of producing individual composite films. The titanium-containing DLC film was prepared using carbon shunting arc discharge with titanium rail electrodes [8]. It was confirmed based on spectroscopic measurements that the shunting arc plasma contained titanium and carbon ions which were extracted by negative pulse voltage.

The ion densities in the vicinity of the ion extraction electrode were also obtained by ion current accelerated with negative pulse voltage [8]. However, it is difficult to clarify the dynamics of the shunting arc plasma because the measurement method of the ion density employed in the previous study was limited to the diffuse region of the shunting arc plasma at 200 μs after the arc discharge. In this study, the electron density distributions are measured using a time-resolved double probe to clarify the dynamics of the shunting arc discharge plasma.

2. Experimental Setup

A schematic diagram of the experimental facilities is shown in **Fig. 1**. A cylindrical vacuum chamber of 100cm-length and 80cm-inner-diameter was evacuated down to 2×10^{-2} Pa with a diffusion pump and a rotary pump. A carbon rod of 2mm-diameter and 4cm-length was held horizontally by a pair of titanium electrodes. The rod holder made of titanium had dimension of 5cm-width, 1cm-thickness, and 10cm-length. The rod holder was set with a 4cm-separation, and the carbon rod was set between the rod holders. The total resistance of the shunting arc generation unit was determined to be approximately about 5Ω by a potential drop measurement.

A 20 μF -capacitor bank of applied voltage in the 900 V was employed to supply kilo amps pulse current using a spark gap as closing switch and was connected to the rod holder. Two current transformers (Pearson 4997 and 2877) were used to measure arc current and the double probe current. High-voltage

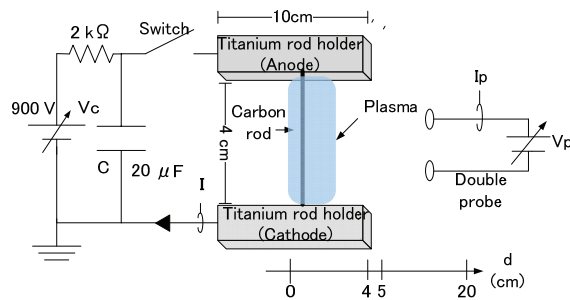


Fig. 1 A schematic diagram of the experimental facilities used shunting arc generation and a floating double probe circuit.

probes (Tektronix P5100) were used to measure the voltage between the rod holders, i.e., the voltage between the electrodes. The signals were digitized by a digitizing oscilloscope (Tektronix TDS2024B) and were transported to a personal computer to calculate power consumption in the carbon rod and shunting arc discharge.

The ion density of the plasma was measured with a flat-type double probe with a collecting area of 7 mm² made from a stainless rod (SUS316L) of 1.5mm-radius. The collecting part of the double probe was changed in position from 5 to 20 cm apart from the carbon rod. The probe bias voltage was changed in the range from +50 to -50 V using a DC power supply.

3. Results and Discussion

3.1 Electrical characteristics

Figure 2 (a) shows the waveforms of the circuit current and the voltage between the electrodes without nitrogen injection. The background gas pressure is 0.02 Pa. The waveforms can be divided into two regions. In the first region, the voltage between the electrodes rises to 0.6 kV at 3.0 μs from the switch-on and the current increases gradually. In this region, the current of 0.12 kA flows through the

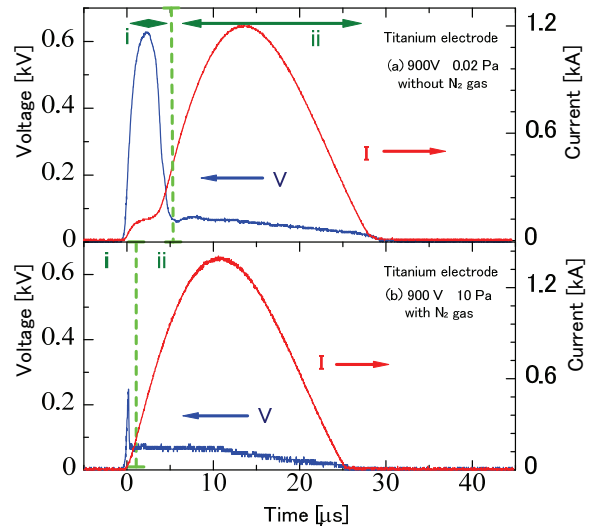


Fig. 2 Waveforms of current through the electrodes and voltage between the electrodes at 900 V charging voltage (a) without nitrogen injection (0.02 Pa), and (b) with nitrogen injection to 10 Pa in gas pressure.

rod. These current values almost agree with those estimated based on Ohm's law ($=600\text{V}/5\Omega$). Therefore this phase indicates the current flows through the rod and the rod temperature rises with Ohmic heating process.

In the second region, the voltage abruptly decreases $6.0\ \mu\text{s}$ after switching on the closing gap switch and the abrupt decrease of voltage is accompanied by an abrupt increase in current. These rapid changes in voltage and current indicate the initiation of the shunting arc. The arc current is sinusoidal with duration of about $35\ \mu\text{s}$, and its peak current is about $1.1\ \text{kV}$, $20\ \mu\text{s}$ after switch-on. This is due to LC oscillation from the capacitor and the inductance of the wiring of the present shunting arc generation system. The minimum resistance of the arc discharge can be estimated from the current and the voltage waveforms and is obtained as $0.08\ \Omega$.

Figure 2 (b) shows the waveform of the circuit current and the voltage between the electrodes with nitrogen injection to $10\ \text{Pa}$ in gas pressure. In the first region, the voltage between the carbon electrode rises to $0.5\ \text{kV}$ in $1.0\ \mu\text{s}$. In this region, the current of about $0.05\ \text{kA}$ flows through the rod. The arc current is sinusoidal with duration of approximately $25\ \mu\text{s}$, and its peak current is about $1.2\ \text{kV}$ at $13\ \mu\text{s}$ after the switch-on.

Figure 3 shows the heating energy to ignite the shunting arc and the onset voltage as a function of nitrogen gas pressure at $900\ \text{V}$ charging voltage of

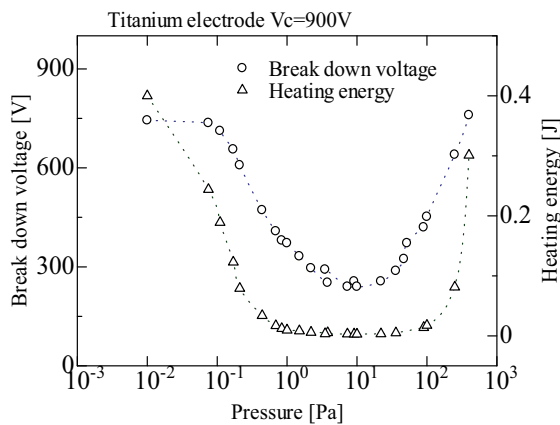


Fig. 3 Breakdown voltage and heating energy to generate shunting arc at $900\ \text{V}$ capacitor charging voltage as a function of nitrogen gas pressure.

the capacitor. The heating energy and the onset voltage have U-shape characteristics in pressure range from 0.02 to $400\ \text{Pa}$. The heating energy decreases from 0.4 to $0.003\ \text{J}$ with increasing gas pressure from 0.02 to $10\ \text{Pa}$ in Paschen left region, and then increases to about $0.3\ \text{J}$ with increasing gas pressure to $400\ \text{Pa}$. The discharge onset voltage decreases from 800 to $240\ \text{V}$ with increasing gas pressure from 0.01 to $10\ \text{Pa}$, and then increases to about $800\ \text{V}$ with increasing gas pressure to $400\ \text{Pa}$.

3.2 Spectroscopic observation

Figure 4 shows the spectral lines of light emission from the induced plasma (a) without nitrogen injection ($0.02\ \text{Pa}$), and (b) with nitrogen injection to $10\ \text{Pa}$ in gas pressure. The spectroscopic measurement was carried out in wavelength region from 300 to $400\ \text{nm}$ with resolution ability of less than $2\ \text{nm}$ using optical multichannel analyzer (HAMAMATSU C10027). Several spectrum lines of titanium and carbon ions are observed without nitrogen injection. These lines are mainly originated from single carbon and titanium ions. The spectrum lines from nitrogen ions appear with injection of

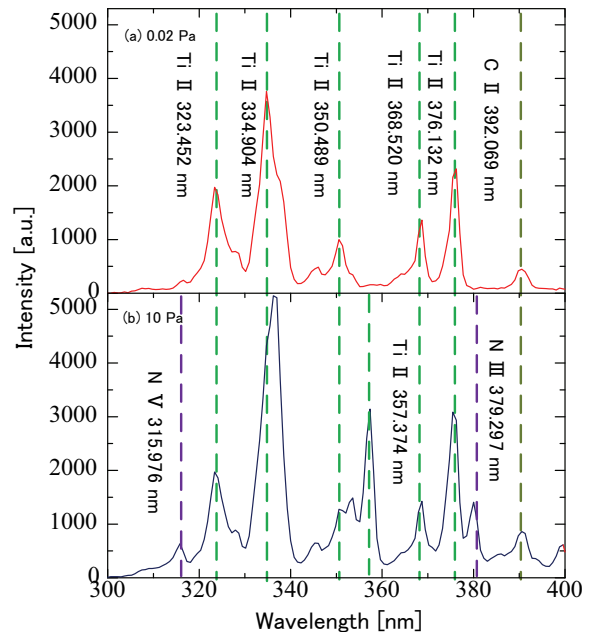


Fig. 4 Emission spectra of shunting arc for two different pressures (a) without nitrogen injection ($0.02\ \text{Pa}$), and (b) with nitrogen injection to $10\ \text{Pa}$ in gas pressure.

nitrogen at 10 Pa in gas pressure. The lines from single carbon and titanium ions are also observed. Intensities of the light emission from titanium ions increase by injecting nitrogen gas owing to the increase of the arc current as shown in Fig. 2.

3.3 Double probe measurement

Figure 5 shows the waveforms of the double probe current at various probe voltages. The double probe is located at 5 cm apart from carbon rod. The ambient gas pressure and the charging voltage are set as 0.02 Pa and 900 V, respectively. The probe current starts to increase at 10 μ s after gap switch on. The period of the double probe current is almost synchronized with that of the discharge current. Using waveforms of the double probe current, the I_p - V_p curves are obtained at various times from the arc ignition.

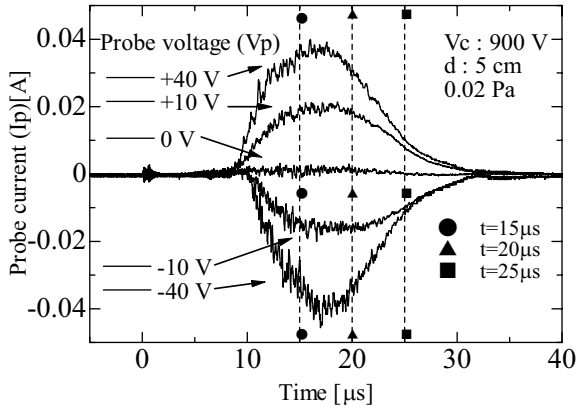


Fig. 5 Waveforms of the double probe current changing bias voltage from +50 V to -50 V.

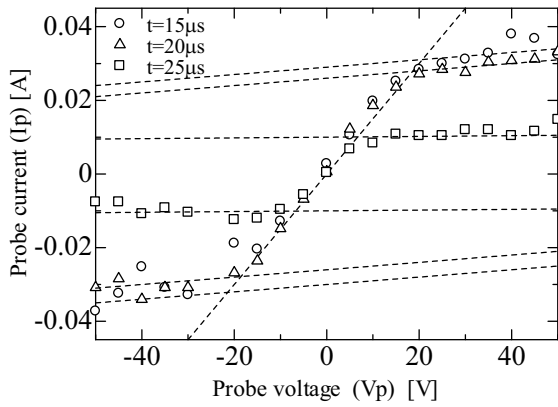


Fig. 6 Voltage-current characteristic of the double probe current at various time for shunting arc plasma.

Figure 6 shows the I_p - V_p curves of the double probe used to plot at various times. The electron temperature and the electron density can be obtained using I_p - V_p curves. The electron temperature and the electron density N_e is determined as follows;

$$T_e = - \frac{\sum I_i}{A_1 \times \left(\frac{dI_p}{dV_p}\right)_{V_p=0} - A_2 \left(\frac{dI_p}{dV_p}\right)_{V_p \gg 0}} [eV] \quad (1),$$

$$N_e = \frac{\sum I_i}{0.61S} \sqrt{\frac{m_i}{kT_e}} [m^{-3}] \quad (2).$$

Where, m_i is the mass of ion, e is the electron charge, S is the area of the probe, k is Boltzmann constant, A_1 and A_2 are constants of 4 and 3.28 in low pressure plasma, respectively [10].

Figure 7 (a) and (b) show the temporal evolution of the electron density profile obtained at various measurement positions in the range from 5 to 20 cm. The ambient gas pressure and the charging voltage are set as 0.02 Pa and 900 V, respectively. The electron densities are obtained as 10^{18} m^{-3} orders and

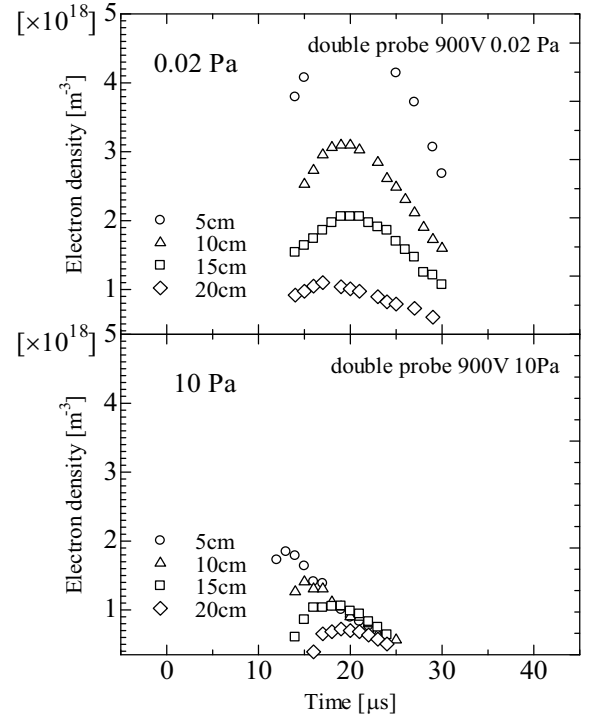


Fig. 7 Electron density as a function of times at various distances from carbon rod at (a) 0.02 Pa and (b) 10 Pa of nitrogen gas pressure.

have maximum values at 20 μs after the arc ignition at gas pressure of 0.02 Pa. After the 20 μs from the arc ignition, the electron density decays with the time. The electron density decreases by increasing the ambient gas pressure from 0.02 to 10 Pa.

4. Conclusions

The nitrogen and titanium contained plasmas are induced by the carbon shunting arc discharge. From the spectroscopic observation the produced plasma contained carbon and titanium ions without nitrogen injection. The spectra of nitrogen species are confirmed at 10 Pa nitrogen gas injected into the discharge chamber. The electron density of the shunting arc plasma is measured using the double probe and is obtained as 10^{18} m^{-3} orders.

Acknowledgement

The authors would like to express our gratitude to Prof. K. Yukimura of National Institute of Advanced Industrial Science and Technology, Prof. T. Fujiwara of Iwate University, Dr. S. Mukaigawa Iwate University for their variable comments and fruitful discussions. The authors would like to thanks to Mr. H. Shida for his technical assistant of the research.

References

- [1] K. Yukimura, R. Isono, T. Monguchi, K. Yoshioka, and S. Masamune, "Pulsed Metal Ion Source by Triggerless Shunting Arc Discharge", *J. Vacuum Sci. Technol. B*, **17**, 2, pp.871-875 (1999).
- [2] K. Yukimura and Y. Tani, "Generation of Triggerless Silicon Shunting Plasma and Ion Extraction", *Surf. Coat. Technol.*, **142/144**, pp.388-391 (2001).
- [3] K. Takaki, O. Kumagai, S. Mukaigawa, T. Fujiwara, M. Kumagai and K. Yukimura, "Ion Extraction From Magnetically Driven Carbon Shunting Arc Plasma", *IEEE Trans. Plasma Sci.*, **34**, 4, pp.1209-1215 (2006).
- [4] K. Yukimura and S. Masamune, "Shunting Arc Plasma Generation over a Wide Range of Ambient Pressure and Ion Extraction", *Rev. Sci. Instrum.*, **73**, pp.860-862 (2002).
- [5] K. Yukimura, M. Kumagai, M. Kumagai, H. Saito, M. Kohata and K. Takaki, "Deposition of Amorphous Carbon Using a Shunting Arc Discharge", *Surf. Coat. Technol.*, **174/175**, pp.1187-1190 (2003).
- [6] K. Takaki, S. Mukaigawa, T. Fujiwara and K. Yukimura, "Shunting Arc-Produced Hybrid Plasma and its Magnetic Drive for PBII&D", *Surf. Coat. Technol.*, **201**, pp.6490-6494 (2007).
- [7] K. Takaki, K. Imanishi, T. Murakami, T. Fujiwara, Y. Suda and K. Yukimura, "Production of Nitrogen-Containing Carbon Plasma Using Shunting Arc Discharge for Carbon Nitride Films Preparation", *Physica Status Solidi (a)*, **205**, 4, pp.971-975 (2008).
- [8] K. Takaki, T. Murakami, S. Mukaigawa, T. Fujiwara and K. Yukimura, "Production of Titanium-Coating Carbon Plasma Using Shunting Arc Discharge for Hybrid Film Deposition", *Jpn. J. Appl. Phys.*, **49**, p.046001 (2010).
- [9] K. Takaki, S. Mukaigawa and T. Fujiwara, "Ion Extraction from Carbon Shunting Arc Plasma", *Appl. Phys. Lett.*, **82**, 16, pp.2583-2585 (2003).
- [10] T. Dote, "A New Method for Determination and Plasma Electron Temperature in the Floating Double Probe", *Jpn. J. Appl. Phys.*, **7**, pp.964-965 (1968).

APPLICATION OF TRIBOLUMINESCENCE TO ROENTGEN DIAGNOSIS

Naoya TASHIRO and Seizo FURUYA

Saitama Institute of Technology, Fukaya 369-0293 JAPAN

ABSTRACT

Triboluminescence is a luminous phenomenon resulted from friction; for example, peeling scotch tape, breaking rock sugar with a hammer, peeling mica and so on. Triboluminescence is well known over 50 years but in 2008 UCLA group reported the radiation of x-ray region by triboluminescence in vacuum for the first time. UCLA group made an automatic machine which peels scotch tape. With a view to practical application of triboluminescence to roentgen diagnosis we made an automatic peeling machine similar to that of UCLA group. Replacing conventional x-ray tube with triboluminescence is very useful to roentgen diagnosis. First, we have confirmed the x-ray generation from triboluminescence using a filtered phosphor screen when the parameters such as the followings are changed; peeling speed, atmospheric pressure, variety of scotch tape, emission angle etc. Then in a similar way we have successfully measured the x-ray dose from triboluminescence using a potable dosimeter. It was found that the x-ray generation from triboluminescence has a directional property.

I. Introduction

Triboluminescence is a luminous phenomenon resulted from friction; for example, peeling scotch tape, breaking rock sugar with a hammer, peeling mica and so on. Triboluminescence is well known over 50 years but in 2008 UCLA group reported the radiation of x-ray region by triboluminescence in vacuum for the first time.¹⁾ UCLA group made an automatic machine which peels scotch tape. With a view to practical application of triboluminescence to roentgen diagnosis we made an automatic peeling machine similar to that of UCLA group. An x-ray tube for conventional roentgen diagnosis needs a high voltage power supply. In contrast, triboluminescence does not need it. So it is very useful for roentgen diagnosis to replace a conventional x-ray tube with triboluminescence.

In our previous report²⁾, we have made an automatic peeling machine similar to that of UCLA group and have confirmed the visible light and x-ray emissions from the peeling tape. The visible light emission from peeling tape seems continuous by the naked eye but we have verified using a photomultiplier that the peeling tape emits light in pulses actually.

In this report, at first, we have confirmed the x-ray generation from triboluminescence using a filtered phosphor screen when the parameters such as the followings are changed; peeling speed, atmospheric pressure, variety of scotch tape, emission angle etc. Then in a similar way we have

successfully measured the x-ray dose from triboluminescence using a potable dosimeter. It was found that the x-ray generation from triboluminescence has a directional property.

II. Experimental setup

We made an automatic peeling machine similar to that of UCLA group. Figure 1 shows a photograph of the machine. A geared motor of 200 RPM is used for a driving force.

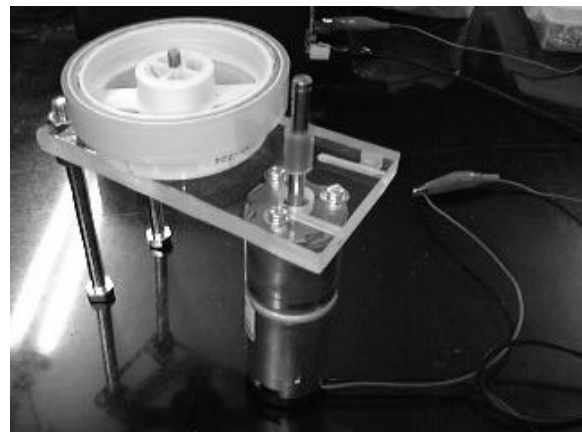


Figure 1 Photograph of automatic peeling machine

Figure 2 shows the vacuum pump system. A turbo molecular pump (TMP) and a rotary pump

(RP1) are a pair (PFEIFFER VACUUM, Turbomolecular Drag Pumping Station TSH261 with DUO2.5). The pumping speed of RP1 is 2.5 m³/h and total pumping speed is 210 L/s. To enhance the pumping capability RP2 (SHINKU KIKO, GVD-135A, 135 L/m) is added.

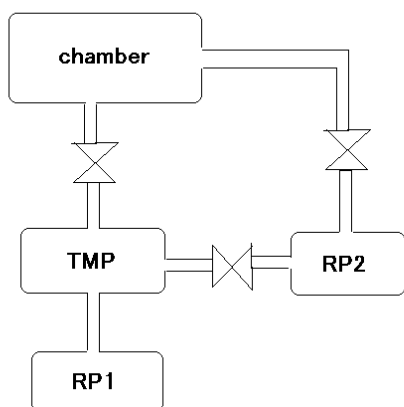


Figure 2 Vacuum pump system

Figure 3 shows a photograph of the vacuum chamber. The inner diameter is 210.7 mm and the inner height is 200 mm.

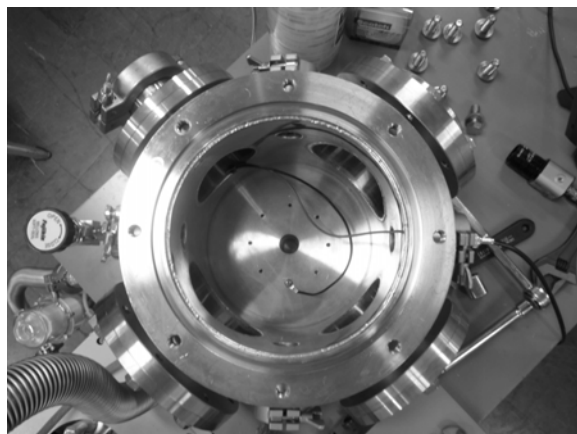


Figure 3 Photograph of vacuum chamber

III. Confirmation of x-ray generation

In the previous report²⁾, a thin piece of plastic scintillator (OKEN, NE102A) was put near the peeling tape to confirm the generation of x-ray. In this report, a phosphor screen was used to detect the x-ray. The phosphor screen is PHOS-RP22SS-C5x5-R1000(Rugged) manufactured by Kimball

Physics. Figure 5 shows an open-shutter photograph of emission of visible light from peeling tape and the phosphor screen in vacuum. The phosphor screen emits visible light when irradiated with x-ray, and it is found that the phosphor screen emits light in the photograph. The photograph was taken by turning off a room light and covering the vacuum chamber overall with a blackout curtain. Soon after peeling the tape, the pressure in the chamber started to increase. In the previous report²⁾, when the pressure was more than 7×10^{-3} torr, the plastic scintillator did not emit light. In this experiment, the pressure became 1×10^{-2} torr, balancing the outgas from peeling tape with the evacuation by vacuum pump. At that pressure, the phosphor screen still emits visible light.

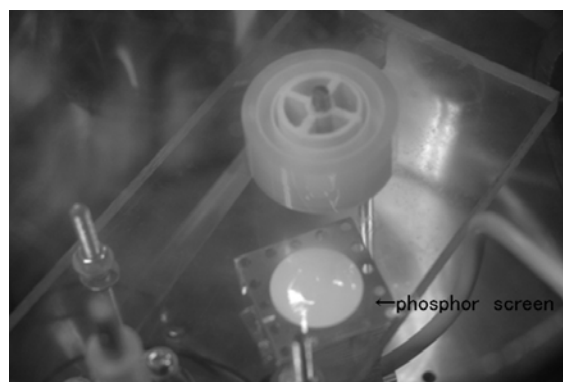


Figure 4 Experimental setup of phosphor screen

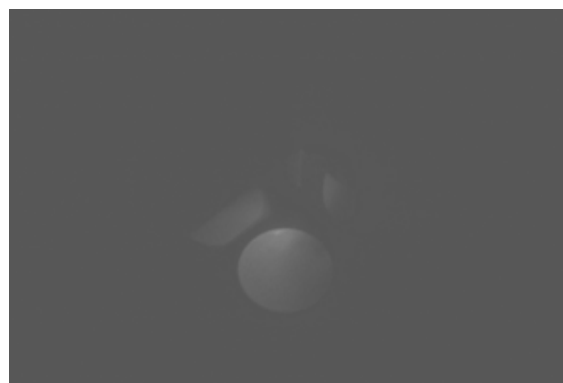


Figure 5 Photograph of light emission from peeling tape and phosphor screen

Next, the phosphor screen was wrapped by a polymer film to cut UV light. The polymer film is food wrap, so detailed transparent characteristics are not clear. Figure 6 shows an open-shutter photograph of the emission from the polymer-film-filtered phosphor screen. As shown in

the figure, because the polymer film was not flat, the phosphor screen emitted light in stripes.

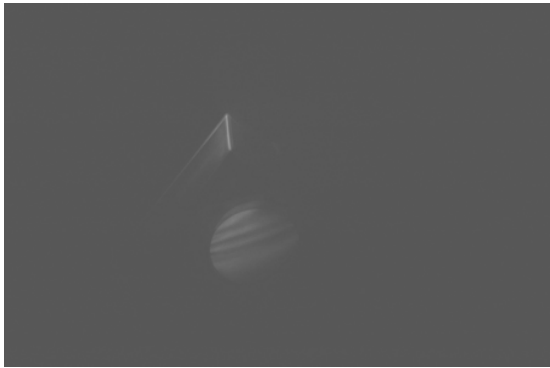


Figure 6 Photograph of emission from polymer-film-filtered phosphor screen



Figure 7 Experimental setup of aluminum foil

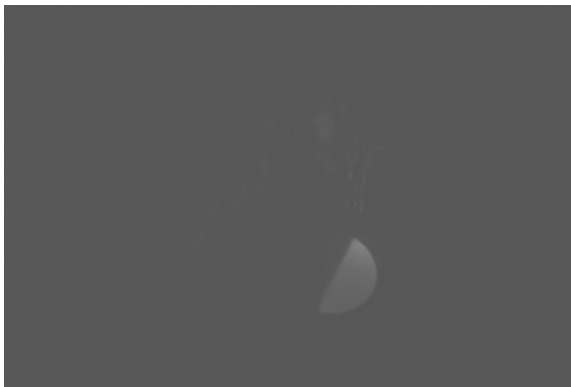


Figure 8 Photograph of emission from aluminum-foil-filtered phosphor screen

Finally, an aluminum foil was set between peeling tape and phosphor screen to cut visible and UV light. The experimental setup of the aluminum foil was shown in Figure 7, and Figure 8 shows an open-shutter photograph of the emission from the aluminum-foil-filtered phosphor screen. As shown in

Figure 8, because the size of aluminum foil is insufficient, the phosphor screen produced luminescence in semicircular shape due to stray light.

IV. Measurement of x-ray dose

Figure 9 shows the experimental setup to measure the x-ray dose of upward direction. The x-ray dose was measured using a portable dosimeter(ALOKA, PDM-117). Figure 10 shows the time variation of pressure and accumulated x-ray dose. The dotted lines in the figure are the data in the case that the initial pressure was 1.0×10^{-3} torr and the peeling speed is 0.6-1.2 cm/s. The x-ray dose of $1 \mu\text{Sv}$ was detected for 10-minute exposure. The broken lines are the experimental results in the case of 7.8×10^{-4} torr and 0.6-1.2 cm/s. When the initial pressure is low, the x-ray dose increases. When the peeling speed increases, the x-ray dose also increases? The continuous lines are the data in the case that the peeling speed is twice. The answer is no because the pressure rapidly increases.

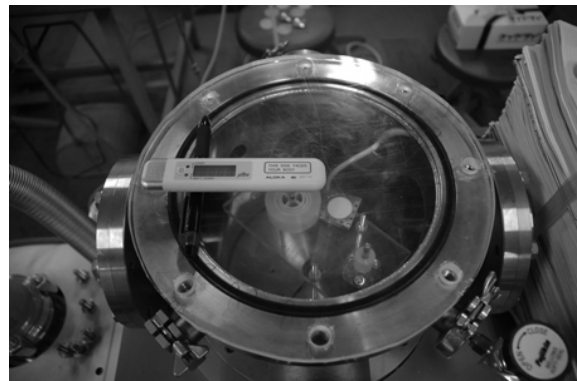


Figure 9 Experimental setup to measure x-ray dose of upward direction

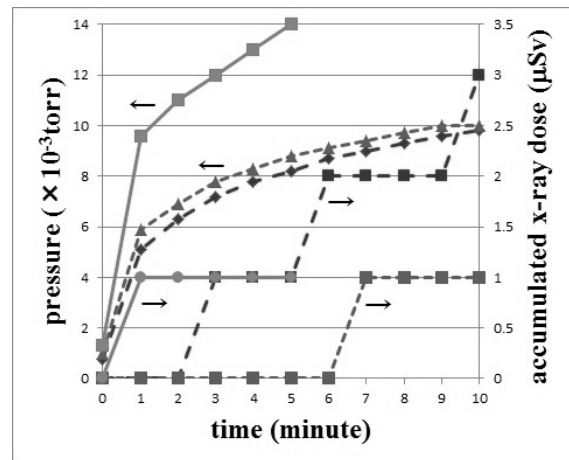


Figure 10 Time variation of pressure and accumulated x-ray dose

Figure 11 shows the experimental setup to measure the x-ray dose of traverse direction. The x-ray was not detected in this setup, so the x-ray was not radiated to the traverse direction.

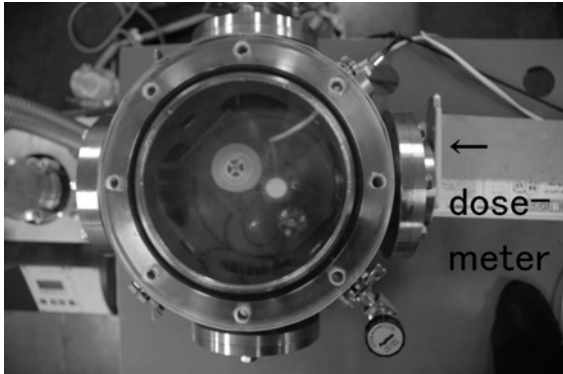


Figure 11 Experimental setup to measure x-ray dose of traverse direction

V. Conclusions

We have confirmed the x-ray generation from triboluminescence using a filtered phosphor screen when the parameters such as the followings are changed; peeling speed, atmospheric pressure, variety of scotch tape, emission angle etc. Then in a similar way we have successfully measured the x-ray dose from triboluminescence using a portable dosimeter. It was found that the x-ray generation from triboluminescence has a directional property.

Acknowledgements

We cordially thank Professor Emeritus Shozo ISHII and Dr Shinji IBUKA of Tokyo Tech for their ungrudging support to our experiments.

References

- 1) C.G.Camara, J.V.Escobar, J.R.Hird and S.J.Putterman, "Correlation between nanosecond X-ray flashes and stick-slip friction in peeling tape", *nature*, **455**, 1089-1092 (2008).
- 2) Y.Arai and S.Furuya, "Practical application of triboluminescence to roentgen diagnosis", APSPT-6(The Sixth Asia-Pacific International Symposium on the Basic and Application of Plasma Technology) December 14-16, 2009, Hsinchu, Taiwan, R.O.C. proceeding pp.124-127

Laser Target using Continuous Supersonic Jet

Yujin Ogata, Kazumasa Takahashi, Hajime Kuwabara¹, Mitsuo Nakajima, and Kazuhiko Horioka*

*Department of Energy Sciences, Tokyo Institute of Technology,
Nagatsuta 4259, Midori-ku, Yokohama, 226-8502, Japan*

¹*Yokohama Engineering Center, IHI Corporation, 1,
Shin-nakaharacho, Isago-ku, Yokohama, 235-8501, Japan*

For an extreme ultraviolet (EUV) light source, Sn plasmas, which can produce a strong radiation with high conversion efficiency at 13.5nm, attract attention. The purpose of this study is to establish technology to form and recover a tin vapor supersonic jet in vacuum and to make clear the interaction between the supersonic free jet and an incident laser experimentally. In order to make the tin vapor, a tantalum crucible is inductively heated up and the radiation loss is compared with the input energy. In future, we increase the number of shields and heat the tantalum crucible to the boiling point. We observe the density gradient of vapor jet emitted from a supersonic nozzle by shadowgraph. We are planning to make a study on the interaction process between laser and the free jet.

Keywords: EUV, Debris, Laser-produced plasma, Tin, Supersonic free jet

I. INTRODUCTION

As the next generation optical lithography for advanced large-scale integrated circuit, EUV light source at 13.5 nm is under development now. In a practical EUV lithography system, an average EUV power of 180 W in 2%-bandwidth around 13.5 nm is required at the intermediate focus. EUV light sources can be roughly classified into two groups; that is based on a laser-produced plasma (LPP) or a discharge produced plasma.

Figure 1 shows a basic concept of LPP. A high energy pulsed laser irradiates a target, producing high temperature and high density plasma light sources with a particular spectrum range. In addition, because there is not a structure interrupting the optical transport, we can get a large collecting solid angle around the plasma source. LPP has other advantages such that a control of the source size is easy and an angle distribution of the EUV power is uniform. [1–4]

In EUV lithography, Mo/Si multilayer mirror which has a sensitivity peak at 13.5nm is used, in which 1%-bandwidth around 13.5nm is effective. An element having an emission spectrum in this domain is used as a target selectively. Sn plasmas can produce a brilliant light with high in-band conversion efficiency at 13.5nm.

A solid, a liquid, and a gas can be the plasma medium. However, the solid target generates a lot of debris that damages collector optics and limits the lifetime of the optical system. A high repetition supply, that is indispensable to the high average power output, is predicted to be difficult in case of the solid target.

In the case of the liquid droplet, the laser spot size is larger than the target size, so a part of the beam passes outside the droplet. It is required that Sn micro-droplets

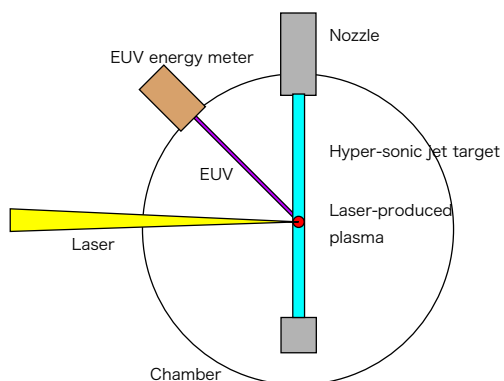


Fig. 1: Basic concept of laser-produced plasma (LPP) using continuous free jet

have to be expanded, in advance, by 10-20 times before CO₂ laser irradiation, in order to improve the coupling efficiency between the long-wavelength CO₂ laser and micro-droplets. The double laser irradiation method is considered to be difficult to operate practically [1].

The purpose of this study is to establish the technological basis to form and recover a supersonic metal vapor jet continuously in vacuum. With controlled tin vapor supersonic jet, we can suppress the debris; i.e., the formation of micro-droplets and fast neutral particles. At the same time, by the controlled density profile of jet, we can expect to get high conversion efficiency. Also, by the continuous supply and recovering of the vapor, we can realize highly reproducible and repetitive operation of the light source.

An important issue that we should make clear experimentally is the interaction between the supersonic free jet and laser. Because a high temperature domain is generated by the laser irradiation in supersonic tin vapor jet. With laser irradiation, temperature rises locally and

*Electronic address: khorioka@es.titech.ac.jp

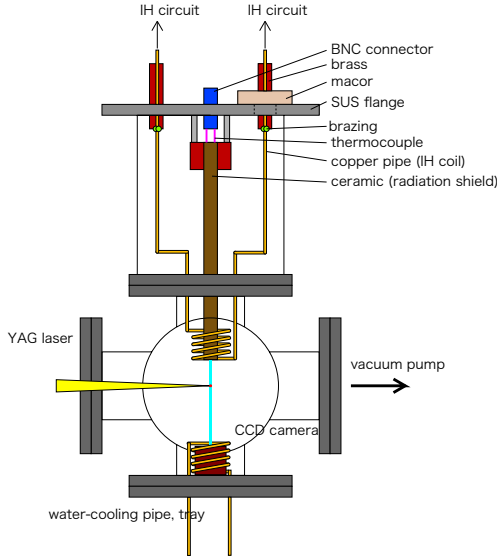


Fig. 2: Schematic of experimental setup

the local Mach number of the jet decreases. Naturally a transonic and subsonic domain should grow up. Then it is expected that disturbance occurred in the interaction domain reaches upper region of the flow.

II. EXPERIMENT

Figure 2 shows a schematic diagram of the experimental device. The experimental device consists of a nozzle which discharges a tin vapor jet in vacuum, a saucer which collects the jet, and an induction heater for tin vapor. It is necessary to aim the nozzle exit downward so that the jet does not interfere with the induction heating (IH) coil. The induction heating coil is made of copper pipe to cool it with water flow. The device also consists of a vacuum exhaust system, a Nd:YAG laser, a CCD camera, and a measurement device for the temperature history.

A. Supersonic nozzle

We use tantalum as the nozzle and crucible materials.

Eq.(1) shows the relation between the cross section and the Mach number of isentropic flow,

$$\frac{A}{A^*} = \frac{1}{M} \left[\frac{(\gamma - 1) M^2 + 2}{\gamma + 1} \right]^{\frac{\gamma+1}{2(\gamma-1)}} \quad (1)$$

where A is the cross section, A^* is the throat cross section, and γ is specific heat ratio.

The mass flow rate can be estimated by

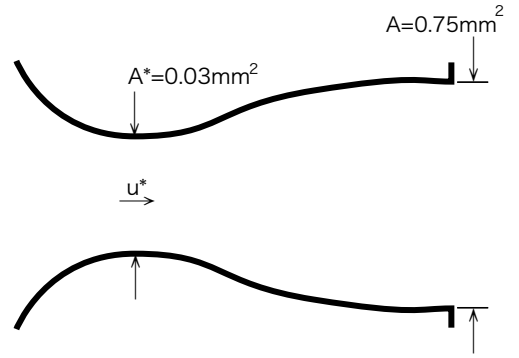


Fig. 3: Schematic of miniature supersonic nozzle

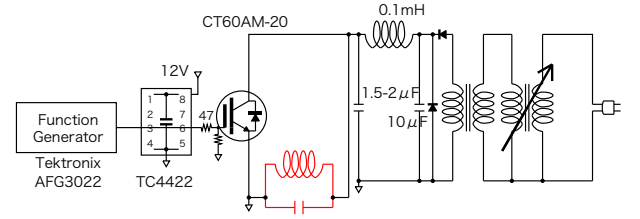


Fig. 4: Circuit diagram of induction heating

$$\dot{m} = \frac{p_0 A^*}{\sqrt{RT_0}} \sqrt{\gamma \left(\frac{2}{\gamma + 1} \right)^{\frac{\gamma+1}{\gamma-1}}} \quad (2)$$

where P_0 is the plenum pressure, T_0 is the plenum temperature. Figure 3 shows the geometry of supersonic nozzle. The tin vapor is accelerated with the nozzle, accompanied by condensation of the vapor. When we assume that the specific heat ratio to be $\gamma = 1.4$, Eq.(1) indicates $\frac{A}{A^*} = 25$ to realize $M = 5$.

We set $A^* = 0.03[mm^2]$ as the nozzle throat cross section. In addition, we used a pseudo nozzle of which shape was not contoured because tantalum was difficult materials to process.

B. Induction heating

The electric conductivity of the tantalum crucible is not infinite. Then a magnetic field invades the surface of crucible to some depth (in other words, skin depth). The eddy current Joule heats the conductor. IH heater uses the dissipation energy as the heat source.

Figure 4 shows a circuit diagram of the heating device. A high frequency electric current is provided by driving the LC resonator. We put a capacitor in the heater coil in parallel to resonantly drive the high frequency current. We operate the IGBT switch at the resonant frequency.

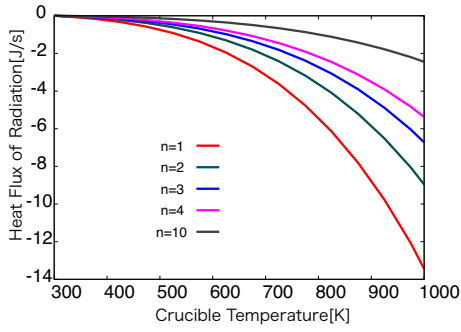


Fig. 5: Theoretical value of radiation flux versus crucible temperature (n shows the number of shield)

We considered the next three points for operation of the IH device. First, for the heating, we increase the amplitude of the electric current which flows in the heater coil. Second we avoid the audible frequency. Third, we should not heat IGBT over the operation limit to save the element.

C. Radiation shields

The radiation heat flux \dot{q} is estimated with

$$\dot{q} = \frac{\sigma}{(n+1)\left(\frac{2}{\varepsilon} - 1\right)} (T_j^4 - T_0^4) \quad (3)$$

where σ is the Stefan-Boltzmann constant, n is the number of the radiation shield, ε is the emissivity.

Silica-glass fiber tapes are used for radiation shields. Figure 5 shows the estimated heat flux of radiation. As expected, radiation is dominant in high-temperature range, because the heat flux varies with fourth power of temperature.

Temperature history of the tantalum crucible with $n = 1$ was measured as a function of input power. Figure 6 shows the temperature history of crucible with a parameter of transformer voltage. By converting a vertical axis (crucible temperature) into energy $Q = McT$ and differentiating it in time, total input power to the crucible and the energy loss power are found at each temperature. That is shown in Figure 7. The upper part of the graph shows change of the net energy at the time of induction heating. The lower part of the graph is the net energy loss when the electric transformer was turned off. In other word, the history reflects the energy flow that is lost in radiation and heat conduction. As a result, heat flux to and from the tantalum crucible was calculated with transformer voltage as a parameter.

Next, we compared the temperature history with an analytical equation of the heat losses. Factor are derived

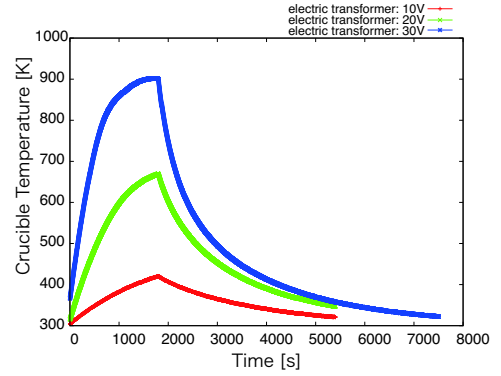


Fig. 6: Temperature history of tantalum crucible ($n = 1$)

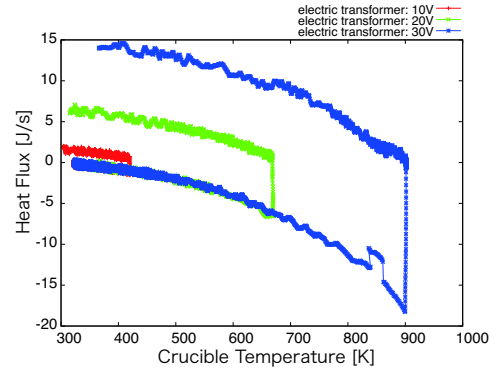


Fig. 7: Heat flux of the crucible and the energy loss

by fitting of this curve to the expression of heat conduction and radiation. They are expressed as follows,

$$\dot{q} = -a(T_j^4 - T_0^4) - b(T_j - T_0) \quad (4)$$

where a is a factor of radiation and b is a factor of heat conduction. In the case of $n = 0$, $a = 8.0 \times 10^{-11}$ and $b = 2.0 \times 10^{-3}$ are calculated (Fig. 8). By fitting the temperature history for the $n = 1$ case, tantalum crucible emissivity was estimated to be 0.52.

When we put $\varepsilon = 0.52$, the radiation flux can be calculated for $n=1$. In this condition, $a = 2.7 \times 10^{-11}$ and $b = 2.0 \times 10^{-3}$ are derived. The heat loss is calculated to be 1850[W] by extrapolating this curve to the boiling temperature 2875[K] of tin (as shown in Fig. 10).

III. CONCLUDING REMARKS

We made a heating system for Sn vapor jet formation in vacuum using induction heating. We compared the characteristic of the radiation loss with the input power to derive effective value of radiation loss of the tantalum

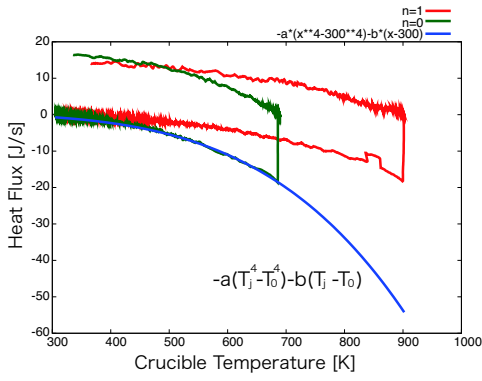


Fig. 8: Comparison of heat flux for $n = 0$ (and $n = 1$). $a = 8.0 \times 10^{-11}$, $b = 2.0 \times 10^{-3}$ are calculated.

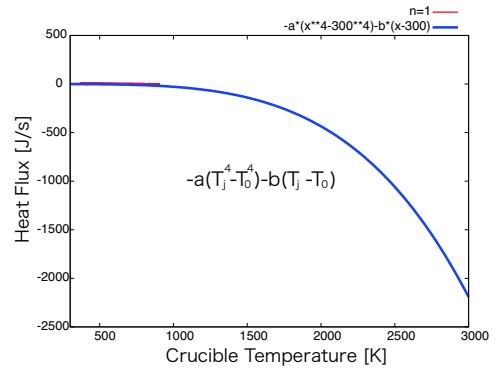


Fig. 10: Derived heat loss of the device, which indicates loss is 1850[W] at 2875[K] for $n = 1$.

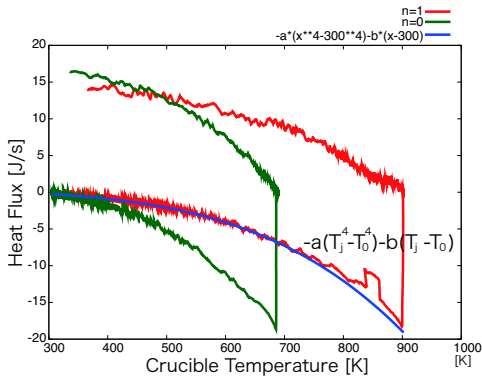


Fig. 9: Radiation flux at $\epsilon = 0.52$ and $n = 1$. $a = 2.7 \times 10^{-11}$ and $b = 2.0 \times 10^{-3}$ are derived by fitting the history.

crucible. The tantalum crucible emissivity was found to be 0.52. The heat loss are calculated to be 1850[W] by fitting and extrapolating this curve to 2875[K] at $n = 1$.

In future, we increase the number of shields and heat the tantalum crucible to the tin boiling point. Next to the jet formation, we observe the density gradient of a Sn vapor jet emitted from the supersonic nozzle by shadowgraph. We do an experiment to irradiate a laser to the tin vapor free jet and to investigate the interaction process between the laser and the supersonic free jet.

[1] Daisuke Nakamura, Tomoya Akiyama, Akihiko Takahashi, and Tatsuo Okada, JLMN-Journal of Laser Micro/Nanoengineering Vol.3, No.3, (2008)
 [2] Daisuke Nakamura, Koji Tamaru, Tomoya Akiyama, Akihiko Takahashi, and Tatsuo Okada, The Review of Laser Engineering Supplemental Volume (2008)1129
 [3] Paddy Hayden, Anthony Cummings, Nicola Murphy,

Gerry O'Sullivan, Paul Sheridan, John White, and Padraig Dunne, JOURNAL OF APPLIED PHYSICS 99, 093302 (2006)
 [4] Takeshi Higashiguchi, Masaya Hamada, and Shoichi Kubodera, Rev. Sci. Instrum. 78, 036106 (2007)

Ion Acceleration Independent of the Direction of Electric Currents in Gas-puff Z-Pinch

M. Nishio K. Takasugi* and H. Sakuma

College of Science and Technology, Nihon University, Tokyo 101-8308, Japan

** Institute of Quantum Science, Nihon University, Tokyo 101-8308, Japan*

Abstract

Ions accelerated in z-pinch experiments with either positive or negative discharge were measured by using a Thomson Parabola analyzer in order to understand the directional tendencies of the ion acceleration. Ions having energy on the order of MeV were observed in both positive and negative discharges. The velocity and energy of each ion species were measured to be considerably similar in magnitude, in spite of the difference in the polarity of the power supplies. The highest-velocity ions with different charges in each measurement lay on the constant velocity line. The model independent of the current direction should be considered as the main mechanism of ion acceleration in this study.

Keywords

z pinch, gas-puff, ion acceleration, Thomson parabola measurement

1. Introduction

Accelerated ions having energy on the order of MeV have been observed in many studies of high current experiments, particularly in the plasma foci [1, 2] and z pinch systems[3, 4]. Charged voltages of the main power supplies of these systems are several tens of kV, thus the understanding of any acceleration mechanism is required. Some acceleration models are discussed as the potential mechanisms of the acceleration, such as an induced electromotive force caused by increase of inductance[5, 6] and/or resistivity[7, 8], the kinematic effect under the calculated electric fields[9, 10], and a displacement current caused by the blocking of the conduction[11].

In all the above theories, the direction of the accelerated ions are assumed to be the same as that of the electric currents. The models of these theories are collectively called the “current-directional electric field model” in this study. Although few experimental observation[3] have reported the reversed acceleration of ions, no comparative experiments have been carried out.

Because it is difficult to measure the electric field in the fast and microscopic phenomena of pinch, the nature of the particle acceleration process by the electric field still remains undefined. Experimental observations using another approach are needed. Assuming that the above-mentioned current-

directional electric field model is the main mechanism, the reversal of polarity of the power supply should reverse the acceleration direction of ions. Accordingly, either positive or negative power supplies were examined in the same gas-puff z-pinch experiment system in this study.

2. Experimental Setups

The SHOTGUN-III device at Nihon University was used for the gas-puff z-pinch discharge in this study. The charged voltage of the bank was ± 20 kV. The initial discharge media was a puffed Ar gas (5 atm in plenum). Details of the experimental setup are discussed in the previous work[12]. According to authors, the acceleration phenomena become more predominant in the divergent gas-puff experiments than in the conventional straight gas-puff z-pinch experiments. In this study, a 30° divergent gas nozzle installed on the center conductor was used. Discharge currents were measured by two Rogowski coils (the anode and cathode Rogowski coils were located outside the vacuum chamber and between two electrodes, respectively). Soft x-ray intensity was detected by x-ray diodes (XRDs) with a Ni photocathode.

A Thomson parabola analyzer[13] was used to measure the accelerated ions. The analyzer was located on the discharge axis, and it was able to detect only ions ejected toward the axial direction

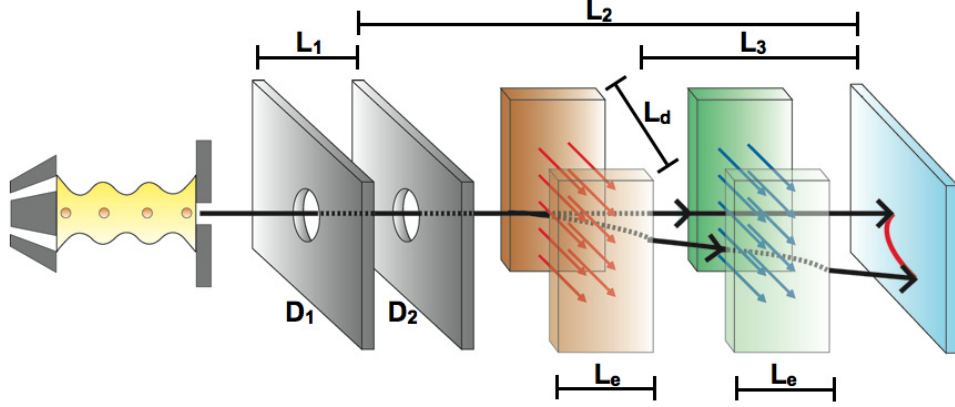


Fig. 1: Resulting injected ions through the two pinholes and are deflected by the applied electric and magnetic fields. Accelerated particles hit to the detector surface on the analyzer axis corresponding to the magnitude of energy.

from the center conductor to the opposite electrode. In both the measurements with positive and negative discharges, the intensity of the applied static electric field and pulsed magnetic flux density for parabola analysis were 5 kV per 8 mm and 0.6 T, respectively. The ejected ions went through the two pinholes, and were recorded on the detector plate (“Baryotrak-P”, Nagase-Landauer Co., Ltd.) after the deflection by the fields. After the experiments, the plates are etched by NaOH water solution during a proper interval for a visualization of particle tracks. The detector without electrical system can eliminate the electromagnetic noises. Schematic arrangement of the analyzer is shown in Fig. 1.

Analyzer parameters are shown as follows: plate size; 60×60 [mm], distance between cathode and the plate; 800 [mm], first pinhole diameter D_1 ; 1.0 [mm], second pinhole diameter D_2 ; 0.4 [mm], distance between pinholes L_1 ; 170 [mm], distance between second pinhole and plate L_2 ; 380 [mm], distance between the field and plate L_3 ; 355 [mm], distance between electrodes L_d ; 8 [mm], electrode width along the axis for both electric and magnetic fields L_e ; 25 [mm].

3. Results

Figure 2 shows the typical waveforms of discharge currents and XRD signal intensities. Electric currents were reversed by the reversal of polarity of the power supply. In both discharges, the abrupt current decrement indicated the increment of the plasma impedance by the pinch.

As shown in the cathode currents of Fig. 2, the current flowing through the pinch plasmas did not oscillate in any discharge in spite of the periodic waveforms measured by the anode Rogowski coil. This unidirectional current flow occurring in the gas-puff z-pinch implosion is called a “self-crowbar” current[14, 15]. The x-ray radiations associated with strong implosions were detected only at the first half period of the anode current waveforms. The strong implosions should have dominant influence on the particle acceleration in a pinch plasma, so it is indicated from the detection of x-ray radiations that the acceleration can occur only at the first half period of the anode current. Because the currents at the pinch timing of both the positive and negative discharges flow oppositely, as shown in the cathode current waveforms in Fig. 2, parabolas obtained in the two discharge conditions should reflect only the difference in the direction of the current flowing through the plasmas.

Figure 3 shows the resultant parabolas in the (a) positive and (b) negative discharges. The exposures of discharges for the parabola analysis were carried out over 40 shots in both measurements. The distributions obtained show three parabola curves in each figure. Judging from the comparative experiments, the difference in concentration levels (*i.e.*, ion flux) of each parabola between positive and negative discharges is minimal. Ion species were determined to be Ar^+ , Ar^{2+} , and Ar^{3+} beginning at the bottom in Fig. 3. Velocities and kinetic energies per charges of the parabolas in Fig. 3 are listed in Table 1.

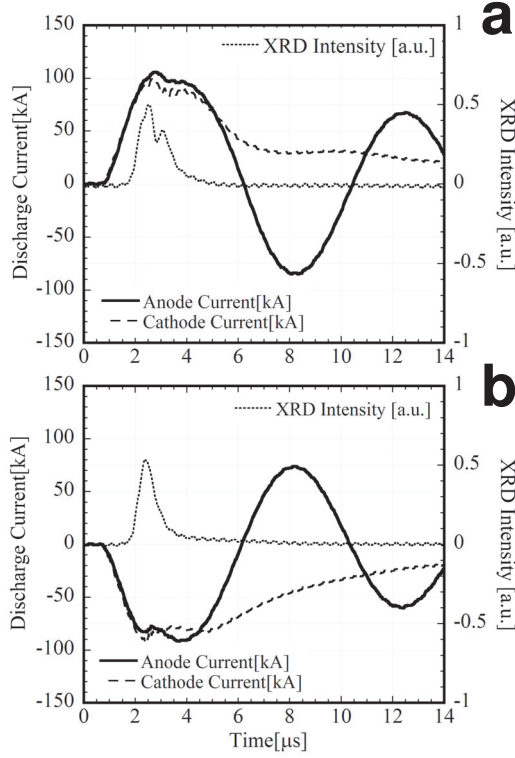


Fig. 2: Typical waveforms of discharge currents and XRD signal intensities with (a) positive and (b) negative discharges.

4. Discussions

Comparing experiments of positive and negative discharges, three results were obtained: (1) Ions having energy on the order of MeV were observed in measurements of both positive and negative discharges. (2) The velocity and energy of each ion species were measured to have similar magnitudes of accelerations both in the same and opposite direction of the electric currents, as shown in Table 1. (3) The highest velocity ions with different charges in each figure lay on the constant-velocity lines (eq. 6 in ref.[13]). These results show that the direction of the acceleration could not depend on the direction of currents. This contradicts the existing current-directional electric field model, because ions should not be accelerated toward the opposite direction to the supposed strong electric fields dependent on the current direction.

The reasonable mechanisms of particle acceleration from the z-pinch plasma in this study are concluded to have no dependence of the electric current direction. The models of the current independent model listed previously are evaluated as follows.

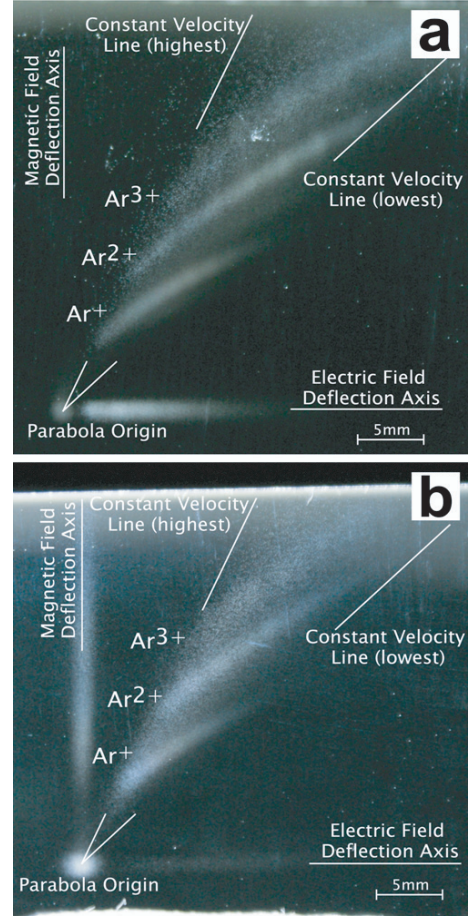


Fig. 3: Resultant parabola curves in measurements with (a) positive and (b) negative discharges.

(1) Thermal energization with the fluid dynamical instabilities of sausage instability[16] and/or kink instability[17]. However it cannot explain sharp boundary of upper velocity limit. (2) Trapping effect by the axially propagating potential trough generated in the two-stream instability [18] It can explain sharp boundary of upper velocity limit as the phase velocity of propagating potential, however may not explain the gradual boundary of lower velocity regime. (3) Mechanical reflection by the imploding current sheet[19] It can explain sharp boundary of upper velocity limit and also can explain current-directional independency, in addition, may explain the anisotropy of axial ion distribution.

The third model, that is mechanical reflection model proposed by Gureev (1980), is considered to be the most reasonable model. In short time of pinch phenomena, the strong acceleration of particles may need multiple head-on collisions with imploding wall like first-order shockwave Fermi ac-

Table 1: Highest and lowest velocities and kinetic energies per charges of parabolas in Fig. 3. Units of velocities v and energies per charges E/Z are “km/sec” and “MeV/Z”, respectively.

	Positive		Negative	
	max v max E/Z	min v min E/Z	max v max E/Z	min v min E/Z
Ar ⁺	1.9×10^3 0.8	1.0×10^3 0.2	1.9×10^3 0.7	1.1×10^3 0.2
Ar ²⁺	2.0×10^3 0.4	1.0×10^3 0.1	2.0×10^3 0.4	1.1×10^3 0.1
Ar ³⁺	2.1×10^3 0.3		2.0×10^3 0.3	

celeration in astrophysics. In the collisional z-pinch plasma, particles in the hollow area of radially imploding annular cylinder can always obtain the gains of kinetic energy by the multiple head-on collisions. Energy distributions of particles indicates power-law condition in general statistical acceleration (even in the first order Fermi process), and maximum energies exist because that some realistic velocity of shockwave discovered in astrophysics may control the limitation of accelerated ions. While, the accelerations in this study may be limited by another process, because the configuration of reflection surface is different from that in the astrophysical condition. Multiple reflection process in the self-contracting plasma have to be discussed. Because the mechanical acceleration proposed by Gureev (1980) has not take the detailed reflection process into account (only ideal elastic collisions between ions and a rigid wall), the reflection processes with the magnetic wall is needed to be discussed with the further experimental results.

5. Conclusion

Energetic ions of MeV order were observed in the gas-puff z-pinch experiments with divergent gas nozzle. Ions accelerated to the similar velocity both in the positive or negative discharge. Ion acceleration in the divergent gas-puff z-pinch experiments of this study should be caused by the acceleration mechanism independent of current direction not by the current-directional electric field model. A reasonable mechanism of the particle acceleration are concluded to be independent of the electric current

direction. Pointed out as an example of the physical processes independent of the current direction, a mechanical reflection effect caused by the radially and axially moving cylindrical magnetic wall or a trapping effects caused by a potential trough propagating in symmetrical directions along the axis may have an important role in acceleration.

References

- [1] A. Moser *et al.*, J. Appl. Phys. **53**, 2959 (1982).
- [2] H. Heo and D. K. Park. Physica Scripta **65**, 350 (2002).
- [3] X. M. Guo and C. M. Luo, J. Phys. D Appl. Phys. **29**, 388 (1996).
- [4] C. Luo *et al.*, IEEE Trans. Nucl. Sci. **28**, 1599 (2000).
- [5] O. A. Anderson *et al.*, Phys. Rev. **110**, 1375 (1958).
- [6] Y. Kondoh and K. Hirano, Phys. Fluids **21**, 1617 (1978).
- [7] S. P. Gary, Phys. Fluids **17**, 2135 (1974).
- [8] M. Tanimoto and K. Koyama, Jpn. J. Appl. Phys. **21**, L491 (1982).
- [9] S. P. Gary and F. Hohl, Phys. Fluids **16**, 997 (1973).
- [10] M. G. Haines, Nucl. Instru. Meth. **207**, 179 (1983).
- [11] B. A. Trubnikov and S. K. Zhdanov, Sov. Phys. JETP **43**, 48 (1976).
- [12] K. Takasugi and E. Kiuchi, Plasma Fusion Res. Rapid Commun. **2**, 036 (2007).
- [13] M. J. Rhee, Rev. Sci. Instru. **55**, 1229 (1984).
- [14] K. Takasugi *et al.*, Jpn. J. Appl. Phys. **31**, 1874 (1992).
- [15] H. Akiyama *et al.*, Rev. Sci. Instru. **61**, 1344 (1990).
- [16] V. V. Vikhrev and V. D. Korolev, Plasma Phys. Report, **33**, 356 (2007).
- [17] T. Haruki *et al.*, Phys. Plasmas, **13**, 082106 (2006).
- [18] S. P. Gary, and H. W. Bloomberg, Appl. Phys. Lett., **23**, 112 (1973).
- [19] K. G. Gureev, Sov. Phys. Tech. Phys., **25**, 192 (1980).

Characteristics of Nano-second Pulsed Discharge Using All Solid State Pulsed Power Generator

Ippei Yagi, Koichi Takaki, Takao Namihira*, Ryo Ono**

Department of Electrical and Electronic Engineering, Iwate University

**Bioelectronics Research Center, Kumamoto University*

***Department of Advanced Energy, The University of Tokyo*

ABSTRACT

All solid state inductive energy storage (IES) pulsed power generator demonstrated to generate output voltages with 5-41 ns in pulse rise time and up to 26.4 kV in peak voltages. The pulsed power generator consisted of a capacitor, a MOSFET switch, a pulse transformer and semiconductor opening switches. The output voltage of the pulsed power generator was applied to a coaxial chamber consisting of a center wire of 1 mm in diameter and an outer electrode of 20 mm in diameter. An atmospheric pressure air was fed into the chamber to generate streamer discharges homogeneously. The streamer-to-glow transient was observed by ICCD and streak cameras at various peak voltages and pulse rise times. The discharge impedance rapidly decreased with the streamer-to-glow transient at higher peak voltage. The streamer propagation velocity increased with shortening rise time of the pulsed voltage.

Keywords

All solid state IES pulsed power generator, nano-second pulse, semiconductor opening switch, streamer-to-glow transient, streamer velocity.

1. Introduction

Non-thermal plasma in atmospheric pressure is a promising technology for the decomposition of environmental pollutants and in medical treatment [1-3]. Non-thermal plasma driven by pulsed streamer discharge has received great interest for many years as an abundant radical source. The streamer characteristic is a key factor in improving radical production. For this reason, it is necessary to study the propagation mechanism of the pulsed streamer discharge. The streamer discharge was originally proposed by Loeb [4], Meek [5], [6], Raether [7]. The electric field at the head of and the propagation velocity of the streamer were theoretically studied using computer simulations [7-11].

In this paper, an all solid state inductive energy storage (IES) pulsed power generator demonstrated to control output voltage waveforms such as peak

voltage and rise time. Using the pulsed power generator, the streamer discharges were generated in a coaxial discharge chamber at various rise times and peak voltages. The flaming images of the discharge were observed for streamer-to-glow transient using ICCD camera. The streamer propagation of the streamer discharge was observed using a streak camera to obtain velocity of the streamer heads.

2. Experimental Setup

2.1 Pulsed Power Generator

Figure 1 shows the all solid state IES pulse power generator circuit employed in the experiment. The pulse power generator was combined primary and secondary circuit by magnetic core (pulse transformer: PT). The primary and the secondary circuit consisted of a energy storage capacitors C_1 and C_2 , two of

inductors L_1 and L_2 , MOSFET as a closing switch, and a semiconductor opening switch SOS. Fast recovery diodes K100UF (Voltage Multiplier Inc., 10 kV maximum voltage, 100 A maximum current, 100 ns interruption time of reversed current) were used as a semiconductor opening switch and were connected up to five in series and four in parallel to realize high-voltage and large current operation of the SOS.

2.2 Discharge Observation System

Figure 2 shows a schematic diagram of the experimental setup for discharge observation. A coaxial cylindrical chamber was used as the discharge electrode to observe the pulsed streamer discharge. A center electrode, having 1 mm in diameter and 10 (or 20) mm in length, was connected to high-voltage side of the pulsed power generator. The outer electrode, 20 mm in diameter, was grounded. The chamber was filled with dry air at a gas flow rate of 1.0 L/min at atmospheric pressure. A high speed gated CCD camera (C8484-05G01, Hamamatsu Photonics K. K.) with

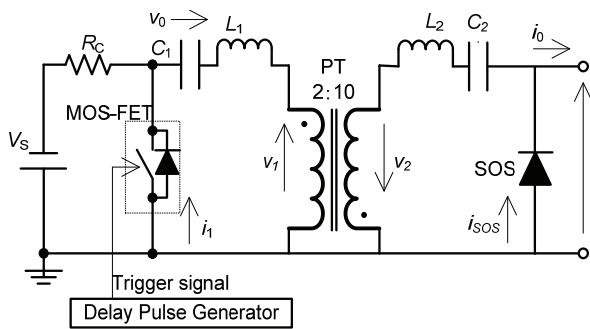


Fig. 1 All solid state IES pulsed power generator using semiconductor opening switch diode.

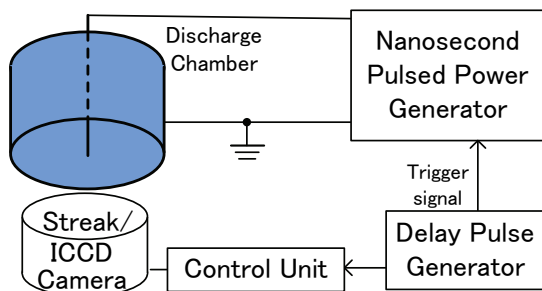


Fig. 2 Observation system for pulse discharge.

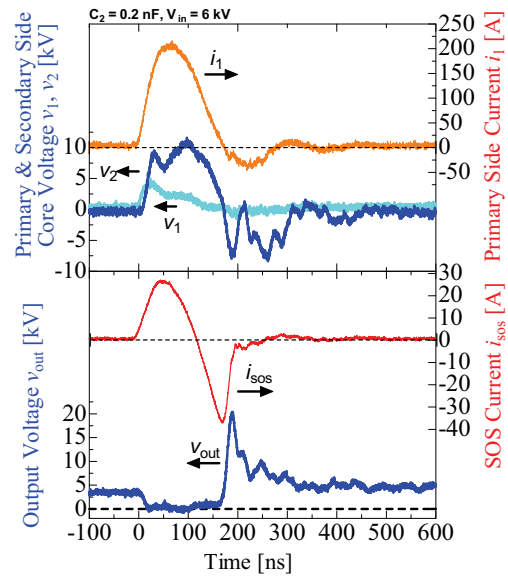


Fig. 3 Waveforms of primary and secondary sides core voltages v_1 and v_2 , primary side current i_0 , output voltage v_0 and SOS current i_{sos} .

MCP (micro channel plate, maximum gain: 10,000) was used to observe the flaming image of light emission from the discharge. The exposure time was fixed at 5 ns. A fast-dynamic-range streak camera (C7700, Hamamatsu Photonics K.K.) consisting of a sensitive microchannel-plate with a maximum gain of 10,000 was used to observe the streamer discharge propagation in the coaxial electrode. The slit of the streak camera was adjusted to focus from the center electrode to the outer electrode. A single pulse was applied to the discharge electrode to observe the streamer images. These cameras were synchronized with the discharge by pulse delay generator (DG535, Stanford Research Systems Inc.).

3. Results and Discussion

3.1 Behavior of Pulsed Power Generator

Figure 3 shows typical waveforms of primary and secondary sides core voltage v_1 and v_2 , primary side current i_0 , output voltage v_0 and SOS current i_{sos} without connecting to any load at charging voltage of -6 kV. The circuit parameter were $C_1=2$ nF, $C_2=0.2$ nF, $L_1=2$ μ H and $L_2=0$ μ H. The primary

capacitance C_1 was fixed to be 2 μH in all experiment. After the MOSFET switch is closed at 0ns, the voltage is applied to primary side of the magnetic core. The voltage of the primary side core is slightly amplified to 10kV of peak volatege at secondary side of the magnetic core. As the result, the charges of the primary capacitor C_1 are transferred to the secondary capacitor C_2 with flowing current in forward direction of the SOS diode. After the magnetic core saturates with magnetic flux in the core and the voltage of primary side magnetic core drops, the reverse direstion current starts to flow to the SOS diode at 117 ns. From 168 ns, the reverse direction current is interrupted rapidly by SOS diode. As the result, a pulsed voltage is generated as induction with electromotive force by rapid interruption of the current.

3.2 Discharge properties

Figure 4 shows waveforms of output voltage v_{out} and current i_o , consumed energy between electrodes and impedance of dicharge. A diameter of 10 mm was used as outer electrode. The consumed energy was calcultaed to integrated value of the instantenous power calculated by multiplying the output voltage v_{out} by the output current i_o . The impedance of discharge was calculated by dividing output voltage v_{out} by discharge current. The discharge current was estimated by subtracting displacement current of the chamber from the output current i_o . The applied peak voltages are 10 and 12 kV, respectively. The dashed lines represent 50 ns and 66 ns, respectively.

In the case of 12 kV, the output current increases up to apploximately 10 A at 66 ns. The impedance of discharge decreases to 860 Ω , the value is less than tenth part of the impedance of 10 kV at 66 ns. The impedance is agree with typical value of glow phase discharge [12].

Table 1 shows flaming image of the pulsed discharge using ICCD camera. The applied voltages are 10 kV and 12 kV, respectively. The

times of 50 and 66 ns on the photographs correspond to the times on the figure 4. The flaming images of 10 and 12 kV at 50 ns shows the light emission from the streamer discharge propagating from the center wire electrode to

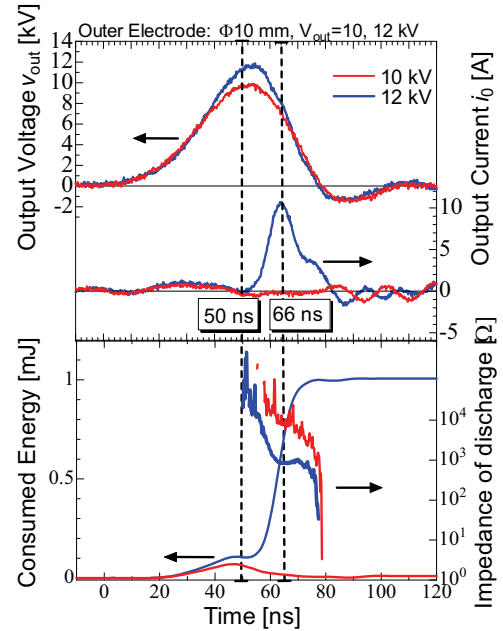
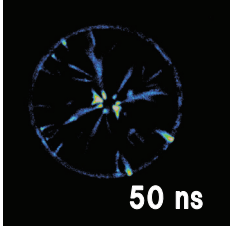
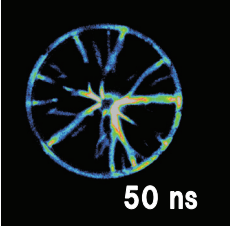
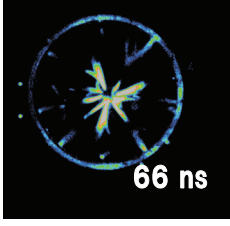
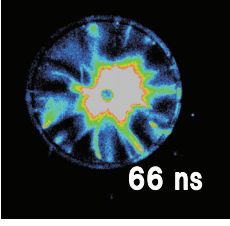


Fig. 4 Waveforms of output voltage v_{out} , current i_o , consumed energy in electrodes and impedance of discharge.

Table. 1 Framing images of pulsed discharges using ICCD camera (Left: 10 kV, Right: 12 kV of maximum applied voltage, 5 ns of gate time).

Voltage: 10kV	12kV
 50 ns	 50 ns
 66 ns	 66 ns

the outer electrode. The steamer head, consisted of high energy electron, is the area of high electric field and effective for dissociation and ionization of moleculars of the gases. At 66 ns, the glow phase, a bright and homogeneous light emission around the center wire electrode, is observed at 12 kV of applied voltage, whereas the length of light emission of the discharge decreases at 10 kV of applied voltage.

3.3 Streamer Velocity

Figure 5 shows the waveforms of the output voltage v_{out} , which is applied to the center electrode, and the output current i_{out} . The rise time of the output voltage is controlled with capacitance and inductance of the all solid state IES pulsed power circuit as described in figure 1. The primary and secondary loop inductances, L_1 , L_2 , and capacitances, C_1 , C_2 , are chosen as (a) 2 and 0.1 μ H, 2 and 0.2 nF; (b) 2 and 8 μ H, 2 and 2 nF; and (c) 10 and 4 μ H, 2 and 2 nF, respectively. The rise times of the output voltage of 16.5 kV are obtained as (a) 7.2, (b) 23.4, and (c) 40.2 ns for the various circuit inductances and capacitances. Here, the pulse rise times are defined by durations of 10-90% of peak voltage.

Figure 6 shows the streak images of the streamer propagation using the streak camera at an

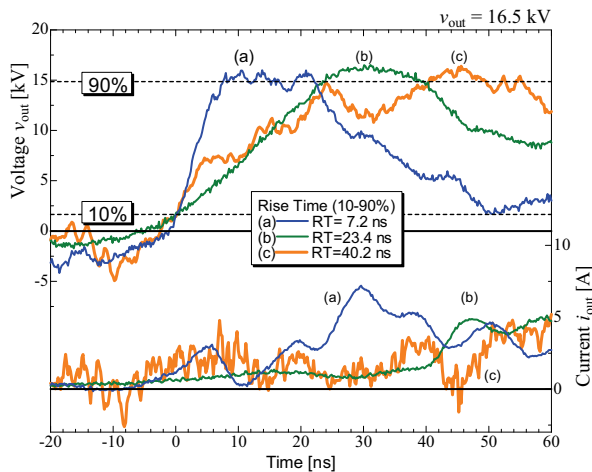


Fig. 5 Waveforms of output voltage v_{out} and current i_o at applied voltage of 16.5 kV with various pulse rise time; (a) 7.2 ns, (b) 23.4 ns, (c) 40.2 ns.

applied voltage of 16.5 kV with rise times of (a) 7.2 ns, (b) 23.4 ns and (c) 40.2 ns. The horizontal direction of the streak images corresponds to the position within the gap between the electrodes. The left and right ends of the streak images are the surfaces of the center electrode and the grounded cylinder, respectively. The vertical direction indicates the time progression of the discharge emission and the time scale corresponding to figure 5.

The streamer discharges appear near the center electrode and develop toward the outer cylindrical electrode. The streamer heads reached the outer electrode at (a) 10 ns, (b) 30 ns and (c) 47 ns after the ignition. The discharge mode after the full development of the streamer across the gap between the electrodes changed from streamer phase to glow phase with stronger emission near the center electrode [12]. The average propagation velocity of the streamer head is given by the following equation:

$$v_{streamer} = L/t_0 \quad (1)$$

where L and t_0 are the gap distance and the propagation time, respectively. The velocities are obtained as (a) 0.92, (b) 0.79 and (c) 0.49 mm/ns, respectively. The streamer velocity increased with shorting rise time of the applied pulsed voltage. Additionally, the emission intensity of streamer head increases with shorting rise time of the applied pulsed voltage. High emission intensity is related with high frequency of dissociation and ionization. Therefore, it is considered that the shorten rise time contributes to high degrees of the ionization rate.

Figure 7 shows streamer velocity as a function of pulse rise time with various applied voltages. The applied voltages are changed in the range from 13.2 to 26.4 kV. Each plot represents the average value of five measurements. The standard deviations of each value are less than 0.2. For each peak voltage, the shorter rise time increases the streamer velocity. The influence of pulse rise time increases under higher peak voltage.

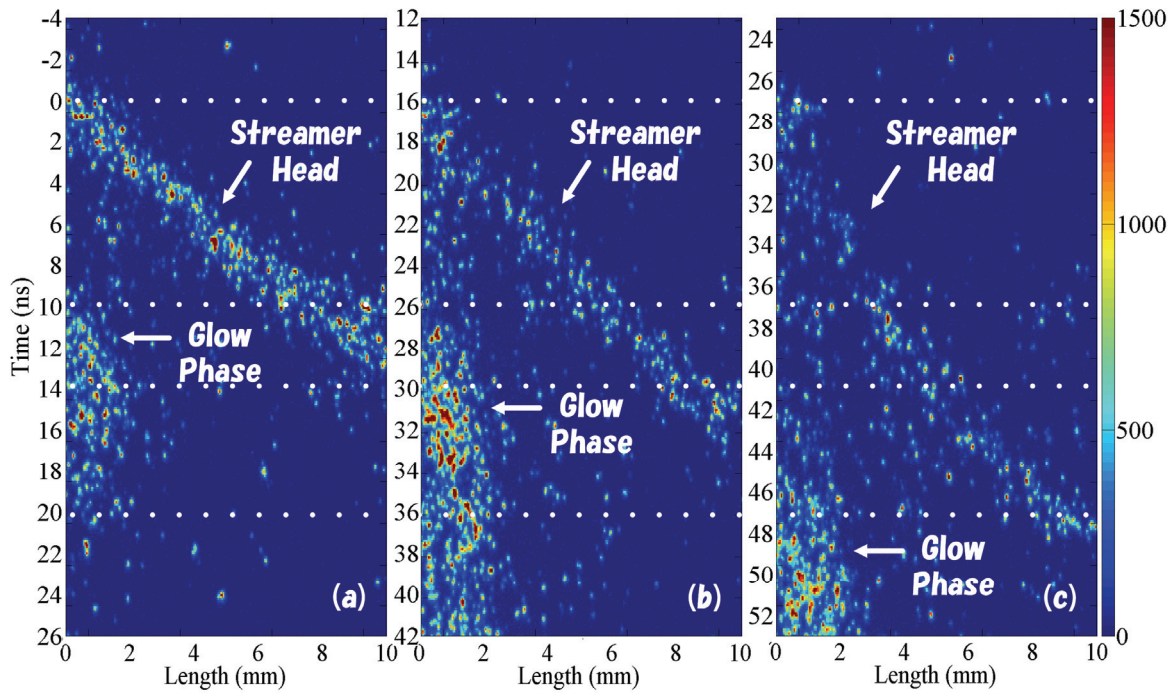


Fig. 6 Streak images of streamer propagations at applied voltages of 16.5 kV with rise times of (a) 7.2 ns, (b) 23.4 ns, and (c) 40.2 ns by changing the circuit inductance and capacitance according to Fig. 5.

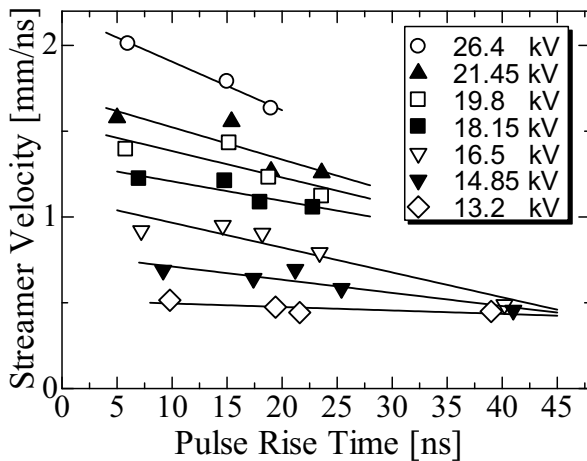


Fig. 7 Streamer velocity as a function of pulse rise time with various applied voltages.

Meek mentioned that “A streamer will develop when the radial field about the positive space charge in an electron avalanche attains a value of the order of the external applied field” [5]. Thus, the results indicate that the differences of propagation velocities with several pulse rise times are due to an increase in the electric field during streamer formation and propagation.

4. Conclusion

All solid state IES pulsed power generator using semiconductor opening switch was demonstrated to generate the nano-second pulse voltage in the range from 5 to 41 ns in pulse rise time. The streamer-to-glow transition and impedance of discharge are changed with applied voltage. Especially, in the case of high voltage, the discharge phase shifted streamer-to-glow with decreasing the impedance. The shorter rise time contributes to the increase of the streamer velocity.

Reference

- [1] M.B. Chang and J.S. Chang, “Abatement of PFCs from Semiconductor Manufacturing Processes by Nonthermal Plasma Technologies: A Critical Review”, *Ind. Eng. Chem. Res.*, 45, 4101-4109 (2006).
- [2] K. Takaki, M. Hosokawa, T. Sasaki, S. Mukaigawa, T. Fujiwara, “Production of atmospheric -pressure glow discharge in nitrogen using needle-array electrode”, *Appl. Phys. Lett.*, 86, 151501-1-3 (2005).
- [3] G. Fridman, G. Friedman, A. Gutsol, A. B. Shekhter, V. N. Vasilets, A. Fridman, “Applied Plasma Medicine”, *Plasma Process. Polym.*, 5,

503-533 (2008).

- [4] L.B. Loeb, "Ionizing waves of potential gradient", *Science*, vol. 148, p.1417, (1965).
- [5] J.M. Meek, "A theory of spark discharges," *Phys. Rev.*, vol. 57, p. 722 (1940).
- [6] J.M. Meek and J.D. Craggs, "Electrical Breakdown of Gases", Oxford, U.K.: Clarendon, pp. 251–290 (1953).
- [7] H.Raether, *Electron Avalanches and Breakdown in Gases*. London, U.K.: Butterworth (1964).
- [8] A. A. Kulikovskiy, "Positive streamer in a weak field in air: A moving avalanche-to-streamer transition", *Phys. Rev. E*, vol. 57, no. 6, pp.7066–7074 (1998).
- [9] O. Eichwald, O. Ducasse, D. Dubois, A.Abahazem, N. Merbahi, M. Benhenni and M.Yousfi, Experimental analysis and modeling of positive streamer in air: towards an estimation of O and N radical production, *J. Phys. D: Appl. Phys.*, Vol.41, 234002 (2008).
- [10] F. Tochikubo and H. Arai, "Numerical Simulation of Streamer Propagation and Radical Reactions in Positive Corona Discharge in N₂/NO and N₂/O₂/NO", *Jpn. J. Appl. Phys.* 41 pp. 844-852 (2002).
- [11] A Komuro, R Ono and T Oda, "Kinetic model of vibrational relaxation in a humid-air pulsed corona discharge", *Plasma Sources Sci. Technol.*, 19, 055004 (2010).
- [12] D. Wang, M. Jikuya, S. Yoshida, T. Namihira, S. Katsuki, H. Akiyama, "Positive- and Negative-Pulsed Streamer Discharges Generated by a 100-ns Pulsed-Power in Atmospheric Air", *IEEE Trans. Plasma Sci.*, 35, 4, pp. 1098-1103 (2007).

Electrical Conductivity Measurements of Warm Dense Matter with Semi-rigid Vessel

Hiroki Sakai, Kotaro Iwasaki, Mitsuo Nakajima, Tohru Kawamura, and Kazuhiko Horioka*
*Department of Energy Sciences, Tokyo Institute of Technology,
Nagatsuta 4259, Midori-ku, Yokohama, 226-8502, Japan*

Thin wires were rapidly vaporized in capillaries by means of a short pulse current. The wires evolved to plasma through a warm dense matter region. The inner wall of the semi-rigid capillaries confined a homogeneous plasma for a short time, which enabled us to make accurate measurements of the electrical conductivity, density and input energy. Electrical conductivities of the dense plasmas were compared with conventional theoretical estimations and those of previous experiment as a function of electrical input energy and density.

Keywords: Warm Dense Matter, Wire Explosion, Electrical Conductivity, Pulse-Power

I. INTRODUCTION

State of matter can be explained in a density-temperature diagram. In the low temperature and high density regime (-10^5 K, $10 - 10^4$ g/m³), that is, in a warm dense matter (WDM) region, there are not appropriate equation of state (EOS) and transport coefficient. When a solid is abruptly heated, the matter changes from solid state to plasma through a warm dense state. Therefore, when we study the evolution of matter in a broad parameter region, it is crucially important to study the WDM. Properties of matter in a warm dense state are of interest, specifically, concerning interiors of giant planet (e.g., Jupiter) and hydrodynamics of fuel pellet of inertial confinement fusion.

Recently, because energy drivers such as fast pulse power device, ion beam have been developing, so we are capable of producing a warm dense state with a simple small scale device. However, it is difficult to well confine the warm dense plasma and to accurately measure the values because production of a warm dense state is accompanied with high pressure over GPa. As a result, appropriate experimental data in this region have yet to be obtained so much, and there are few researches which accurately evaluate relations between physical parameters and transport coefficient. In this research, we produced a warm dense matter using wire discharge in a semi-rigid capillary so that we extract experimental data in a wall defined condition.

Wire discharge in a semi-rigid capillary enabled us to produce a well-defined plasma while the inside of the capillary is filled with a plasma. A well-defined plasma provided us with input energy and electrical conductivity from I-V properties as well as plasma density from plasma radius. Electrical conductivity, which is one of the transport coefficients, can be expressed as a function of internal-energy and density. To make the scaling law, it is important to estimate electrical conductivity as a function of internal-energy and density over a wide parameter region. In fact, the previous experiment per-

formed in our laboratory; wire discharge in water, indicated that electrical conductivity has a minimum value that supposedly corresponds to metal-nonmetal transition around $1/30 \rho_s$ (ρ_s : solid density). In this study, we evaluate the electrical conductivity as a function of input energy and density. In addition, the results of wire discharge in the semi-rigid capillary are compared with those in water and conventional theoretical estimations.

II. EXPERIMENTAL SETUP AND METHOD

The experimental setup is shown in Fig.1. Current is driven by capacitors coaxially connected, totaling 3.2 μ F and is switched by a pressurized spark-gap switch. The inductance of the circuit, exclusive of the wire load, is estimated to be about 70 nH. The voltage and current through the wire were measured, respectively with a high voltage probe, and a Rogowski belt. The Rogowski belt surrounds the wire, directly giving current waveform. The pure aluminum wire used for the discharge, whose diameter is 50 μ m or 100 μ m, is thin enough for us to disregard skin effect, and therefore the input energy is expected to be uniformly put into the wire. Thanks to these things, we were capable of evaluating the input energy and the resistivity as a function of time, based on the measured voltage and current.

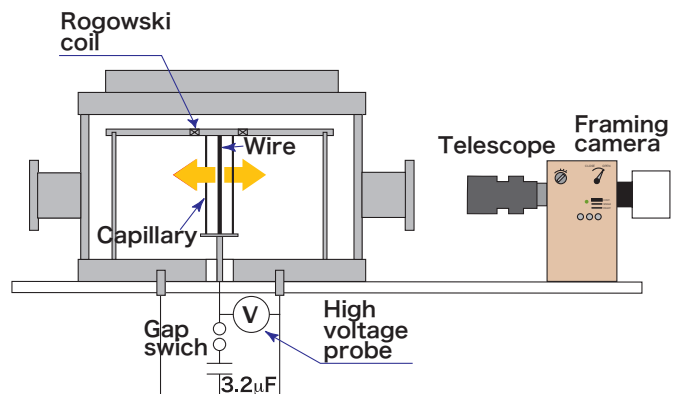


Fig.1 Schematic diagram of experimental setup

*Electronic address: khorioka@es.titech.ac.jp

First, the resistive part $V_i(t)$ of the voltage applied to the wire plasma is described as follows.

$$V_i(t) = V_o(t) - L \frac{dI(t)}{dt} \quad (1)$$

where $V_o(t)$ is the measured voltage, $I(t)$ is the measured current, L is the stray inductance of the circuit.

Next, the input energy $E(t)$ and the resistivity $R(t)$ are simultaneously calculated using $V_i(t), I(t)$ as follows,.

$$E(t) = \int_0^t V_i(t)I(t)dt \quad (2)$$

$$R(t) = \frac{V_i(t)}{I(t)} \quad (3)$$

Here, if we assume that the axially symmetrical plasma is produced in the capillary, the electrical conductivity σ is described as below using eq. (3) for the resistivity,

$$\sigma = \frac{l}{\pi r(t)^2 R(t)} \quad (4)$$

where l is the wire length, $r(t)$ is the plasma radius. In this study, we regarded the plasma radius $r(t)$ is constant ($r(t) = 0.8$ mm) and corresponding to that of a semi-rigid glass capillary. The glass capillary allowed us to produce the well-defined plasma with low cost as well as to observe the wire plasma radius with a fast framing camera due to transparency of the capillary.

III. I-V WAVEFORM PROPERTIES AND EVALUATION FOR DISCHARGE

Typical I-V waveforms which provided us with $I(t)$ and $V_o(t)$, are shown in Fig.2. As for the features of the waveforms, we could make sure that both the voltage and the current have the sharp peak, which indicate that the energy was firstly deposited into the Al wire. After this first peak, the voltage and the current, respectively, gradually decreased and increased with time. This fact indicates that the Al wire evolved by the input energy through a WD state from gas phase to a plasma state in which conductivity increases with temperature.

We determined the time region when the capillary was filled with a dense plasma, using the I-V waveforms and the images obtained by framing camera. We could make sure that the I-V waveforms are highly reproducible by repeating the discharges in the same experimental condition. Consequently, they enabled us to identify the region in which a well-defined plasma was produced. Indeed, we determined the interval from $0.5 \mu s$ till $1.5 \mu s$ as the region where we ought to observe. The start of the available period ; $0.5 \mu s$ was determined by appearance of the behavior like metal-insulator transition that previous experiment (wire discharge in water) implied. The

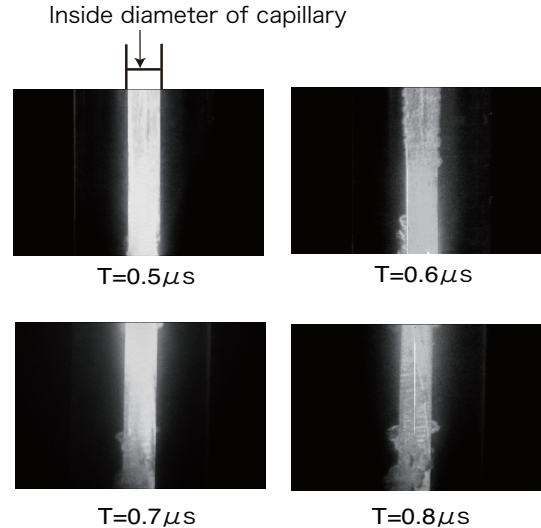
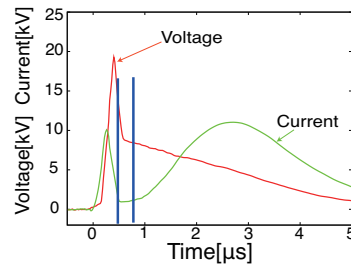


Fig.2 Framing images of wire/plasma evolution in Pyrex-capillary

end of available period ; $1.5 \mu s$ was determined by the moment when some waveforms began to subtly change, which might mean macroscopic destruction of the capillary, namely, the limit that the capillary was able to confine the plasma.

In order to confirm whether the inside of the capillary was certainly filled with a plasma within the given interval, we observed the plasma behavior with the framing camera in the time region from $0.5 \mu s$ till $0.8 \mu s$. The transparency of the glass capillary made it possible for us to observe the outside of the capillary. As a result, we could make sure that the well-defined plasma was produced as Fig.2 shows. Although in the image at $t = 0.8 \mu s$ it seems that scattered light came out of the capillary inner wall, the I-V waveforms were quite reproducible.

IV. EXPERIMENTAL RESULTS AND CONSIDERATION

In this research, we used two types of aluminum wires; $100 \mu m$, $50 \mu m$ in diameter so as to produce various plasma density patterns (6 patterns). For example, when we use one to three aluminum wires of $100 \mu m$ in diameter, the plasma density is produced around $1/60 \rho_s, 1/30 \rho_s, 1/20 \rho_s$ (ρ_s :solid density) respectively, when the inside

of the capillary was filled with a plasma. Similarly, in the case of one to three aluminum wires of $50\ \mu\text{m}$ in diameter, the produced plasma density are around $1/255\ \rho_s, 1/125\ \rho_s, 1/85\ \rho_s$ respectively. Typical I-V waveforms for the respective plasma densities are indicated in Fig.3. We found the time histories depend on the density and could confirm highly reproducible I-V waveforms. Their patterns were qualitatively similar ; a sharp peak in the initial phase, its collapse, and current evolution. Therefore, we were not only able to obtain the well-defined plasma in the glass capillary within the density region which ranges from $1/255\ \rho_s$ to $1/20\ \rho_s$, but we were capable of getting input energy and electrical conductivity based on the Eqs.(2) and (4).

The input energy versus conductivity of aluminum wire is shown in Fig.5, which shows change of the conductivity versus the input energy. We determined the available region for estimation of conductivity and input energy to be a period while the inside of the capillary was filled with a plasma. Considering the volume of the capillary, the wire mass and the input energy per unit mass of the wire, the relations between plasma states and conductivity are uniquely determined. Fig.5 indicates that conductivity has a minimum at a specific input energy point for respective plasma densities.

As the conductivity and the input energy per unit mass and density of Al plasma were well defined, we could get

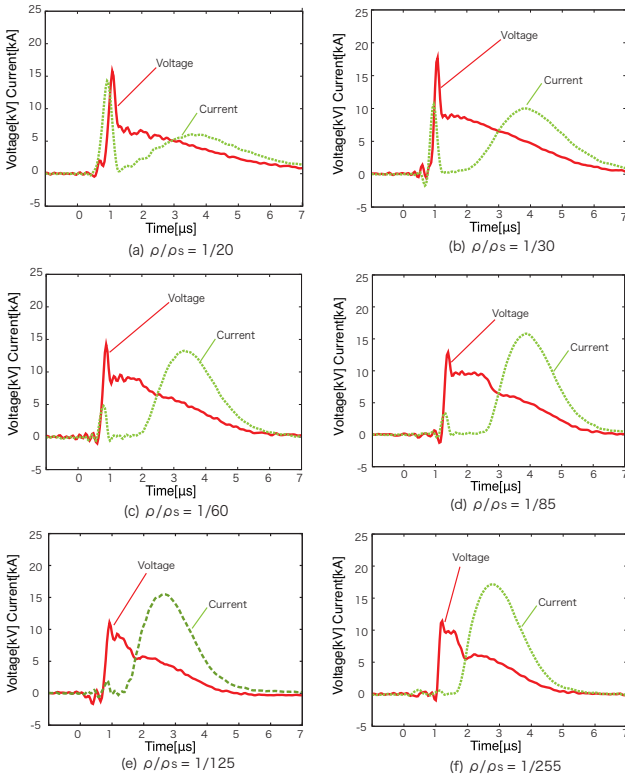


Fig.3 Typical waveforms of voltage and current of Al-wire discharges ($V_c = 10\ \text{kV}$, in glass capillary)

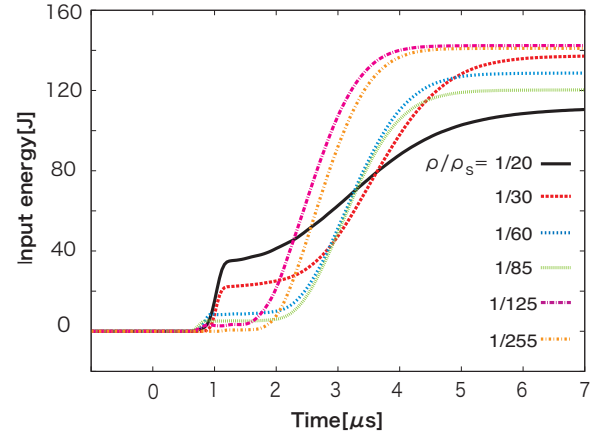


Fig.4 Input energy history of wire discharge

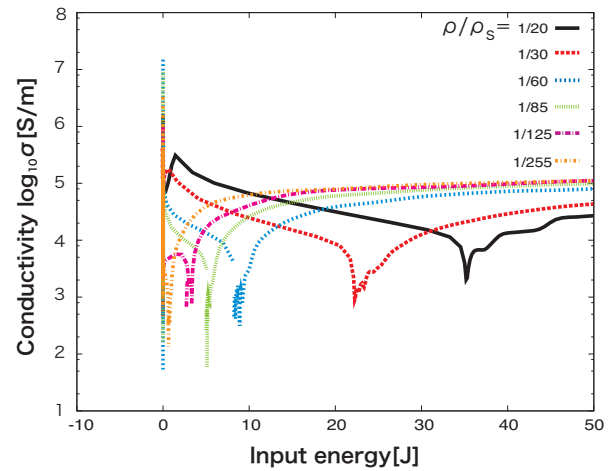


Fig.5 Input electric energy versus estimated conductivity of Al-wire/plasma

density dependence of the conductivity with a parameter of specific energy density.

We could make sure that in the case of $15\ \text{kJ/g}$, conductivity has a minimum around $1/85\ \rho_s$. We think that this result implied that metal-insulator transition having been alluded by the previous experiment appeared in the low input energy per unit mass, that is, in the low temperature region. The minimum of conductivity disappears with increase of specific energy density as shown by the data in Fig.6 for $47\ \text{kJ/g}$. In fact, this tendency that minimum of conductivity is gradually disappearing with temperature increase is predicted by quantum molecular dynamics (QMD) simulation.

We compared our experimental results with conventional theoretical models ; by Spitzer, Ichimaru and Lee-More, together with, previous experimental results, as Fig.6 shows. These theoretical models effectively include various effects, for instance, collisions which are involved in electron - electron, electron - ion, electron - neutral, and degeneracy effect appearing in the vicinity of the

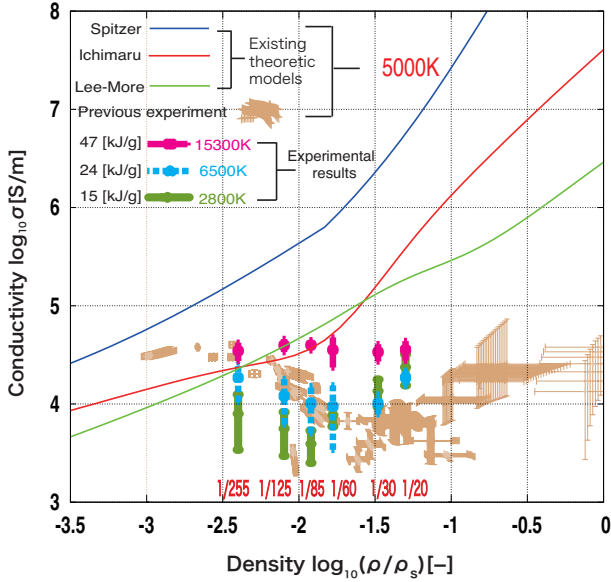


Fig.6 Comparison between experimental results and theoretical models, together with previous experimental results

solid density. As warm dense matter state is located in the region between solid and plasma, we need to consider these complicated effects. However, it is extremely difficult to self-consistently treat these effects in WDM physics even using theoretical models like these.

The data given as 5000 K in Fig.6 is based on the temperature estimated by spectroscopic measurement which

was obtained in previous experiment. When we approximately estimate the temperature corresponding input energy per unit mass obtained from our experiment, the temperatures of 2800 K, 6500 K, 15300 K were obtained. Comparing our experimental result with previous experimental one, we could make sure that the data at the temperature of 5000 K are corresponding to those between 2800 K and 6500 K. This means conductivity derived from our experiment was about 1/10 of conventional theoretical predictions and it has a minimum at $1/30 \rho_s$ - $1/100 \rho_s$.

V. CONCLUSION

We produced well-defined dense plasma using wire discharge in the semi-rigid capillary. Using the I-V waveforms, we were capable of getting input energy and conductivity with a parameter of density. Consequently, we could confirm that conductivity of Al plasma depends on input energy and plasma density. Obtained results indicate that the conductivity has a minimum at specific density at low temperature and it disappears with temperature rise. These results are consistent with the recent results by QMD simulations.

VI. ACKNOWLEDGEMENT

This work is partly supported by Grant-in-Aid for Scientific Research (A) from the Japan Society for the Promotion of Science (JSPS).

-
- [1] K.Horioka, T.Kawamura, M.Nakajima, et.al., *Nucl. Instr. Meth., A606*. 1 (2009)
 - [2] Horioka,K, Sasaki,T, Takayama, Hasegawa, J, *Journal of Plasma Fusion Research, Vol.86*. 269-281 (2010)
 - [3] T.Sasaki, Y.Yano, M.Nakajima, T.Kawamura, K.Horioka, *Laser and Particle Beams*. Vol.24, 371 (2006)
 - [4] T.Sasaki, M.Nakajima, T.Kawamura, K.Horioka, *Phys. Plasmas*. Vol.17, 084501, (2010)
 - [5] A.W.Desilva, and J.D.Kasouros, *Phys. Rev. E-49*. 4448 (1994)
 - [6] A.W.Desilva and J.D.Kasouros, *Phys. Rev. E57* . 5945 (1998)
 - [7] T.Hosoi, M.Nakajima, T.Kawamura, K.Horioka, *NIFS-Proceedings* . to be appear (2011)
 - [8] Y.T.Lee, R.More, *Phys. Fluids* . Vol.27, 1273 (1984)
 - [9] M.P.Desjarlais, *Contrib. Plasma Physics* . Vol.41, 267 (2001)
 - [10] S.Kuhlbrodt and Redmer, *Phys. Rev.* . E62, 7191 (2000)

Pulsed Power Generator Using Solid-State LTD Modules

Weihua Jiang and Akira Tokuchi

Extreme Energy-Density Research Institute, Nagaoka University of Technology, Nagaoka, Japan

ABSTRACT

Linear transformer driver (LTD) modules using power MOSFETs as switches have been developed and tested for applications to repetitive, compact pulsed power sources. It is based on the same principle as large-scale LTDs being developed abroad for fusion and high energy-density physics purposes, while having advantages in high repetition rate and turning-off capability. It is expected to become a new approach leading to innovative compact pulsed power generators.

Keywords

Pulsed power, power electronics, high voltage, LTD, MOSFET

1. Introduction

Linear transformer driver (LTD) technology is being developed for large-scale pulsed power facilities aiming at nuclear fusion and high energy-density physics applications.¹⁻³⁾ In the LTD scheme, the pulsed power is generated by a large number of synchronized basic circuits, each consists of a capacitor (or capacitors) and a switch. The required output power and output impedance of a system is obtained by connecting these basic circuits in parallel (for the current) and by adding their output inductively (for the voltage).

The important advantage of the LTD concept over traditional pulsed power generation schemes are twofold, one the stress breakup and other is modularity. It is noted that these features are also very attractive in compact pulsed power source development and application. For this reason,

solid-state LTD technology is being developed for industrial applications.⁴⁾

2. Experimental Setup

Figure 1 shows the LTD module using MOSFETs as switches. It has 35 basic circuits each of which consists of a capacitor, a MOSFET, and driver IC. These basic circuits are connected in parallel. There is an optical module which converts the optical control signal to electrical signal and sends it to the driver ICs. The major circuit elements are shown in Table 1.

The equivalent circuit is shown in Fig. 2. The capacitor is charged to a certain voltage beforehand. When the MOSFET is turned on, the capacitor discharges to the load. The magnetic core prevents significant current leakage through the case. The output voltage can be adjusted by either the charging

Table 1 Major circuit elements

Part Name	Manufacturer	Model	Specifications
Capacitor	Murata	GRM55DR73A	1 kV, 100 nF
MOSFET	STMicroelectronics	STB6NK90	900 V, 5.8 A (DC)
Driver IC	Microchip	MCP1407	6 A
Optical Module	Toshiba	TODX283	DC ~ 50 Mb/s

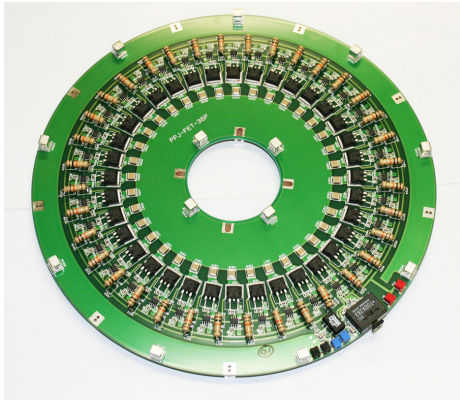


Fig. 1 Solid-state LTD module using MOSFETs.

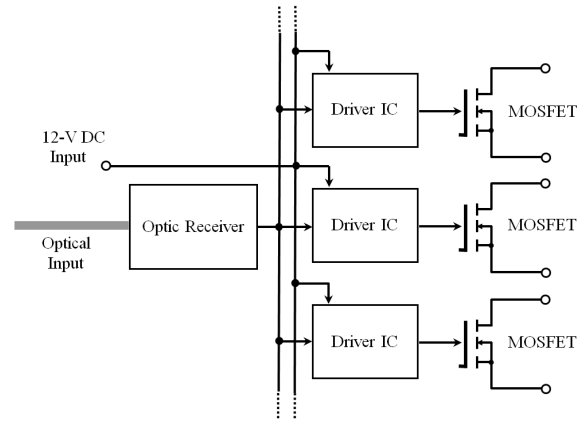


Fig. 3 Illustrated diagram of the gate circuit.

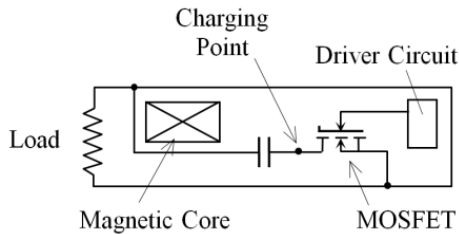


Fig. 2 Equivalent circuit of each LTD unit.

voltage or the number of same modules connected in series, while the output current can be adjusted by changing the switching devices or the number of units that are connected in parallel. In the module shown in Fig. 1, there are totally 35 circuit units.

Figure 3 illustrates the circuit for MOSFET gate control. The original control signal delivered to the module by a fiber is collected by an optic receiver (Toshiba TODX283). The signal is then sent to the inputs of all driver ICs through a common bus. Each driver IC amplifies this signal and send it to the gate of a MOSFET through a resistor of 1Ω . Another wire is used to deliver the 12-V DC power supply to the driver ICs. The charging voltage of the capacitors is applied on the drain electrode of each MOSFET, through a 1-k Ω resistor. The typical waveforms obtained at different locations are shown in Fig. 4, where the capacitor charging voltage is 500V.

The core is made by Sichuan Liyuan Electronics Co., Ltd (China). It has dimensions of outer

diameter 13 cm, inner diameter 8.6 cm, and height 0.5 cm. It is fabricated from Metglass, although its detailed specifications are yet to be obtained. An external DC current source of 2.0 A has been used for magnetic flux restoration through a wire winding of 3 turns around the core.

3. Test Results

In the test results in shown Fig. 4, the original control signal has a pulsed width of 100 ns. After

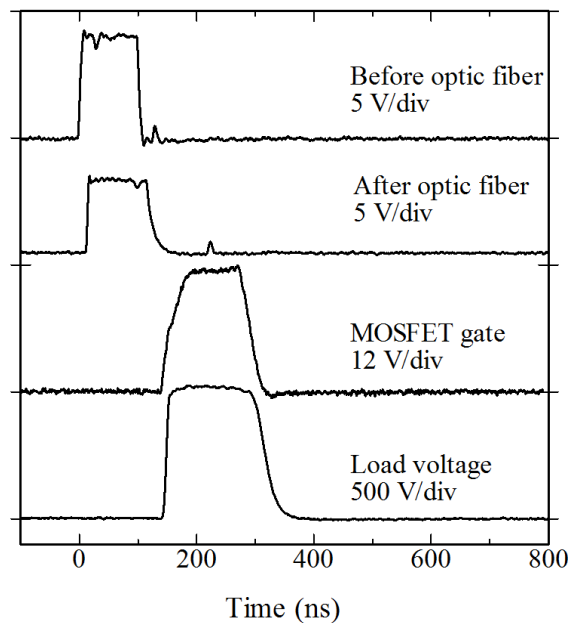


Fig. 4 Typical waveforms (from above) of original control signal, input signal to driver IC, MOSFET gate, and output voltage to a resistive load of 8.25 Ω .

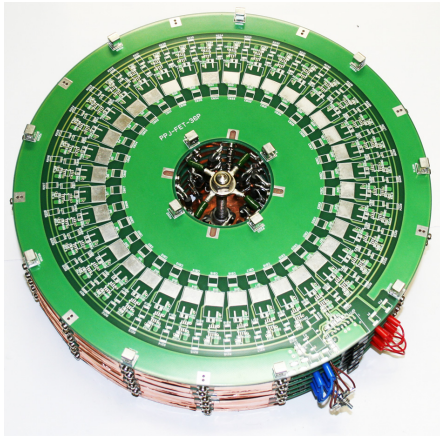


Fig. 5 LTD-based pulsed power generator using 5 modules shown in Fig. 1.

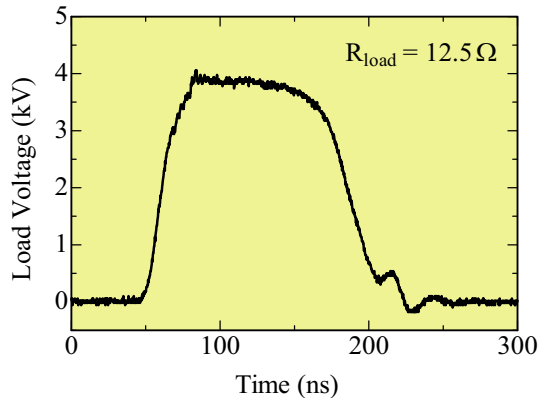


Fig. 6 Output voltage from a 5-module LTD generator to resistive load of 12.5Ω .

the optical transmission, the signal is delayed for only a few nanoseconds and the pulse width is about the same. However, a ~ 100 ns delay is caused by the driver IC which also causes a slight increase in pulse length. The output waveform clearly followed that of the driver IC.

Figure 5 shows the 5-module LTD assemble. It has been tested with charging voltage of 800 V. The output voltage form obtained on a resistive load of 12.5Ω is shown in Fig. 6. The peak voltage reaches nearly 4 kV, with a rise-time of ~ 20 ns and a

fall-time of ~ 40 ns, and a pulse width (FWHM) of ~ 120 ns. The peak output current is calculated to be ~ 320 A giving a peak output power of ~ 1.3 MW. The repetition rate for this testing operation was 1 kHz (continuous).

4. Conclusions

A 5-module LTD assembly has been developed and tested, in order to demonstrate the effectiveness of LTD concept in pulsed power generation. Output of 4 kV with pulsed length of ~ 120 ns has been obtained at repetition rate of 1 kHz.

References

- [1] B. M. Koval'chuk, V. A. Vizir', A. A. Kim, E. V. Kumpyak, S. V. Loginov, A. N. Bastrikov, V. V. Chervyakov, N. V. Tsoi, P. Monjaux, and D. Kh'yui, "Fast Primary Storage Device Utilizing A Linear Pulse Transformer", *Russian Physics Journal*, vol. 40, no. 12, pp. 1142-1153, 1997.
- [2] M. G. Mazarakis, W. E. Fowler, A. A. Kim, V. A. Sinebryukhov, S. T. Rogowski, R. A. Sharpe, D. H. McDaniel, C. L. Olson, J. L. Porter, K. W. Struve, W. A. Stygar, and J. R. Woodworth, "High Current, 0.5-MA, Fast, 100-ns, Linear Transformer Driver Experiments", *Physical Review Special Topics – Accelerators and Beams*, vol. 12, 050401-1~17, 2009.
- [3] W. A. Stygar, M. E. Cuneo, D. I. Headley, H. C. Ives, R. J. Leeper, M. G. Mazarakis, C. L. Olson, J. L. Porter, T. C. Wagoner, and J. R. Woodworth, "Architecture of Petawatt-Class Z-Pinch Accelerators", *Physical Review Special Topics – Accelerators and Beams*, vol. 10, 030401-1~24, 2007.
- [4] W. Jiang: "Solid-State LTD Module Using Power MOSFETs", *IEEE Transactions on Plasma Science*, vol. 38, no. 10, 2730-2733, 2010.

DEVELOPMENT OF MOS-FET BASED MARX GENERATOR WITH SELF-PROVED GATE POWER

A. Tokuchi^{1,2,3}, W. Jiang², K. Takayama³, T. Arai³, T. Kawakubo³ and T. Adachi³

¹*Pulsed Power Japan Laboratory Ltd., Kusatsu, Shiga, 525-0027, Japan*

²*Nagaoka University of Technology, Nagaoka, Niigata, 525-0027, Japan*

³*High Energy Accelerator Research Organization (KEK), Tsukuba, Ibaraki 305-0801, Japan*

ABSTRACT

New MOS-FET based Marx generator is described. An electric gate power for the MOS-FET is provided from the Marx main circuit itself. Four-stage Marx generator generates -12kV of the output voltage. The Marx Generator is successfully used to drive an Einzel lens chopper to generate a short pulsed ion beam for a KEK digital accelerator.

1. Introduction

For many years, A Marx circuit was used to generate a high voltage pulse. Figure 1 shows a conventional Marx circuit. All capacitors (C1~CN) are charged in parallel through charging resistors up to a voltage of Vc. After finishing the charging, all spark gap switches are closed the circuit by an external trigger pulse, then all capacitors are connected in series and a high voltage pulse of $N \times V_c$ is generated. Here, N is a number of the capacitors. There are some demerits in the conventional Marx circuit as follows.

- Long charging time because the charging current flows through the charging resistors.
- Low efficiency because of the same reason mentioned above.
- Low repetition rate because of the same reason.
- Few output voltage appearance in charging period because the charging current flows through the charging resistors and a load.
- Turn-off is impossible because of using the spark gap switches.
- Short life time of the spark gap switches.

In order to solve these problems, some new Marx circuits are proposed. These new improved circuits use semiconductor switches such as MOS-FETs or IGBTs. Two types of the improved circuits are introduced here.

Figure 2 shows an improved Marx circuit that we called TYPE-1. In the TYPE-1 circuit, all charging resistors are replaced to diodes and all spark gap switches are replaced to semiconductor switches. In fig. 2, MOS-FETs are used as semiconductor

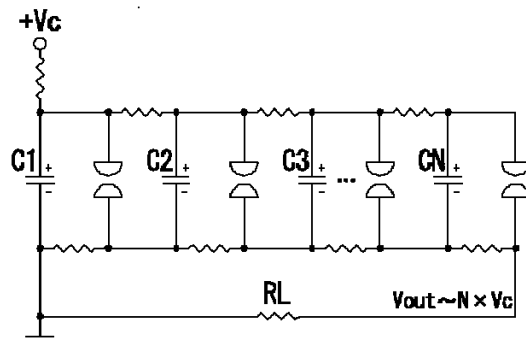


Figure 1: Conventional Marx circuit.

switches. In The TYPE-1 circuit, some demerits of conventional Marx circuit are improved as follows.

- Relatively short charging time because the charging current flows through the diodes instead of the charging resistors.
- Relatively high efficiency because of the same reason mentioned above.
- Relatively high repetition rate because of the same reason.
- Turn-off is possible because of using the semiconductor switches instead of the spark gap switches.
- Long life time of the switches.

But some demerits and new demerit are still remained in the TYPE-1 circuit as follows.

- Few output voltage appearance in charging period because the charging current flows through a load.
- About the charging time, the efficiency and the repetition rate, they are not optimal because

of above-mentioned reason.

- One additional gate circuit is required in each Marx stage to drive the semiconductor switch.

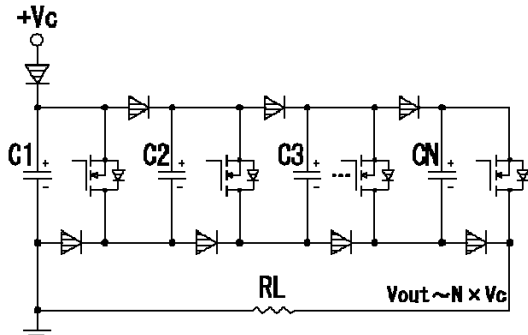


Figure 2: Improved Marx circuit (TYPE-1).

To the next, fig. 3 shows an improved Marx circuit that we called TYPE-2. In the TYPE-2 circuit, a half of the charging diodes are replaced to another semiconductor switches. In fig. 3, MOS-FETs are also used as the second semiconductor switches. In The TYPE-2 circuit, all demerits of conventional Marx circuit are further improved as follows.

- Very short charging time because of no charging resistor in charging circuit.
- Very high efficiency because of the same reason mentioned above.
- Very high repetition rate because of the same reason.
- Turn-off is possible because of using the semiconductor switches.
- Long life time of the switches.
- No output voltage appearance in charging period because the charging current dose not flow a load.

But new demerit of the TYPE-2 circuit is described as follows.

- Two additional gate circuits are required in each Marx stage to drive the semiconductor switch.

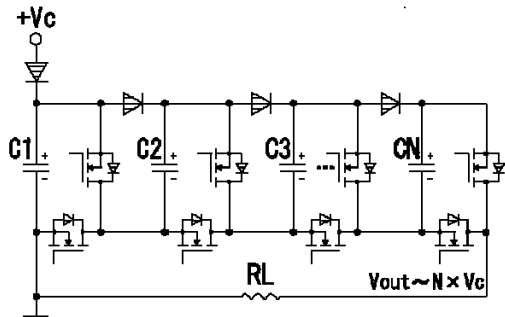


Figure 3: Improved Marx circuit (TYPE-2).

We developed TYPE-1 Marx circuit in order to drive an Einzel lens chopper used for a short pulsed ion beam generation to inject into a digital accelerator

at KEK.

2. A design of a Marx board

Table 1 shows target specifications of the developed Marx board. Four Marx-boards were used to generate an output pulsed voltage of 12kV.

Table 1 Specifications of the Marx board.

Switching device	MOS-FET IXTF1N400(IXYS) Rationg:4kV,1A,3Ap
Circuit configuration	Improved Marx circuit (TYPE-1) Involving a dummy load
Charging voltage	3kV
Pulse output current	9Ap
Gate power supply	Self-providing from main circuit
Rise time	Less than 30ns

In case of the Marx circuit using semiconductor switch, an important technical problem is how to provide a gate power to drive the semiconductor switches. Each Marx board is triggered by optical fiber signal, because a voltage potential of the each Marx board is different each other. An electric power supply is required to transmit from optical trigger signal to electric gate signal in each Marx board. There are following three methods to provide the electric gate power to the Marx board.

- (1) Using DC-DC converter
- (2) Using isolation transformer and AC-DC converter
- (3) Self-providing from main circuit

In case of (1), an isolation voltage of the commercial DC-DC converter is less than about 6kV. Therefore a high voltage pulse generator cannot use this method. In case of (2), a stray capacitance of the isolation transformer may cause a serious oscillation of the output pulsed voltage, and it is usually difficult to find out optimal devices in commercial. In case of (3), a technical problem is how to reduce a current from main circuit to the gate circuit.

In this development we chose a method of (3). Figure 4 shows a circuit diagram to provide a electric gate power from a main circuit of the Marx circuit. A

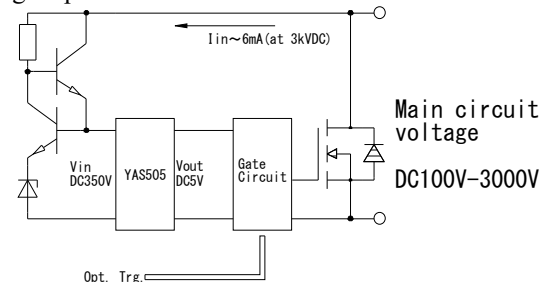


Figure 4: Circuit diagram to provide gate power from main circuit.

maximum charging voltage of the main circuit of the Marx board is 3kV. If we can use a DC-DC converter from DC3kV as a primary voltage to DC5V as a secondary voltage, that is quite ideal. Regrettably there is no such a convenient device. The second best plan is using a DC-DC converter having highest primary voltage. Then we chose DC-DC converter YAS505 (cosel co.) that had wide range of primary voltage from DC110V to DC370V. An efficiency of that is 65%. DC350V of a primary voltage was made by using a voltage regulation of a bipolar transistor circuit, then a DC5V of a secondary voltage was obtained by using YAS505. A current from the main circuit to gate circuit was less than 6mA. This value is relatively low and almost fixed during from DC100V to DC3000V of the main charging voltage.

Figure 5 shows a circuit diagram (upper) and a photograph (lower) of a developed Marx board. The Marx board consists of a main capacitor, MOS-FETs,

a gate power circuits, an optical trigger circuit, Marx diodes and dummy loads. The main capacitors are 10 parallels of 3150V, 0.047uF. The MOS-FETs are 3 parallels of IXTF1N400(4kV,1A). The gate power circuit provides a voltage of DC5V for the optical trigger circuit. The Marx diodes connect the Marx board to next Marx board. The dummy load keeps a current of the MOS-FETs constant during the output pulse and reduces a fall time of the output pulse.

3. An experimental results of a Marx board

Figure 6 shows a waveform of a gate voltage for a MOS-FET of the Marx board and an external trigger pulse. The external trigger pulse is transmitted to an optical trigger signal. The optical trigger signal is re-transmitted to electric voltage trigger pulse on the Marx board. From Fig. 6, a gate voltage of 16V was obtained and a pulse width of it was about 4 us.

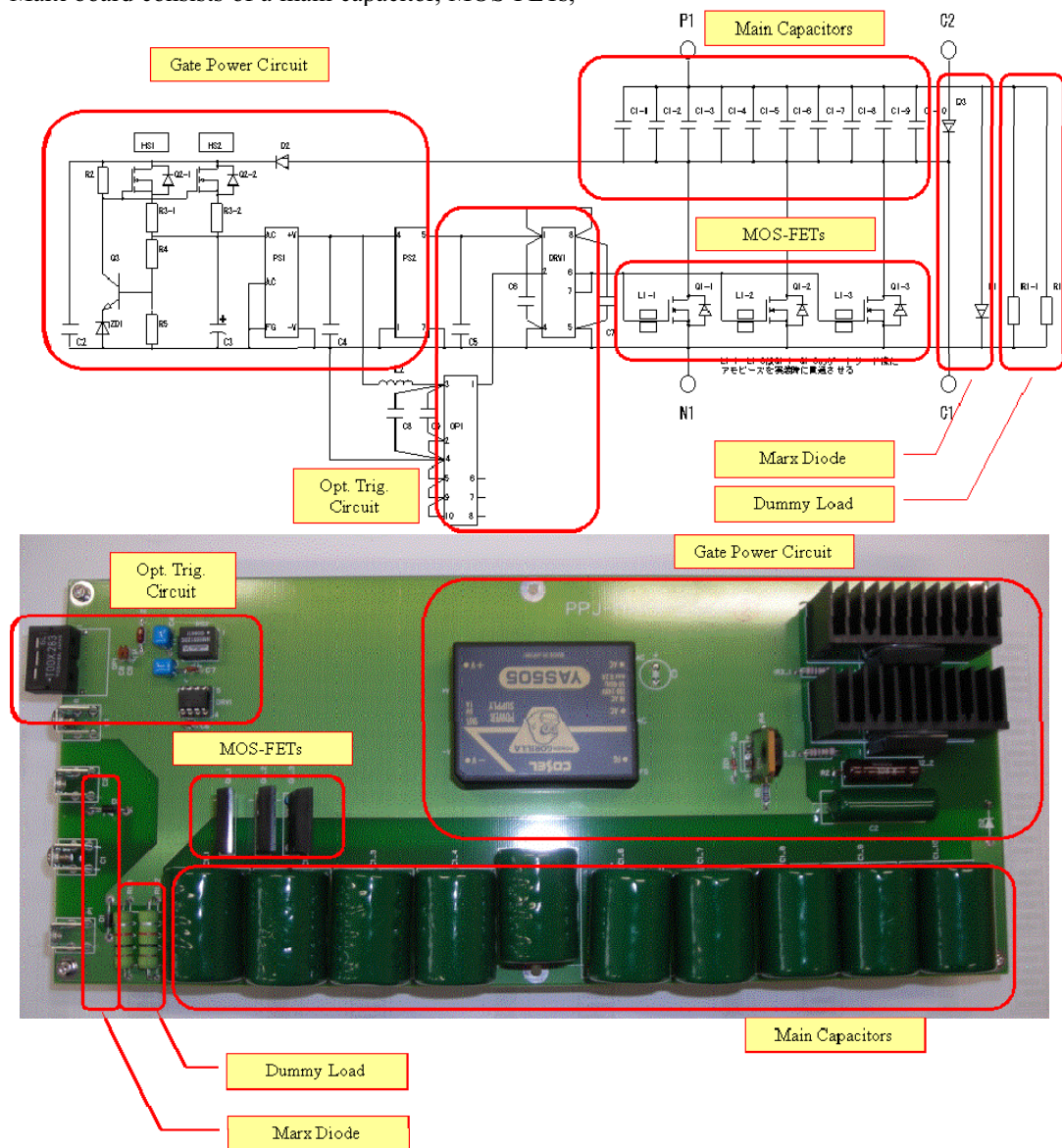


Figure 5: A circuit diagram (upper) and a photograph (lower) of the Marx board.

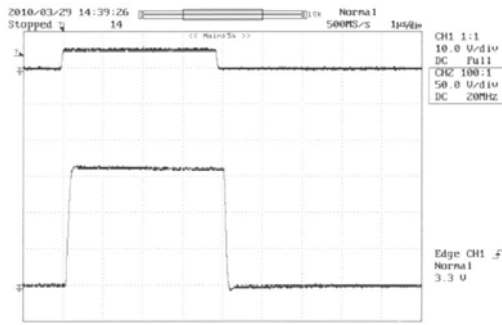


Figure 6: A waveform of a gate voltage for a MOS-FET of Marx board (lower 5V/div) and an external trigger pulse (upper 10V/div). 1 us/div.

Figure 7 shows a waveform of the output voltage of the Marx Board. In this test, a pulse width of an external trigger was changed to 5 us. When a charging voltage was 3kV and a dummy load was 500 ohm, a peak output voltage of 2.7kV was obtained.

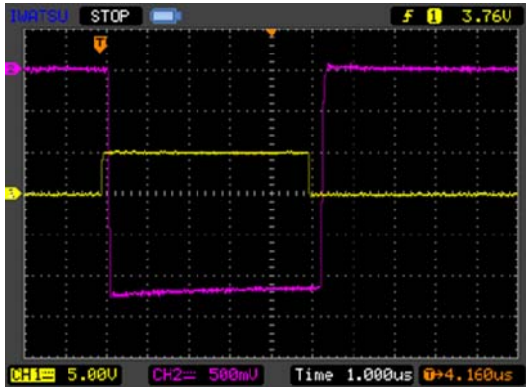


Figure 7: A waveform of an output voltage of Marx board (CH2 violet 500V/div) and an external trigger pulse (CH1 yellow 5V/div). 1 us/div.

In the next, we examined four-stage Marx generator by using four Marx boards. Figure 8 shows an experimental setup. Four Marx boards are stacked vertically and each Marx board is triggered by using an optical fiber signal.

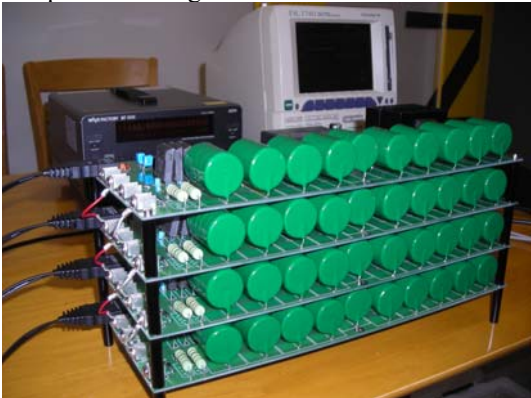


Figure 8: An experimental setup of the four-stage Marx generator.

Figure 9(a) shows a waveform of an output voltage of four-stage Marx generator. When a charging voltage was 2.5kV and a dummy load was 2 kohm, a peak output voltage was 10kV and a pulse width was about 5 us. It was examined that a voltage was amplified four times by Marx circuit. Figure 9(b) and 9(c) show the rise time and fall time of the output pulse each. A rise time was 30ns and fall time was 120ns. The fall time is determined by stray capacitance of the output and the resistance of the dummy load. These values were suitable for an Einzel lens chopper of the digital accelerator.

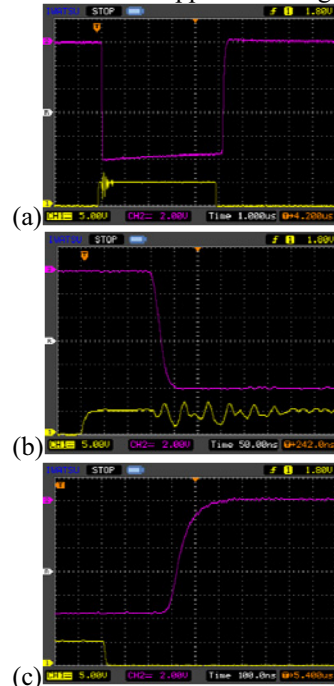


Figure 9: (a) shows a waveform of an output voltage of four-stage Marx generator (CH2 violet 2kV/div) and an external trigger pulse (CH1 yellow 5V/div). (b) and (c) show the output voltage at rise-up and at fall-down each.

4. An Einzel lens chopper experiment

We examined that the developed four-stage Marx generator drive an Einzel lens chopper of digital accelerator at KEK. The Einzel lens chopper is used to chop a long (5ms) ion beam that extracted from an electron cyclotron resonance ion source (ECRIS) to short pulse (5microsec). Figure 10 shows a schematic of the Einzel lens chopper. The middle electrode voltage of the Einzel lens is sustained at V_0 . Ions stop at the position of the middle electrode and are unable to propagate downstream. When a rectangular-shape negative voltage pulse ΔV ($V_0 + \Delta V < V_0$) is provided on the middle electrode in a short time duration, τ . As a kind of barrier voltage stopping ions in the longitudinal direction is reduced, ions can propagate beyond the Einzel lens region for τ . This is an essential mechanism of the Einzel lens chopper.

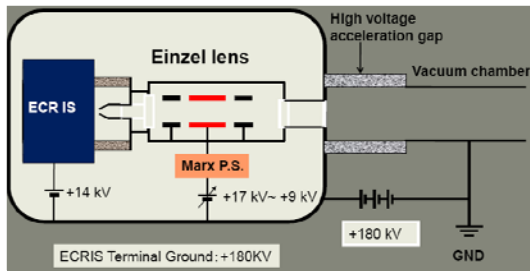


Figure 10: ECRIS with the extraction system and Einzel lens in the high voltage terminal.

Figure 11 show an experimental result of Einzel lens chopper. In the preliminary experiment, a pulse voltage of -8 kV and 5 μ sec, which was generated by the Marx generator, was superimposed on the DC bias voltage of 14 kV at the middle electrode of the Einzel lens. The ion current of He²⁺ was monitored by a Faraday cap. The ion current pulse profile and the electrode voltage profile are shown in Fig. 7. In the time duration of the negative voltage pulse, the ion flow arrived at the Faraday cap. A reason of a delay time between the pulse voltage and the ion current pulse is a response of the Faraday cap. It was proved that the Einzel lens chopper driven by the MOS-FET based Marx generator successfully made the short ion beam from an ion beam extracted from slow ion source.

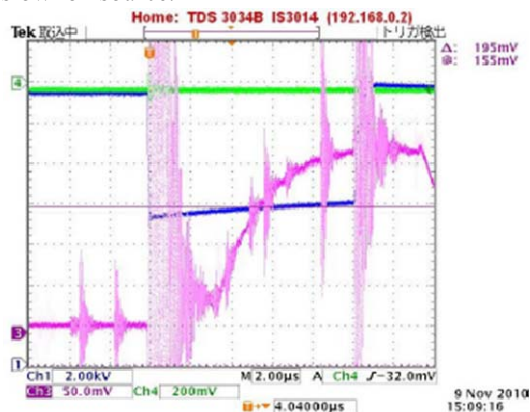


Figure 11: Experimental result of the Einzel lens chopper driven by the Marx generator. Negative voltage pulse (blue) and ion beam profile monitored by the Faraday cup (red).

5. summary

A MOS-FET based Marx generator (TYPE-1) was developed. A gate power was directly provided from the main circuit of Marx generator. A current flow from the main circuit to the gate circuit was about 6mA that was practically low. When the charging voltage was 3kV, an peak output voltage of 12kV was obtained by using Four-stage Marx generator. A rise time of the output voltage was 30ns. The MOS-FET based Marx generator was used to drive an Einzel lens chopper of a digital accelerator and successfully chopped to the short ion beam.

In near future, we will develop the next generation Marx generator (TYPE-2) and new gate power circuit using a combination of a high frequency inverter, a high voltage isolation transformer and a AC/DC converter.

A Marx generator using semiconductor switches has great advantages such as high repetition rate, high efficiency, small size, high reliability, easy control of an output voltage waveform and low cost. It is expected that the semiconductor Marx generator will be utilized for many new industrial applications.

References

- 1) T. Iwashita, T. Adachi, K. Takayama, T. Arai, Y. Arakida, M. Hashimoto, E. Kadokura, M. Kawai, T. Kawakubo, Tomio Kubo, K. Koyama, H.Nakanishi, K. Okazaki, K. Okamura, H. Someya, A. Takagi, A. Tokuchi, K. W. Leo, and M. Wake, "KEK Digital Accelerator", to be published in Phys. Rev. ST-AB 14, 071301 (2011).
- 2) Toshikazu Adachi, Teruo Arai, Kwee Wah Leo, Ken Takayama, and Akira Tokuchi, "A Solid-state Marx Generator Driven Einzel Lens Chopper", Rev. of Sci. Inst. 82, 083305 (2011).

Design of Bragg Resonator for Free Electron Maser

Kota Nose, Ken Misawa, Shoko Yanagi, Katsumasa Kato, Taro Kitamura
Naohisa Yamada, Yukihiro Soga, Keiichi Kamada,
Mitsuhiro Yoshida* and Naum S. Ginzburg**

*Graduate School of Science and Technology, Kanazawa University,
Kanazawa, Ishikawa, 920-1192, Japan*

**High Energy Accelerator Research Organization, KEK
1-1 Oho, Tsukuba, Ibaraki 305-0801 Japan*

***Institute of Applied Physics, Russian Academy of Sciences,
Nizhny Novgorod, 603600, Russia*

ABSTRACT

Two Bragg resonators are designed to develop the frequency selectivity for a free electron maser with frequency of 40 GHz using a helical wiggler coil and an intense relativistic electron beam. One is a normal Bragg resonator utilizing two traditional Bragg reflectors and another is a hybrid Bragg resonator with an advanced and a traditional Bragg reflectors. In the cold test, the frequency selectivity of the hybrid Bragg resonator is appeared to be 0.05 GHz, while that of the normal one is 0.5 GHz.

Keywords

electron beam, intense microwave source, Bragg resonator, FEM, IREB

1. Introduction

Microwave sources with frequency between 0.1 to several tera-hertz (THz) are developed intensively in this decade. THz sources using laser and large accelerator explore every new possibility of application. Among electron tubes, gyrotrons have reached the stage of practical use for thermonuclear fusion with output power of 1 MW and frequency of 200 GHz. An electron tube with a pulsed mildly relativistic electron beam (REB) is expected to realize the intense THz source with output power of over tens of MW. Free electron maser (FEM) is one the candidates of THz source using REB. However, because of its strong self electric field, one of the problems for the FEM using REB is the wide frequency spectrum. Usually, a normal Bragg resonator is utilized to develop the frequency

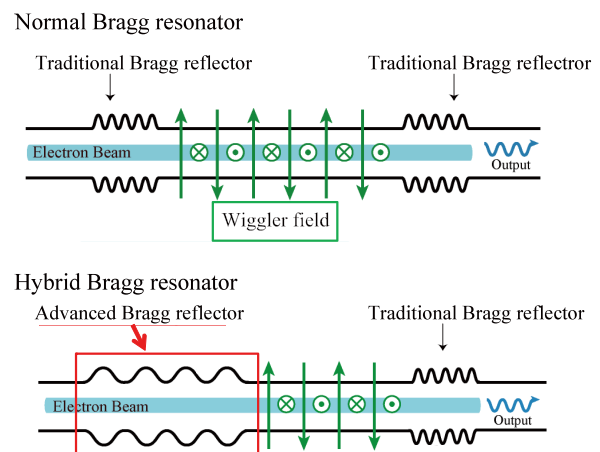


Fig. 1. Schematics of the Normal Bragg Resonator (upper) and the hybrid Bragg resonator.(lower). An IREB is injected from left side.

selectivity. Traditional Bragg reflectors work as mirrors in the optical distributed feedback laser (Fig.1)[1-5]. As the frequency increases, the traditional Bragg reflector loses the selective features over transverse indexes. An advanced Bragg reflector was proposed by Ginzburg[6]. It utilizes the interaction between a propagating wave and a quasi-cutoff mode to provide a higher selectivity over the transverse index than a normal Bragg reflector. Structural difference between the traditional and the advanced reflectors is mainly on the periodic length of the corrugation. While the period of corrugation of a traditional Bragg reflector is a half of the guide wavelength, that of an advanced Bragg reflector is nearly equal to it. The words, “reflector” and “resonator”, are indicated in Fig. 1. In the hybrid Bragg resonator, an advanced Bragg reflector is used at the entrance side and at the exit side the traditional Bragg one is utilized.

2. Experimental Setup

The experimental setup is roughly shown in Fig. 2. An intense relativistic electron beam (IREB) with energy of around 700keV and current of around 200 A was injected into the drift tube with diameter of 20mm. Axial magnet field (Bg) with strength of up to 1T was applied by two solenoid coils. The IREB was diverged to the wall at the exit of the axial magnetic field. A helical wiggler coil [7] located inside the solenoid coils provided a periodic radial magnetic field (Bh) up to 0.15 T. The location of the Bragg reflectors is also indicated in Fig. 2.

We carried out the FEM experiments. With the normal and hybrid Bragg resonators, the radiation with frequency of 35.5-40 GHz was observed and its output power was changed by the strength of Bh. The FEM radiation with TE₁₁ mode was estimated from the experimental parameters. The advantage of the hybrid Bragg resonator to the normal one was not clear because of the resolution of the spectrometer. And because of the break down of the beam source, no more experimental result of FEM

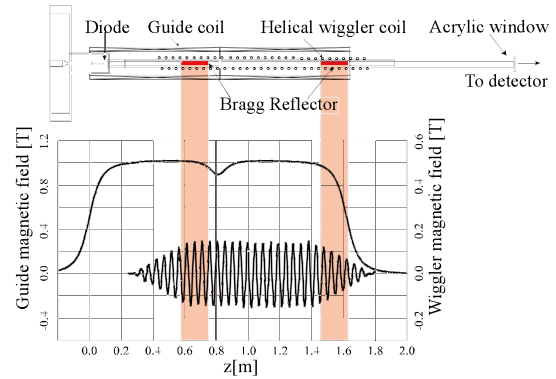


Fig. 2 Experimental setup

has obtained yet.

In parallel with the preparation of new spectrometer with higher frequency resolution, we reexamined the experimental parameters of the helical wiggler coil. We start to redesign the helical wiggler coil to increase the output power of the radiation.

In this paper, the basic design of helical wiggler coil and Bragg resonators is described. Results of the cold test of Bragg resonators are also presented.

3. Single Particle Calculation

The effective length of the helical wiggler field is estimated by the calculation of energy exchange between an electron and the electromagnetic wave. Very simple evaluation by the equation of motion of

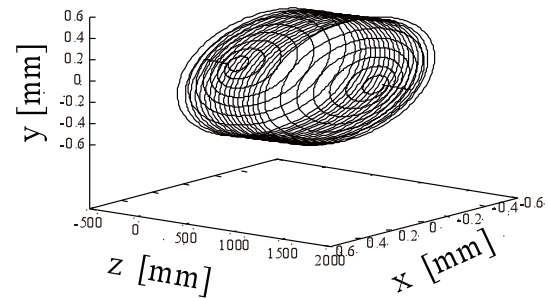


Fig. 3. Single particle orbit in the wiggler magnetic field. An electron was injected at (0,0,0). The axial magnetic field was applied along z-axis.

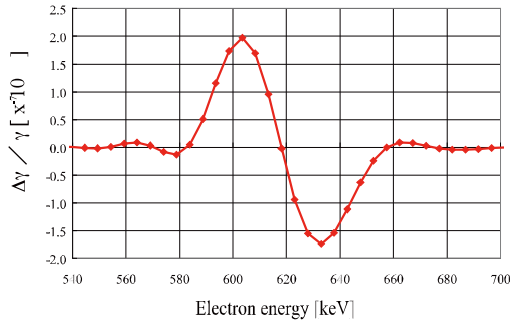


Fig. 4. Energy decrease of electrons propagating with 40 GHz, TE₁₁ electromagnetic wave through drift tube immersed in the wiggler and axial magnetic field.

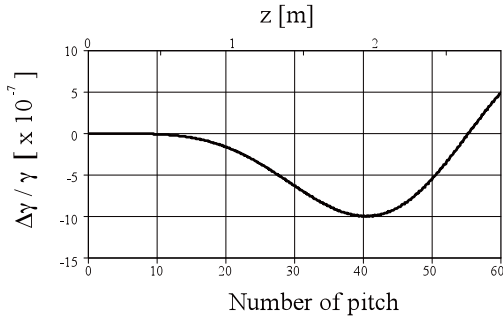


Fig. 5. Energy decrease of electrons vs the wiggler length.

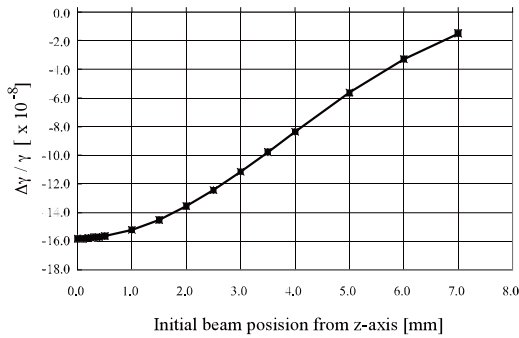


Fig. 6. Energy decrease of electrons vs the initial radial position of electrons.

an electron was employed. An electron was injected into the axial and helical magnetic field with the electromagnetic wave. The typical orbit of an electron without the electromagnetic wave is shown

in Fig. 3. A helical orbit whose period is equal to that of the helical coil is observed. Without the gradual increase of the helical wiggler field, electrons hit the wall.

The increase or decrease of the kinetic energy of an electron travelling with electromagnetic wave through the magnetic fields was evaluated along the axis. The initial phase of the electromagnetic wave at the injection point of an electron was varied from 0 to 2π . The sum of the kinetic energy difference of electrons injected at different initial phase was calculated along the axial length. It was supposed that the decrease of the kinetic energy of electrons was equal to the increase of the energy of the electromagnetic wave. But the latter increase was not reflected to the calculation. Figure 4 show the energy increase/decrease of the beam electrons propagating with the electromagnetic wave with frequency of 40 GHz. The maximum energy decrease is observed at the electron energy of 630 keV. The intersection point of the beam and TE₁₁ mode lines of the dispersion relation is 620 keV, 40 GHz where the phase velocities of the beam and TE₁₁ mode are the same. At this point, the exchange of the energy is zero as shown in Fig.3 as expected. We use the results of the single particle calculation as rough criteria to design the helical wiggler coil and beam radius.

Figure 5 shows the energy decrease of the electrons along the axial length of the helical wiggler coil. It is clear that the energy decrease is saturated at $z=200$ cm i.e. 40 pitches of the wiggler coil.

It is also calculated that the energy decrease of the electrons reduces with the distance from the axis (Fig. 6). This can be used to determine the beam radius.

The energy exchange between the backward wave and electrons was calculated as the energy exchange by the reflected wave from the Bragg reflector at the downstream side was anticipated. The energy of electrons was not changed by the backward wave.

4. Bragg resonators

4.1 Design and cold test of Bragg reflectors

The period of corrugation for a traditional Bragg reflector can be determined by the relation $k_g = k_b/2$, where k_g is the wave number for 40 GHz, TE₁₁ mode of the circular waveguide and k_b is that of the corrugation period. To determine the depth of the corrugation and the length of the traditional reflector, we use the simulation code CST MW studio. Before we utilized the simulation, we check the reliability of the simulation. The reflective coefficient of the traditional Bragg reflector was calculated by use of the Mode-coupling theory [8]. In the calculation, the frequency of 40 GHz (TE₁₁ mode) is expected and TM₁₁ mode is considered to be a candidate of mode conversion. The calculated results showed good agreement with the simulated one as shown in Fig. 7.

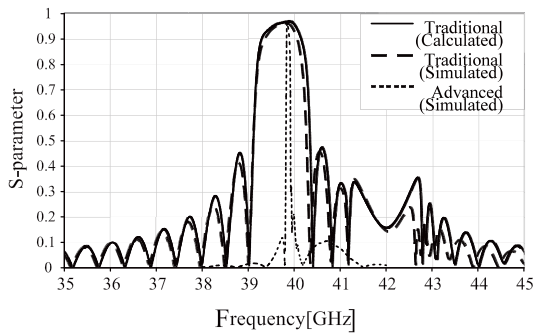


Fig. 7. Calculated results based on the mode coupling theory and simulated results for the traditional Bragg reflector show good agreement. The simulated results of the advanced Bragg reflector is also shown.

The simulated results of reflective coefficient for the depth and the total length of the corrugation for the traditional Bragg reflector are shown in Fig. 8. From these results, the depth and total length are decided to be 0.25 mm and 400 mm, respectively.

We applied the simulated results to set the parameters of an advanced Bragg reflector. The parameters of both Bragg reflectors are summarized on Table 1. The reflective coefficient of the 40 GHz advanced Bragg reflector is also plotted in Fig. 7

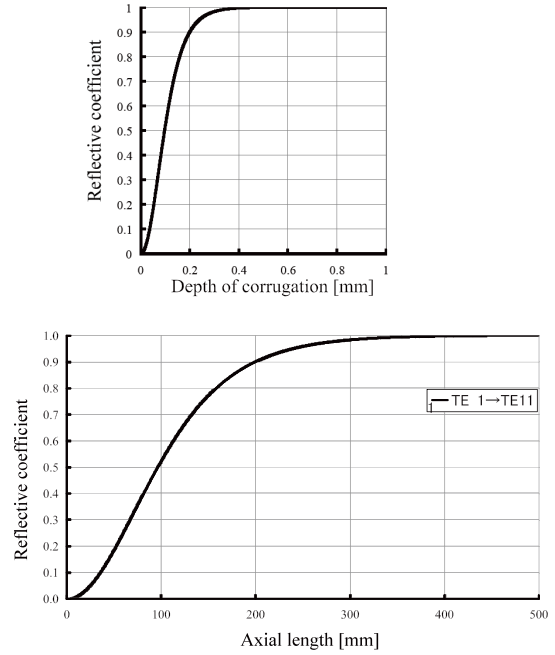


Fig. 8. Simulated results of reflective coefficient vs depth (upper) and length (lower) for the traditional Bragg reflector

along the frequency. The width of the frequency peak of the advanced Bragg reflector is nearly 10 times narrower than the traditional one.

	Traditional	Advanced
Mode	TE ₁₁	TE ₁₁
Frequency [GHz]	39.8	39.8
Frequency Width [GHz]	±0.5	±0.05
Corrugation		
Period [mm]	3.9	7.6
Depth [mm]	0.25	0.1
Length [mm]	400	200

Table 1 Parameters of traditional and advanced Bragg reflectors

Cold tests of the Bragg reflectors were carried out using network analyzer E8354C (Agilent Technology). The microwave passed through the Bragg reflector was detected. The experimental results show good agreements with the simulated results as shown in Fig.9. The width of the reflected frequency of the advanced Bragg reflector is about 10 times narrower than that of the traditional one. This result should contribute to higher frequency selectivity of the hybrid Bragg resonator than that of the normal one.

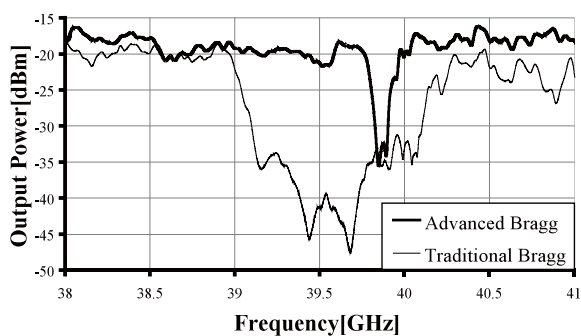


Fig. 9. Transparent characteristics of normal and advanced Bragg reflectors (cold test).

4.2 Cold test of Bragg resonators

Cold tests for normal and hybrid Bragg resonators were carried out with the same network analyzer used for Bragg reflectors. Microwave with frequency around 40 GHz was radiated at the center of the Bragg resonator. And the microwave passed through the traditional Bragg reflector located at the downstream side of both resonators was detected as shown in Fig. 10.

The experimental result of the normal Bragg resonator is shown in Fig. 11. Several peaks were observed within the frequency range in which the microwave passed through the traditional Bragg reflector. The frequencies of each peak are the function of the distance between two Bragg reflectors.

The frequency spectrum passed through the hybrid Bragg resonator is shown in Fig. 12. A single

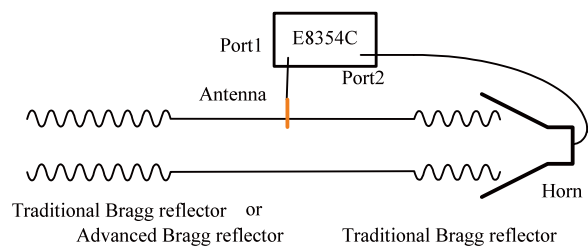


Fig.10. Schematic of the cold test of Bragg resonators.

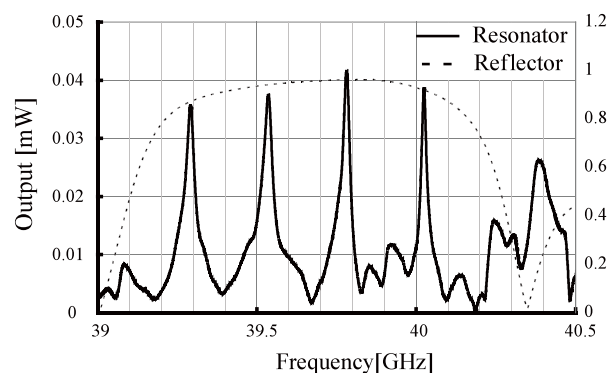


Fig. 11. Frequency spectrum of the normal Bragg resonator.

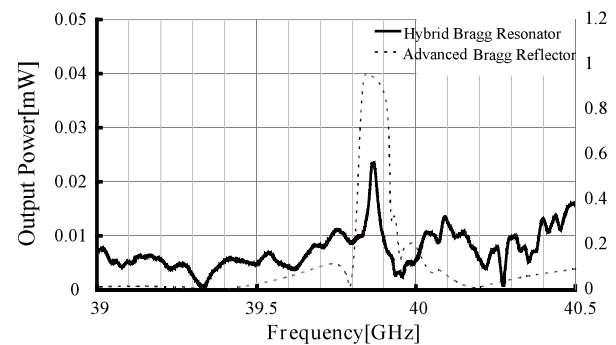


Fig. 12. Frequency spectrum of the hybrid Bragg resonator.

narrow peak is observed at the detected frequency of the advanced Bragg reflector. In comparison with the cold test of the normal Bragg resonator, we can expect the higher frequency selectivity of the hybrid Bragg resonator.

We will carry out the further experiments to increase the output power of the hybrid Bragg

resonator and the appropriate distance between the Bragg reflectors.

4. Conclusions

Criteria of the design of the wiggler coil and beam radius for more intense radiation were obtained by the single particle calculation of the energy exchange between electrons and electromagnetic wave.

The simulated and experimental results of the traditional and the advanced Bragg reflectors show good agreements. We can design new Bragg resonators by the simulation.

From the results of the cold test of both Bragg resonators, we can expect higher frequency selectivity of the hybrid Bragg resonator than the normal one.

References

- [1] A. Kasugai, K. Sakamoto, K. Takahashi, K. Kajiwara and N. Kobayashi: "Steady-state operation of 170 GHz–1 MW gyrotron for ITER", Nuclear Fusion, Vol. 48, Issue 5, pp. 054009 (2008).
- [2] G. G. Denisov, M. G. Reznikov: "Corrugated cylindrical resonators for short-wavelength relativistic microwave oscillators ", Radiophysics and Quantum Electronics, vol. 25, No 5, pp. 407-413, (1982).
- [3] R. B. Mccowan: "Design of a waveguide resonator with rippled wall reflectors for a 100 GHz CARM oscillator", Int. J. Electronics, Vol.65, No.3, pp. 463-475, (1988).
- [4] I. Boscolo: "A tunable Bragg cavity for an efficient millimeter FEL driven by electrostatic accelerators", Appl. Phys. B57, pp. 217-225, (1993)
- [5] T. S. Chu, F. V. Hartemann, B. G. Danly, and R. J. Temkin: "Single-Mode Operation of a Bragg Free-Electron Maser Oscillator", Phys. Rev. Lett., 72, 2391-2394 (1994)
- [6] N. S. Ginzburg, A. M. Malkin, N. Yu. Peskov, A. S. Sergeev, A. K. Kaminsky, S. N. Sedykh, E. A. Perelshtein, A. P. Sergeev, A. V. Elzhov: "Improving selectivity of free electron maser with 1D Bragg resonator using coupling of propagating and trapped waves", Phys. Rev. ST-AB, vol. 8, 040705, (2005).
- [7] K. T. McDonald: "The Helical Wiggler", Joseph Henry Laboratory, Princeton University, Princeton, NJ 08544, Oct.12. (1986).
- [8] N. S. Ginzburg, A. M. Malkin, N. Yu. Peskov, A. S. Sergeev, V. Yu. Zaslavsky, K. Kamada, R. Ando: "Free electron laser with terahertz band Bragg reflectors", Phys. Rev. ST-AB, vol. 12, 060702, (2009).
- [9] N. S. Ginzburg, A. M. Malkin, N. Yu. Peskov, A. S. Sergeev, V. Yu. Zaslavsky, K. Kamada, Y. Soga: "Tunable terahertz band planar Bragg reflectors", Appl. Phys. Lett. 95, 043504, (2009).
- [10] N. Ginzburg, A. Malkin, N. Peskov, A. S. Sergeev, V. Zaslavsky, I. Zotova, K. Kamada, Y. Soga: "Terahertz band FEL with advanced Bragg Reflectors", Proc. of FEL conf., Liverpool, UK., pp. 424-427, (2009).

DEVELOPMENT OF 100 GHz INTERDIGITAL BACKWARD-WAVE OSCILLATOR

Masashi Kato, Yukihiro Soga, Tetsuya Mimura, Yasutada Kato, Keiichi Kamada,
and Mitsuhiro Yoshida*

*Graduate School of Natural Science and Technology, Kanazawa University, Kakuma-machi,
Kanazawa, Ishikawa, 920-1192, Japan*

**High Energy Accelerator Research Organization, 1-1 Oho, Tsukuba, Ibaraki 305-0801 Japan*

ABSTRACT

Simulation studies were carried out on newly designed compact interdigital backward-wave oscillator (BWO) at a frequency of 100 GHz with output power of 700 mW was observed at beam current 100 mA. We designed and constructed the thermionic electron gun that produces an electron-beam that has sufficient energy and emission current for the radiation. A proof of principle experiment of the high power BWO with THz band had started.

Keywords

Backward Wave Oscillator, Electron beam, Electron Gun, THz wave

1. Introduction

Compact electron tubes at terahertz (THz) frequencies offer enormous applications for medical diagnostic, broad-band communication and spectroscopy. Backward-wave oscillator (BWO) is a typical candidate of compact terahertz sources[1].

The output power of a terahertz band BWO, however, has been limited to 100 mW at most at 100 GHz. This is because the structure of a terahertz BWO is comparable in size to the wavelength of 3 mm and then the interaction region and coupled-interaction impedance between electrons and a slow-wave circuit reduces. The purpose of our study is to increase in the output power up to 1 W of a compact terahertz BWO with newly designed electron beam distributions and slow wave structures (SWS).

2. Interdigital slow-wave circuit

Figure 1 shows the structure of an interdigital circuit. The fundamental wave of the interdigital circuit in the dispersion relation is backward whereas

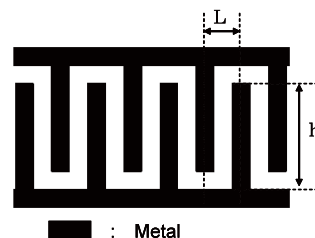


Fig.1. Interdigital structure

that of a general SWS is forward wave. If fundamental is backward wave, the strong interaction between the electromagnetic (EM) wave and electron beam will occur and the phase velocity of the EM wave becomes fast. It is advantageous for the output power improvement of BWO because the energy of the electron beam can be increased compared with other slow-wave circuits. The pattern of an interdigital circuit was produced on the dielectric substrate and uses it as a slow-wave circuit. In the experiment the electron beam is injected along the substrate, and it is interacted with the slow-wave circuit.

When the parameters of SWS and the electron beam

are determined, it is needed to estimate the radiation frequency from the intersection of the dispersion curve of the EM wave propagating on SWS and the beam mode. In this analysis the dispersion of the interdigital type slow-wave circuit is considered. Because the EM wave propagates between the combs of metal, the relation between the phase ϕ_{BW} and the frequency ω can be written as

$$\phi_{BW} = (h + L)\omega / v_g - \pi. \quad (1)$$

Here h is the height of the comb teeth, L is the length of one pitch (Fig.1) and v_g is a group velocity of the EM wave and then

$$v_g = c / \sqrt{\epsilon_{eff}}. \quad (2)$$

Here ϵ_{eff} is an effective permittivity of the dielectric substrate. Because the mode of EM wave on the SWS is almost the same as the quasi-TEM mode that propagates on the coplanar stripline, ϵ_{eff} may be written as follows

$$\epsilon_{eff} = 1 + \frac{\epsilon_r - 1}{2} \frac{K(k')K(k_1)}{K(k)K(k_1')}, \quad (3)$$

where K is complete elliptic integral of the first kind and

$$k = a/b, \quad k_1 = \frac{\sinh(\pi a / 2d)}{\sinh(\pi b / 2d)}, \quad a = S/2, \quad b = S/2 + W$$

$$k' = \sqrt{1 - k^2},$$

where S is the width of metal, W is the distance between the gap and d is the thickness of dielectric.

The interdigital slow-wave circuit is designed by using the equations (1) - (3) that can radiate the EM wave at a frequency 100GHz for the electron beam with the energy of 10keV. The dielectric substrate is made from 1 mm thickness Teflon (relative permittivity is equal to 2). Table 1 shows the designed parameters of SWS.

Table.1 Parameters of SWS

Thickness of metal	20 μm
Thickness of substrate	1 mm
L	150 μm
h	440 μm
Number of pitch	200

Figure 2 shows the dispersion relation of the

slow-wave circuit in the determined parameters. The radiation is expected at the frequency on the intersection with the beam mode in the dispersion. However, the dispersion lines will actually bend where the wave number is 0 and π because the impedance change for the frequency is not considered in Fig.2.

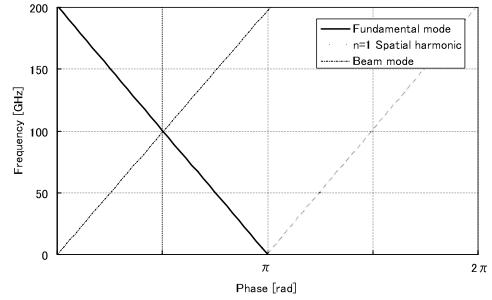


Fig.2. Dispersion of interdigital circuit

3. Simulation on EM wave radiation

We calculated an EM wave radiation from the designed interdigital slow-wave circuit using CST PARTICLE STUDIO in CST STUDIO SUITE. This is one of the most commonly used software in the field of accelerator or microwave tubes [2,3].

Figure 3 shows the position of the slow-wave circuit and the electron beam. The cylindrical electron beam is injected along the surface of the slow-wave circuit on the substrate. The diameter of the cathode is 1 mm, and the distance between the SWS and the bottom of the electron beam is 0.1 mm.

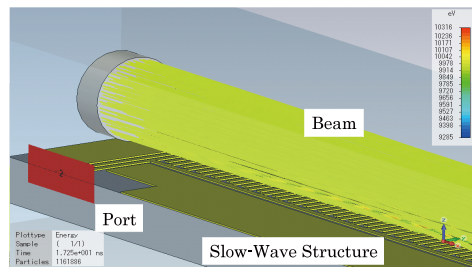


Fig.3. Schematic view of slow-wave circuit and electron beam

The metal of SWS is made of copper. The EM radiation generated in the slow-wave circuit is

observed in the port indicated by a square under the left in Fig. 3 connected with the coplanar stripline on the cathode side. The expected mode of EM wave received in the port is a quasi-TEM mode, and the electric field distribution is shown in Fig. 4.

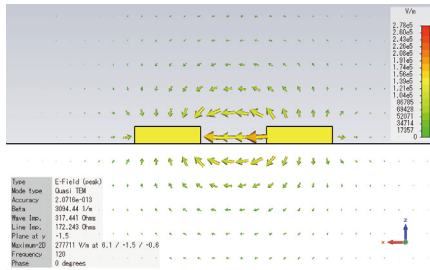


Fig.4. Distribution of electric field at the port

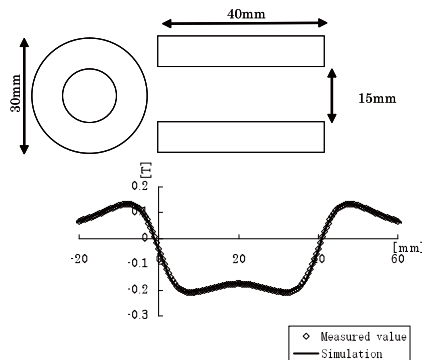


Fig.5. Distribution of magnetic field along the axis

In this simulation it is assumed that the electron beam is emitted from the surface of the cathode along the axis with an equal energy of 10 keV, and the current is from 50 to 100 mA ($5 - 10 \text{ A/cm}^2$). The axial magnetic field to prevent the electron beam from being scattered is generated with the doughnut type neodymium magnet of 15 mm in the inside diameter, 30mm in the outside diameter, and 40mm in the axial length. An almost homogeneous axial magnetic field of 0.17 to 0.2 T can be obtained by this magnet as shown in Fig. 5.

Figure 6 shows the signal of the EM wave observed at the port when the beam current is 100 mA. The signal begins to increase at about 8 ns after the injection of the beam, and a steady radiation is achieved in 14 ns. The output power at the steady state is 700mW. A FFT analysis shown in the lower

graph of Fig. 6 indicates the signal of the port is a single spectrum at a frequency of 102GHz. This frequency is corresponding to that expected from the intersection of the beam mode and the dispersion of the slow-wave circuit.

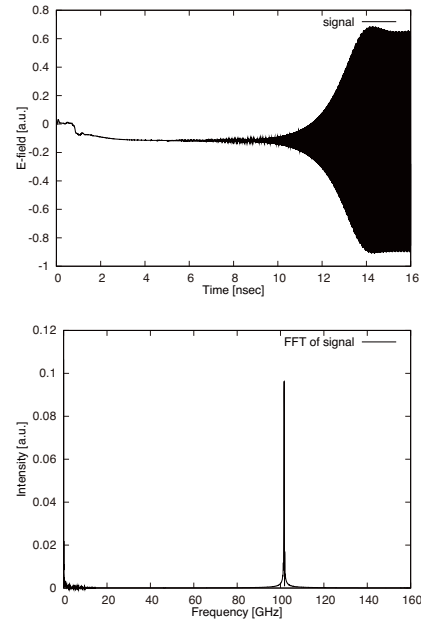


Fig.6. A signal at the port and FFT analysis

Figure 7 represents a typical energy distribution of the electron beam during the steady radiation. A bunch of electrons corresponding to the fundamental period of the slow-wave circuit is formed as a result of the interaction with the EM radiation. Only a vicinity of the electron beam near the SWS can interact with the EM wave.

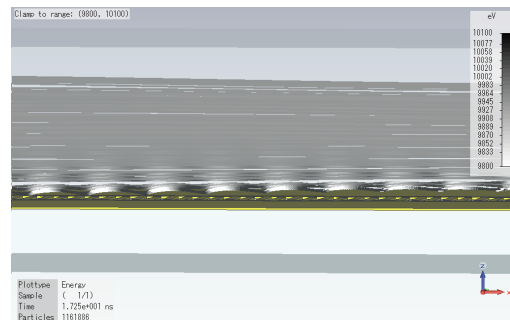


Fig.7. Energy distribution of electrons during radiation

The output power of a radiation when the beam current is changed from 50 to 100 mA is plotted in Fig. 8. The almost linear increase of output power as the injection power of electrons increases suggests

that the ratio of the interactive part of the electrons is unchanged. A radiation is not observed in the current of 50 mA because of the lack of the simulation time (up to 100 ns) or the joule loss in the slow-wave circuit. Moreover the start time decreases as the current increases. The large current contributes to the intense radiation due to the strong coupling to the EM wave. To obtain the radiation in this slow-wave circuit under the present condition, the electron current of more than 60 mA (the current density of about 6 A/cm²) is required.

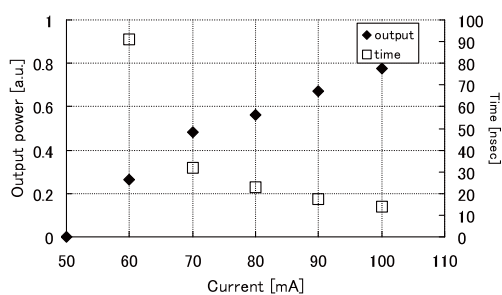


Fig.8. Current vs output power and start time

4. Experimental test of electron gun

The designed electron gun was experimentally evaluated. We used Ir coated impregnated cathode as the emitter [4]. The schematic experimental device is shown in Fig. 9. The electrons that flow into the drift space are received with the collector, and the observation currents are plotted in Fig. 10.

The maximum total current of 3.3 mA is observed at 650 V in the acceleration voltage. The currents are proportional to the 1.6th power of the acceleration voltage. This result suggests that the current is limited by the space charge. The electron beam that has flowed into the drift space is about 65 % of the total current. This is because the electron beam is absorbed to the anode due to misalignment of the magnet, the cathode, and the anode.

It is important to inject the electron-beam with an enough constant current density into the interacting region in order to get a steady radiation of BWO. Because the strong magnetic field guides beam to the axial direction, the current density doesn't change greatly even if the 35 % of the beam hits the anode in

our electron gun. The result of current measurements suggests that the electron-beam obtained by the electron gun has sufficient energy and emission current density for the radiation.

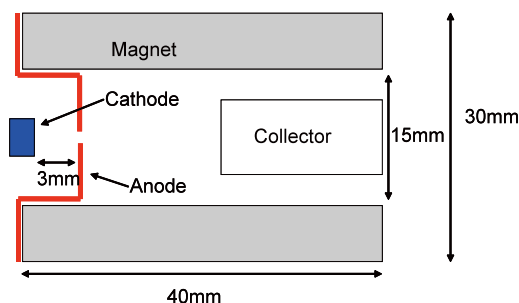


Fig.9. Illustration of experimental device

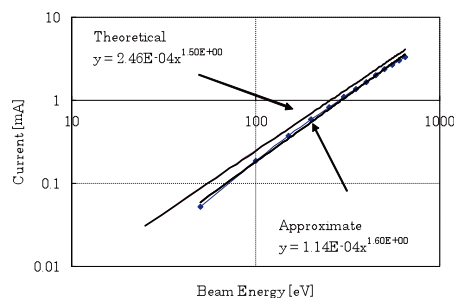


Fig.10. Beam energy vs current in drift space

5. Conclusions

We designed interdigital BWO at a frequency of 100GHz for the electron beam of 10 keV. The particle simulation using CST studio showed that when the electron-beam of 10kV in the acceleration voltage and the current 100mA is injected, the EM radiation of frequency 102GHz with output power of 700mW was observed. This is about five times larger than the present BWO with a same range.

An experimental evaluation was carried out about the designed thermionic electron gun. We confirmed the electron-beam emitted from the electron gun has sufficient energy and emission current for the radiation.

References

- [1] G. Kantorowicz and P. Palluel, "Backward Wave

Oscillators”, Infrared and Millimeter Waves, Vol.1 Sources of radiation, edited by K. J. Button pp.185-211 (1979).

- [2] Carol L. Kory and James A. Dayton, Jr, “Interaction Simulations of Two 650 GHz BWOs Using MAFIA”, Vacuum Electronics Conference, 2008. IVEC 2008. IEEE International, pp.390-391 (2008).

- [3] Carol L. Kory and James A. Dayton, Jr, “Design of 650 GHz Helical BWO Using CST Studio Suite”, Vacuum Electronics Conference, 2008. IVEC 2008. IEEE International, pp.392-393 (2008)

- [4] S. Kimura, T. Yakabe, S. Matsumoto, D. Miyazaki, T. Yoshii, M Fujiwara, and S. Koshigoe : “Ir-Coated Dispenser Cathode for CRT”, IEEE TRANSACTION ON ELECTRON DEVICES, Vol.37, No.12 pp.2564-2567 (1990)

Longitudinal Bunch Compression Study with Induction Voltage Modulator

Akira Nakayama¹, Yoshifumi Miyazaki¹, Takashi Kikuchi², Mitsuo Nakajima¹, and Kazuhiko Horioka^{1*}

¹*Department of Energy Sciences, Tokyo Institute of Technology,
Nagatsuta 4259, Midori-ku, Yokohama, 226-8502, Japan*

²*Department of Electrical Engineering, Nagaoka University of Technology, 1603-1 Kamitomioka, Niigata 940-2188, Japan*

For the beam driver of inertial confinement fusion, the technology to compress charged particle beam in longitudinal direction is crucially important. However, the quality of the beam is expected to be deteriorated when beam is rapidly compressed in the longitudinal direction. In order to investigate the beam dynamics during the bunch compression, we made a compact beam compression system and carried out beam compression experiments. In this paper, we show the background of study and recent progress of the beam compression experiments.

Keywords: Beam bunching, Induction accelerator, Emittance, Switching device

I. INTRODUCTION

Nuclear fusion is expected as one of the future energy sources. In the case of inertial confinement nuclear fusion, millimeter-sized fuel is heated and compressed by irradiation with laser or particle beams of 10nsec pulse length. A high power driver of the short pulse is necessary in order to compress the fuel up to fusion ignition level. Heavy ion beams are considered to be potential inertial fusion driver of reactor level. To increase the beam power, we have to raise the beam energy by acceleration and the beam current by compression. At the final stage of the accelerator, we have to raise the charged particle density of the beam by compression in both longitudinal and traverse directions[1].

For the beam driven inertial fusion, we have to increase the beam current to kA level by acceleration and compression. However, the space charge effect disturbs the beam compression rate during the bunch compression. According to the concept of the heavy ion fusion, the beam is accelerated with long pulse and low current during the low energy domain, and the beam current increases by the longitudinal compression as beam energy increases[2–5]. The beam current is expected to increase about 10 times at the final stage of the accelerator.

At the longitudinal compression process, the emittance of the beam increases due to space charge effects[6–8]. Emittance is an index to express the quality of beam and defined by the volume in 6 dimensional phase space. In addition, emittance is an index of degree that beam is able to be compressed and focused. In other words, the beam can not get expected compression ratio when emittance increases. As factors to decrease the beam compression ratio, followings are considered[9]. They are (1) accuracy of the compression voltage waveform, (2) initial energy spread of charged particles, (3) space charge effect, and (4) collective effects. Above all factors, our final goal is to analyze collective effect on the emittance growth.

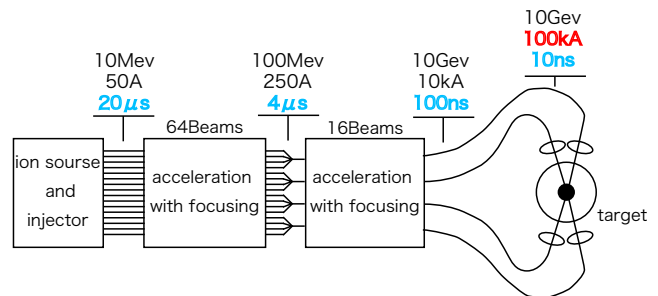


FIG. 1: Concept of HIF with induction accelerator[1]

When beam bunch changes quasi-statically, emittance can keep a constant value. However, it is not the case in the final stage of the high power accelerators. We are going to make the bunch compression experiments with abrupt bunch compression using induction voltage modulator. The modulated beam is compressed through a solenoidal transport line. All of the emittance increase can be reflected only to the longitudinal direction by limiting the influence of traverse motion of the beam. In other words, the beam current waveform observed in the experiment includes all influence factors for compression ratio. Basically, we can include influence and predict the factors (1)-(3) in numerical calculations. We can evaluate collective effect on the emittance growth by comparing experimental value with the numerical calculation in which factors (1)-(3) are included.

As the first step of the bunch compression study, we improved accuracy of the compression voltage waveform than the previous device by using higher-speed semiconductor device[9].

II. EXPERIMENTAL METHOD

We explain our device for the beam compression experiment. Figure 2 shows a schematic diagram of the experimental arrangement. The experimental device consists of an electron gun which makes electron beam bunch, an induction modulator to form the compression volt-

*Electronic address: khorioka@es.titech.ac.jp

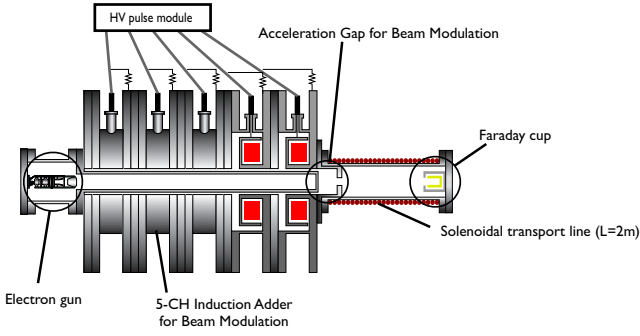


FIG. 2: Setup for beam compression experiment

age, and a solenoidal beam transport line to transport and suppress the transverse motion of the beam.

First, electron beam bunch is formed by the electron gun. Second, compression voltage is applied at the acceleration gap. Finally, the beam is bunched during a bunching distance through the solenoidal transport line, in which transverse motion of the beam is suppressed. As the front of the beam is decelerated by the modulation voltage so as to catch up the front of the beam, the beam bunch is compressed up to the ratio that is determined with the influence factors.

A. ELECTRON GUN

To make the beam compression experiment with laboratory level, we used electron beam because the reaction for the acceleration and the modulation voltage is much faster than heavy ion beam[10].

We show a schematic diagram of the electron gun in Fig 3. In the figure, H is the heater of which normal rating is 6.3V and 95mA, K is the cathode, G1 is grid to control bunch length of electron beam, G2 is grid to control focusing, P1 and P2 are focus electrodes, X is X deflector electrode, and Y is Y deflector electrode. The electron beam is generated by thermionic emission, and extracted as a pulsed beam by a high-speed gate pulser. We could get a beam bunch with quasi-constant energy by extracting it with electrostatic field and the gated operation of the gun.

B. FET DRIVER

The induction modulator is driven by five independent units. The output of each unit is basically sinusoidal, and their waveforms are synthesized in the acceleration gap.

Because high speed switching is necessary in our experiment, we used MOSFET as the switching device. We connected four MOSFET devices in series. We show circuit diagram of the FET driver in Fig 4. As shown, each

sine wave of the pulse is controlled by the FET-based switching circuit.

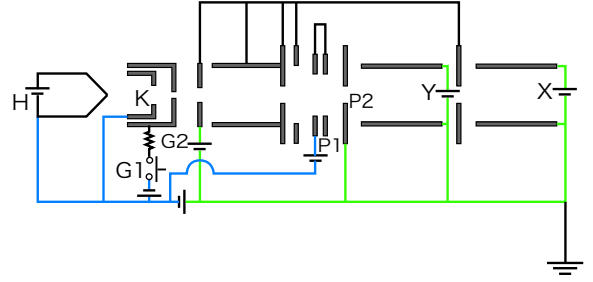


FIG. 3: Schematic of electron gun

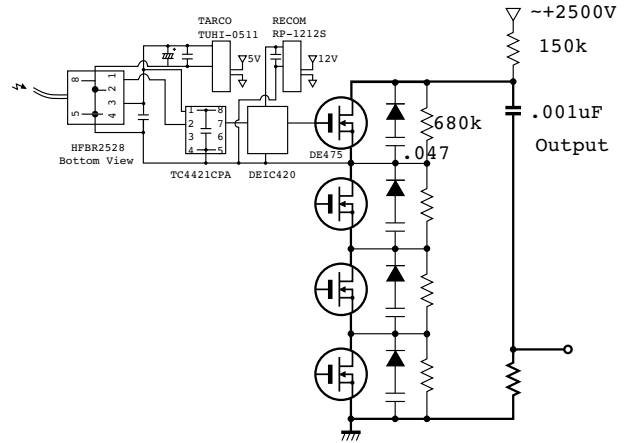


FIG. 4: Equivalent circuit of FET driver

C. INDUCTION MODULATOR AND SOLENOIDAL TRANSPORT LINE

Our induction modulator is driven by five modules as shown in Fig 2. Each module is driven independently by each FET driver. Five voltage waves transmitted from five FET driver are added with the induction modulator at the acceleration gap. Therefore, composite voltage is applied at the acceleration gap. Magnetic cores inside the induction modulator are made of FINEMET which has high saturation magnetic induction at high frequency. During driving of the induction modulator, the induction modulator must be operated within the saturation level.

When the beam passages the acceleration gap, the composite compression voltage is applied for the bunch modulation. Afterward, the beam is compressed during the transportation in the solenoidal line of 2m in length[11–13]. When we extract the electron beam at 2.8kV, speed of the beam is about 3.1×10^7 m/s. Because the distance from the electron gun to the gap of the induction modulator is about 60cm, the electron beam arrives at the acceleration gap after about 20ns from the

extraction. Therefore, in order to apply the compression voltage to the acceleration gap, we adjust the timing of the pulser to 20ns after the gate pulse voltage to modulate the electron beam. We drove electric current of 50A to the solenoid coil and made magnetic field of 0.03T in the transport line. The traverse motion of the beam is limited by the axial magnetic field.

III. COMPRESSION VOLTAGE WAVEFORM

When all particles in the beam bunch has the same velocity and there is no space charge effect and no collective effect, ideal compression voltage can compress the beam bunch into one point at the destination. Such ideal compression voltage waveform is expressed in the following expressions,

$$V(t) = \frac{m_e}{2q_e} \cdot \frac{1}{\left(\sqrt{\frac{m_e}{2q_e V_0}} + \frac{T-t}{L}\right)^2} - V_0 \quad (1)$$

where V_0 is extracting voltage of the beam, so that energy of the beam is eV_0 . T is pulse length of the beam and controlled by the pulse voltage of G1. L is transport length of the beam. In our experiment, we compress the pulse beam of 100ns with the energy of 2.8keV during the 2m transport after applying the compression voltage.

A. PREVIOUS COMPRESSION VOLTAGE WAVEFORM

We show the compression voltage waveform which we used in previous experiments in Fig 6. We performed the beam compression experiment with the compression voltage which is shown in Fig 6. As Fig 6 shows, there are errors between the ideal waveform and the composited waveform made by the five module voltage. When the waveform error occurs, the compression of the beam becomes not ideal. We show the typical compression beam current waveform before and after the compression in Fig 7. We can understand that the beam bunch of 100ns

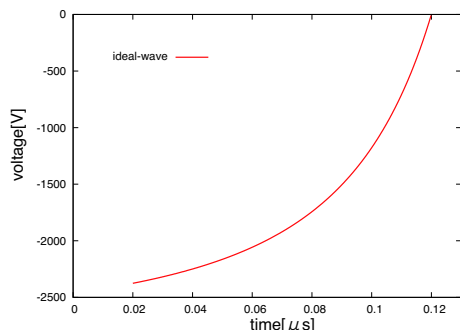


FIG. 5: Ideal compression voltage waveform

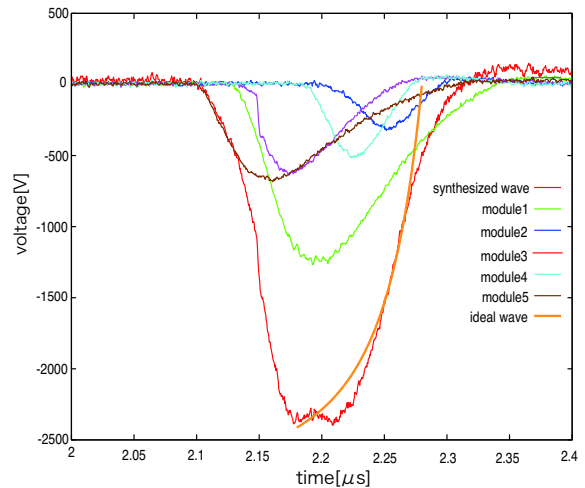


FIG. 6: Previous compression voltage waveform

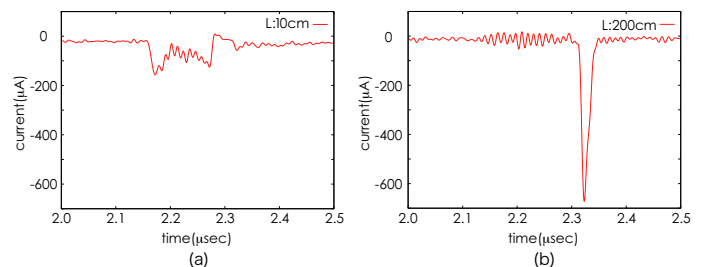


FIG. 7: Beam current waveform modulated with previous compression voltage waveform at transport distance (a) $L=0.1\text{m}$ and (b) $L=2\text{m}$

shown in Fig 7(a) was compressed to the beam bunch shown in Fig 7(b) during transport length of 2m. The beam current waveform in Fig 7 shows that the beam bunch was compressed with finite ratio estimated to be about six or seven. One of the major cause of the decreased compression ratio is the accuracy of the compression voltage waveform. The result indicates the necessity to improve the accuracy of the compression voltage waveform shown in Fig 6.

B. IMPROVEMENT OF COMPRESSION VOLTAGE WAVEFORM

We drove induction modulator with MOSFET which is faster than the previous one, and improved the compression voltage waveform. Also we adjusted capacitance, inductance, resistance, and the operating voltage of FET driver in order to get ideal compression voltage waveform. We were able to improve the compression voltage waveform by adjusting the timing of signal of each FET driver.

The improved compression voltage waveform is shown

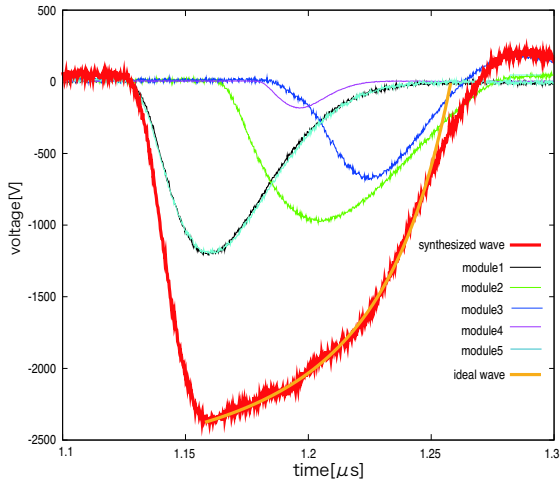


FIG. 8: Improved compression voltage waveform

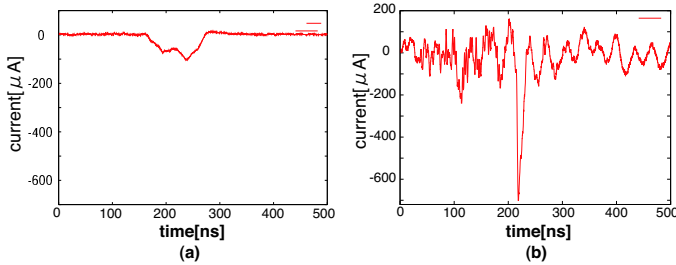


FIG. 9: Beam current waveform operated with improved compression voltage waveform at transport distance (a) $L=0.1\text{m}$ and (b) $L=2\text{m}$

in Fig 8. When we compare the improved compression voltage waveform in Fig 8 with the previous compression voltage waveform in Fig 6, we can understand that accuracy of the compression voltage waveform was improved in the head and the tail of voltage waveform.

In Fig 9, we show the result of beam compression ex-

periment with the improved compression voltage shown in Fig 8. The compression ratio was estimated to be about 8.

However, electromagnetic noise disturbed the current signals as shown in Fig 9(b). It is considered that we can evaluate the influence of accuracy of the compression voltage waveform on the beam compression ratio more precisely by suppressing the electromagnetic noise.

IV. CONCLUDING REMARKS

In high energy density science using high power beams, technology to compress the beams in longitudinal direction is crucially important[15]. We constructed a small system which can examine the longitudinal compression process of beams with laboratory level device.

We improved accuracy of the compression voltage waveform by using higher-speed switching device which drives induction modulator. Experimental results showed that the evaluation was disturbed due to electromagnetic noise and we were not able to evaluate influence of accuracy of the compression voltage waveform on the beam compression ratio precisely. In the near future, we will evaluate influence of accuracy of the compression voltage waveform on the beam compression ratio precisely by suppressing the electromagnetic noise. Our final goal is to discuss collective effects on the compression ratio, i.e., the emittance growth during longitudinal manipulation.

V. ACKNOWLEDGEMENT

The authors would like to express their gratitude to Prof. K.Takayama and Mr. X.Liu for their interests and encouragement to this study.

This work was partly supported by Grant in Aid for Scientific research(A) from the Japan Society for the Promotion of Science(JSPS).

-
- [1] Bangerter,R.O, *Fusion Eng.Des.* 44 (1998) 71
 - [2] Fridman A, *American Institute of Physics.* 0-7354-0101-0/02 (2002)
 - [3] Lee E P and Hovingh J, *American Institute of Physics Conference Proceedings.* No249,PT.2,1713-1724 (1992)
 - [4] Katayama T, Sakumi A, Horioka K, *Journal of Plasma and Fusion Research.* Vol.77,No.1,15-51, (2001)
 - [5] Kim C H and Smith L, *Particle Accelerators.* Vol.18,pp.101-113 (1985)
 - [6] Lawson J D, *CLARENDON PRESS OXFORD.* (1977)
 - [7] Reiser M, *JOHN WILEY & SONS,INC.* (1994)
 - [8] Kikuchi T, Horioka K, Nakajima M, *et. al., Nucl. Inst. Meth.* A-577, 103-109 (2007)
 - [9] M.Tomii T,Kikuchi M,Nagajima M,Horioka K, 6th International conf. International Fusion Sci.Application(2009)
 - [10] Kishek,R.A, *et. al., Nucl. Inst. Meth.* A-544, 179-186 (2005)
 - [11] Molvik,A.W and Faltens A, *Nucl. Inst. and Method in Physics research.* A 464 (2001) 445-451
 - [12] Takayama K, Koseki K *et. al., PRL.* 94,144801 (2005)
 - [13] Takayama K and Kishiro J, *Nucl. Inst. and Meth.* A451/1,304-317 (2000)
 - [14] Kikuchi T and Horioka K, *Phys. Plasmas.* 48, 037002 (2009)
 - [15] Kikuchi T and Horioka K, *Nucl. Inst. Meth.* A-606, 31-36 (2009)

Theoretical Study on Population Inversion of Hydrogen-like Nitrogen in Recombining Plasma

T. Ozawa, Y. Ishizuka, H. Kumai, E. Hotta, K. Horioka, and T. Kawamura

*Tokyo Institute of Technology, Department of Energy Sciences,
Nagatsuta 4259, Midori, Yokohama, Kanagawa.*

ABSTRACT

Discharge produced plasma (DPP) is a promising tool to generate effective extreme ultraviolet (EUV) light. Hydrogen-like nitrogen ions are one of good candidates to get photons at about 13.4 nm with an optical allowed atomic transition from $n=3$ to 2, where n stands for a principal quantum number. To get an optimum condition for the generation of about 13.4 nm laser light, we focus on the properties of population inversion between $n=3$ and 2 in recombining phase. Population inversion is calculated in the framework of population kinetics and an inversion factor F is estimated. The higher plasma density is up to 10^{19} cc^{-1} , the higher F can be obtained and the shorter becomes the duration of the population inversion. Finally, to get enough GL , where G is a gain for raising at about 13.4nm, and L is created plasma length (L is determined by the duration), the competition between the increase in F and the reduction of the duration at higher plasma density seems to be very critical.

Keywords

Discharge produced plasma, Population inversion, Extreme ultraviolet light, Hydrogen-like nitrogen

1. Introduction

A short-wavelength light source has been used for such industrial applications as nanostructure imaging and creation [1]. Especially, extreme ultraviolet (EUV) light is one of the most promising candidates for the next generation lithography. The wavelength of EUV light is typically 5 ~ 40 nm, and can be obtained by creation of hot dense plasma. The EUV light generation has been experimentally done by intense laser light and high current discharge [2,3]. In general, hot dense plasma creation by discharge seems to be more efficient due to its compact and simple scheme compared with that by laser irradiation [4]. In this study, hydrogen-like nitrogen is focused as one of EUV light emitters of which wavelength is about 13.4 nm. The wavelength is near that for the next generation semiconductor lithography, and may be expected to have potential for the industrial use described above. The 13.4 nm light comes from an optical allowed transition from

$n=3$ to 2 (Balmer- α). To get enough intensity of the radiation, nitrogen must be ionized up to the ionization degree of six, and the associated atomic states are higher ones compared with the conventional hydrogen-like line emission, for example, $Ly-\alpha$ and $Ly-\beta$ and so on. Therefore, a recombination scheme may work well. In the scheme, hot dense fully stripped nitrogen plasma is created and the hydrogen-like nitrogen is populated by collisional recombination with rapidly plasma expansion and cooling, resulting in the creation of population inversion and the lasing of Balmer- α . A research with a magnetohydrodynamic (MHD) and a plasma ion kinetics codes for Z-pinch recombination pumping was done [5]. However, in this study, because of plasma motion, understanding for the lasing characteristics in the viewpoint of atomic population kinetics is not clear. To gain insight into the efficient generation of the EUV laser light, population kinetics simulation with a stepwise

cooling profile for the electron temperature is carried out. The ion density is kept constant since clear dependence on the plasma parameters may be obtained. In a sense, this cooling condition is expected to give us strong nonequilibrium properties on atomic processes, and a maximum inversion factor can be expected. Finally, we can gain an insight into the potential of the lasing of nitrogen at about 13.4 nm and an optimum condition to create a population inversion between $n=3$ and 2.

2. Estimation of lasing performance

The laser intensity I is expressed by using the incident intensity I_0 ,

$$I = I_0 e^{GL}. \quad (1)$$

Here, L is plasma length, G is a gain coefficient, and the product GL is an index to show lasing performance [6]. With the cross-section of stimulated emission σ_{stim} , the gain coefficient of Balmer- α is

$$G = N_{n=3} \sigma_{\text{stim}} F, \quad (2)$$

where F stands for an inversion factor and can be written as follows.

$$F = 1 - (N_{n=2} / g_{n=2}) / (N_{n=3} / g_{n=3}) \quad (3)$$

$N_{n=2}$ and $N_{n=3}$ are the population density of $n=2$ and 3, respectively. $g_{n=3}$ and $g_{n=2}$ are the corresponding statistical weights. In this study, $N_{n=3}F$ is focused to evaluate the gain, and normalized population inversion

$$\int_0^\tau N_{n=3} F dt / n_i \tau, \quad (4)$$

is defined. Here, τ is the duration where population inversion between the target atomic levels is created.

3. Simulation conditions

In plasma, atoms and ions undergo transitions between the quantum states through radiative and collisional processes [7].

Table 2.1 Plasma parameters.

ion density n_i [cc ⁻¹]	temperature [eV]	
	initial: T_H	final: T_L
$10^{16} \sim 10^{20}$	300 ~ 800	150
	200 ~ 700	100
	100 ~ 600	50
	100 ~ 600	10

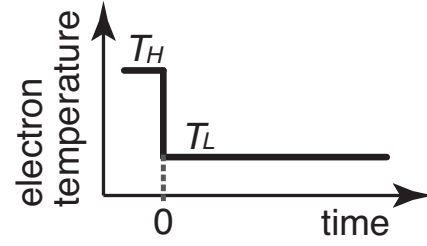


Fig. 2.1 Time evolution of electron temperature.

Atomic processes are calculated with rapid plasma cooling. Here, the ion density is kept constant to exclude the effect of fluid motion in the calculation of population kinetics. Table 2.1 shows the plasma parameters which can be obtained in the plasma creation by discharge, and the plasma cooling is assumed to be a stepwise shown in fig. 2.1.

4. Simulation results and discussion

Fig. 3.1 shows the population densities of hydrogen-like nitrogen ions per statistical weights (N/g). The initial electron temperature T_H is assumed to be 300 eV, and the final one is 50 eV. The ion density is 10^{17-18} cc⁻¹. In this case, the population inversion is created, and we can see that $N_{n=3}/g_{n=3}$ is higher than $N_{n=2}/g_{n=2}$. The higher the plasma ion density is, the higher is N/g and the shorter becomes the duration of the population inversion τ . This is because a collision between an ion and an electron becomes frequent with increase in the ion density. The plasma length L can be approximately estimated by the product of τ and the speed of light c . For example, when the initial and the final temperatures are 300 eV and 10 eV and the ion density is 10^{19} cc⁻¹ (the corresponding result is not given in fig. 3.1.), L is on the order of about ten centimeters. L may be enough when the ion density is below 10^{19} cc⁻¹. However, the population inversion quickly reduced and may become too small to amplify the EUV light with decrease in the ion density. The spontaneous emission from $n=3$ to 2 occurs about 10 ps after the population $N_{n=3}$ is created, which can be estimated by the Einstein's transition probability. Hence, the duration of the population inversion must be greater than the time.

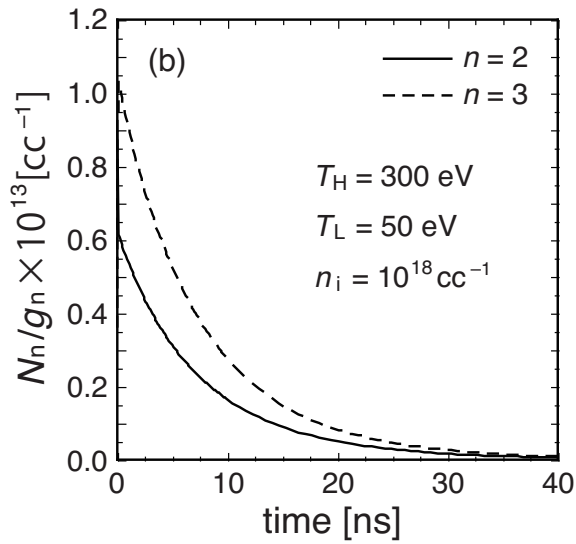
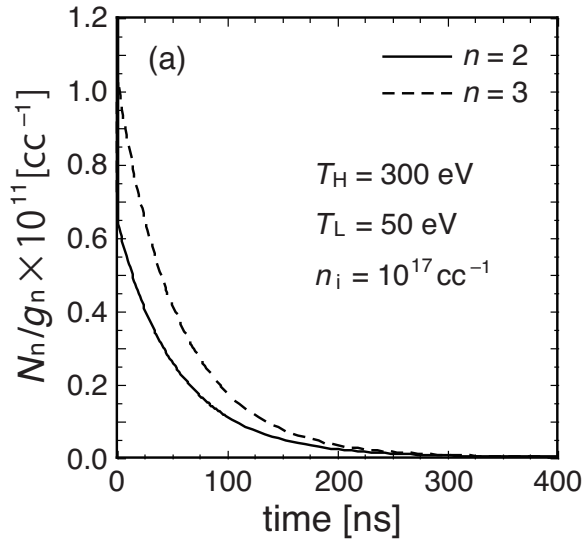


Fig. 3.1 The population densities of hydrogen-like nitrogen ions per statistical weights (n stands for principal quantum number, (a) $n_i = 10^{17} \text{ cc}^{-1}$ and (b) $n_i = 10^{18} \text{ cc}^{-1}$).

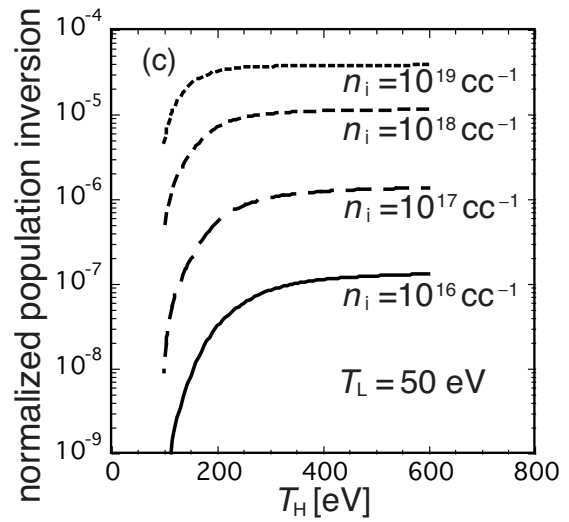
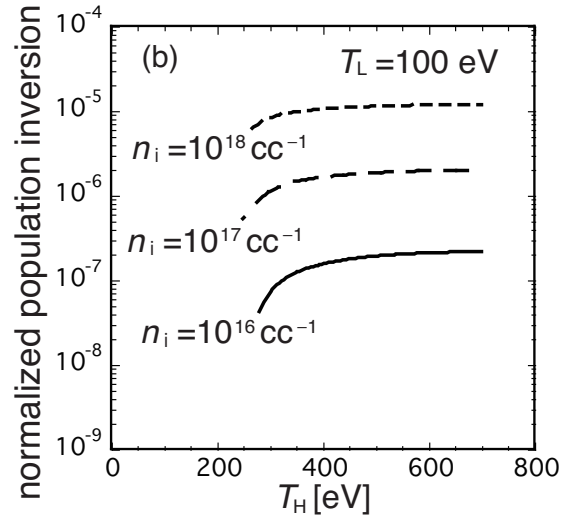
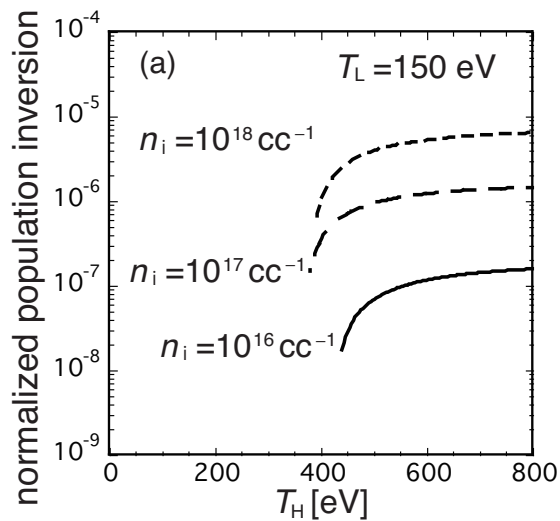


Fig. 3.2 Normalized population inversion at (a) $T_L=150 \text{ eV}$, (b) $T_L=100 \text{ eV}$ and (c) $T_L=50 \text{ eV}$.

The dependence of the population inversion on the ion density and electron temperature is evaluated by eq. (4), and shown in fig. 3.2. When the final temperatures T_L are 150 eV, 100 eV and 50 eV, the initial temperatures T_H need respectively 500 eV, 300 eV and 200 eV to create the population inversion. The population inversion increases with increase in the initial temperature T_H , and saturates at certain higher temperature. The reason is that nitrogen is fully stripped at such electron temperature. When the final temperature T_L is higher than 100 eV, the initial temperature T_H needs several hundreds electron volts or more, and when the final temperature T_L is lower than 100 eV, the initial temperature T_H is only about 200 ~ 300 eV.

The higher the ion density is, the higher is the population inversion. However, when the ion density is 10^{19} cc^{-1} , population inversion is not created at the final temperatures T_L of higher than 100 eV.

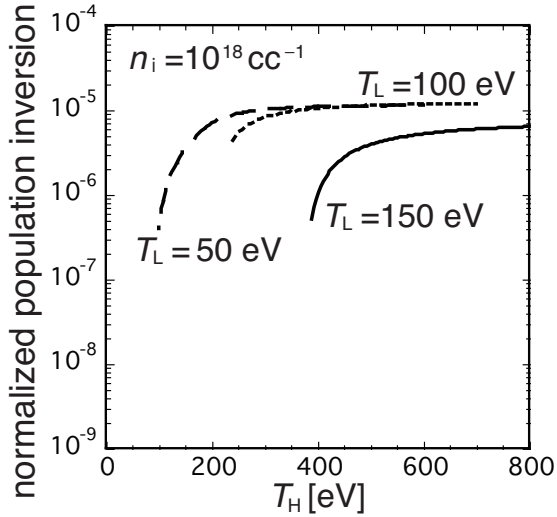


Fig. 3.3 Normalized population inversion at $n_i=10^{18} \text{ cc}^{-1}$.

Fig. 3.3 shows that the population inversion at the ion density of 10^{18} cc^{-1} . It indicates that the maximum of the population inversion is almost determined by the ion density, not by the final temperature T_L .

5. Conclusions

In this study, to get an optimum condition for the generation of about 13.4 nm laser light, we focus on the properties of the population inversion between $n=3$ and 2 (Balmer- α) in recombining phase. In the estimation of the inversion factor F , it is found that higher F can be obtained at higher plasma density. However, the duration of the population inversion τ becomes shorter with increase in the plasma density. Since the duration may become too short to get enough GL , the plasma density cannot be high. Numerical simulation of the population inversion with a stepwise cooling shows that the difference of the electron temperatures between T_H and T_L is about a few hundreds electron volts at $T_L \leq 100 \text{ eV}$. The maximum of the population inversion is almost determined by the ion density, and has a weak

dependence on T_L .

In the future, since we focus $N_{n=3}F$, the gain coefficient must be estimated. In the estimation, the spectral broadening is essential, and the Stark broadening may play an important role to determine the coefficient. We will report the results somewhere.

References

- [1] D. T. Attwood, "Soft X-rays and extreme ultraviolet radiation", Cambridge University Press (1990).
- [2] D. L. Matthews et al., *Phys. Rev. Lett.*, "Demonstration of a Soft X-Ray Amplifier" **54**, pp.110-113 (1985).
- [3] M. C. Marconi and J. J. Rocca, "Time-resolved extreme ultraviolet emission from a highly ionized lithium capillary discharge", *Appl. Phys. Lett.*, **54**, pp.2180-2182 (1989).
- [4] J. J. Rocca et al., "Demonstration of a Discharge Pumped Table-Top Soft-X-Ray Laser", *Phys. Rev. Lett.*, **73**, pp.2192-2195 (1994).
- [5] P. Vrba, et al., "Modeling of capillary Z-pinch recombination pumping of boron extreme ultraviolet laser", *Phys. Plasmas*, **16**, 073105 (2009).
- [6] R. C. Elton, "X-ray lasers", Academic Press, Inc. (1990).
- [7] T. Fujimoto, "Plasma Spectroscopy", Clarendon Press (2004).

Analysis of Highly Ionized N Plasma Spectra under the Effect of an External Magnetic Field in Fast Capillary Discharge

Hideaki KUMAI, Yuya ISHIZUKA, Masato WATANABE and Eiki HOTTA

*Tokyo Institute of Technology, Department of Energy Sciences,
Nagatsuta 4259, Midori-ku, Yokohama 226-8502*

ABSTRACT

It is considered that lasing of a H-like N Balmer α soft X-ray laser (SXRL) at wavelength of 13.4 nm might be possible by utilizing an expansion phase of Z-pinch discharge plasma. To realize the SXRL, we studied the soft-x-ray amplification in discharge-produced plasma under an externally applied axial magnetic field. The purpose of this technique is to make the concave electron density distribution at the time of lasing and amplify the radiation by guiding effect.

I. Introduction

Quantum soft X-ray laser (SXRL) has been investigated for a few decades due to its narrow bandwidth, high coherence and directivity. It becomes a tool to elucidate the problem of solid state physics, nanotechnology, and life science. The main x-ray laser medium is plasma produced by laser irradiation or capillary discharges. In comparison with a laser-pumped x-ray laser, the capillary discharge scheme has the advantages of relatively high efficiency, large gain volume, and long gain duration.

In 1994, utilizing a fast capillary Z-pinch discharge to generate a plasma column efficiently, Ne-like Ar SXRL at a wavelength of 46.9 nm was demonstrated by Rocca et al. [1]. In addition, suppressing the growth of magnetohydrodynamic (MHD) instability by use of predischARGE, lasing of Ne-like Ar laser became to be reproducibly observed [2].

Concerning the generation of a shorter wavelength SXRL pumped by capillary discharge scheme [3, 4, 5], we investigated possibility of lasing the H-like N Balmer recombination SXRL at a wavelength of 13.4 nm. The wavelength of 13.4 nm is in an extreme ultraviolet range, therefore a Mo/Si multilayer mirror can be applied to the capillary discharge for SXRLs.

To realize the SXRL, we studied the soft-x-ray amplification in discharge-produced plasma in an externally applied axial magnetic field. Applying an axial magnetic field to the plasma is a well-known technique to suppress plasma instabilities during implosion, and has been used in several experiments including generation of high density plasma [6]. In this experiment, the purpose of this technique is to generate a concave plasma density distribution at the time of lasing. At and after the maximum

pinch, a convex electron density distribution will be formed in usual Z-pinch plasma. This electron density distribution refracts the ray of light off the axis, as shown in Fig.1. Refraction decreases the effective gain coefficient and limits the maximum gain-length product that could be obtained. For this reason, we aimed to make the concave electron density distribution at the time of lasing by applying axial magnetic field and amplify the radiation by guiding effect. In this paper we discuss the results of the study of soft x-ray amplification in a discharge-produced plasma column under the influence of an axial magnetic field.

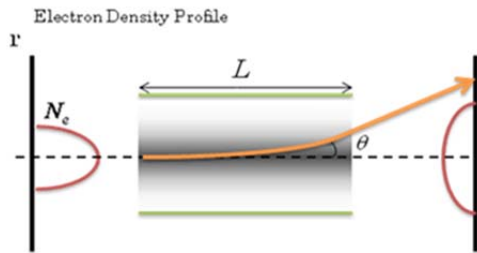


Fig.1. Refraction effect of electron density gradient

II. Experimental setup

Capillary discharge plasma was generated by utilizing a triangular current with peak amplitude of about 50 kA and a pulse width of about 50 ns. A pulsed power supply system with a pulse shaping transmission line as shown in Fig. 2 was used [7, 8]. An alumina (Al_2O_3) ceramics capillary with an inner radius of 1.5 mm and a length of 150 mm was filled with initial nitrogen molecular gas at pressure of about 600 mTorr.

The gas was pre-ionized by RC discharge with amplitude of about 10 A and a decay time constant of 3 μs . Schematic diagram of time

integrated spectrum pinhole imaging set-up is illustrated in Fig. 3. The measurement of radiation from the nitrogen plasma was carried out using a transmission grating spectrometer with a lattice constant of $1/1000 \text{ mm}^{-1}$ in combination with an X-ray CCD camera which has 1024×1024 pixels. Each pixel has an area of $13\text{-}\mu\text{m}$ square. The transmission grating was placed at a distance of 600 mm from the end of capillary and a distance between the grating and the CCD camera was 425 mm. In addition, two slits of $1 \text{ mm} \times 5 \text{ mm}$ were placed between the capillary and the transmission grating, and the diameter of the transmission grating was 50 μm .

The axial magnetic field was generated by using a 4-cm diameter, 15-cm long coil positioned concentrically with the capillary channel. The coil, which was excited by a DC power supply, produced magnetic fields up to 15 mT.

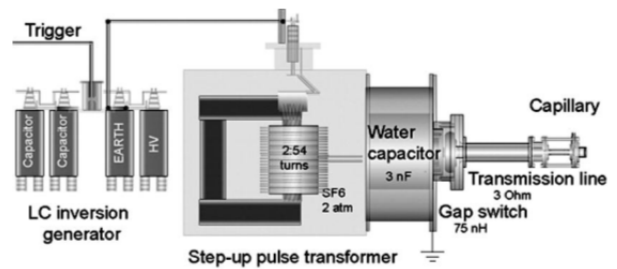


Fig. 2. Experimental setup for lasing H-like N soft X-ray laser

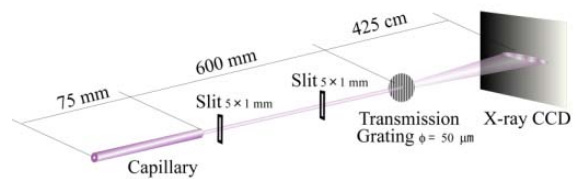


Fig. 3. Time integrated spectrum pinhole imaging set-up

When an axial magnetic field is applied to plasma, the magnetic flux is conserved in the plasma because of induced azimuthal current in plasma shell. The magnetic flux is collected by the imploding plasma, which leads to increase of the magnetic field strength inside the plasma. When the plasma is compressed to a radius of r , the magnetic flux density inside plasma, B , is given by

$$B = \frac{\eta B_0 r_0^2}{r^2} \quad (1)$$

where B_0 , r_0 , and η are the initial magnetic flux density of the external field, initial plasma radius, and leakage of the magnetic flux during implosion.

From previous experimental results, the plasma is compressed to one tenth of initial plasma radius at maximum pinch. Therefore, the multiplication factor of 100 in the magnetic flux density is expected.

III. Experimental results and discussions

The effects of the axial magnetic field [9, 10] on the time-resolved XRD signals radiated from fast capillary Z-pinch discharge plasma are illustrated in Fig. 4. Axial magnetic field inside the plasma opposes the compression force driven by the plasma current. This phenomenon prevents the plasma compression and the increase of the electron temperature and density, which may lead to the decrease of radiation intensity. However no change is observed in radiation intensity with an axial magnetic field. This result indicates that an externally applied axial magnetic field of 15 mT does not significantly affect the evolution of the plasma. The cause may be the negligibly

small compressed axial magnetic field strength $B_z/r^2 \approx 1.5$ T compared with the self-generated azimuthal magnetic field $B_\theta = \mu_0 I / 2\pi r = 33$ T.

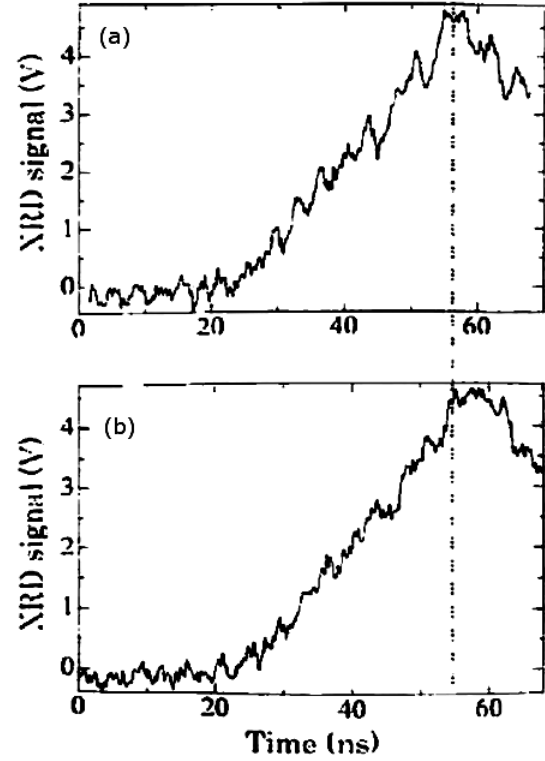


Fig. 4. XRD signals radiated from fast capillary Z-pinch discharge plasma. (a) Without external magnetic field. (b) With axial magnetic field of 15 mT.

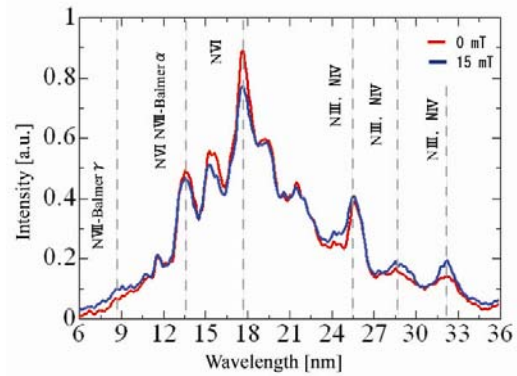


Fig. 5. Emission spectrum profiles without and with axial magnetic field of 15 mT

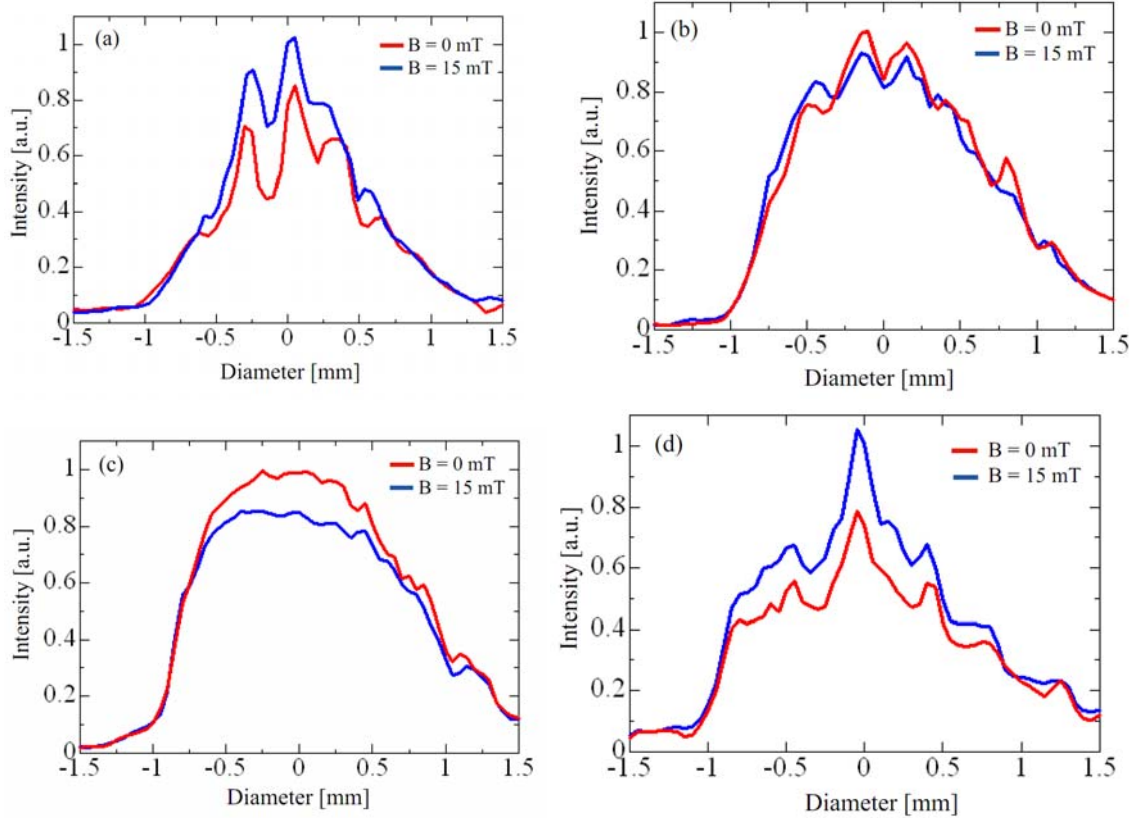


Fig. 6. Soft-x-ray profiles (a) 9 nm, (b) 13.4 nm, (c) 18 nm and (d) 27 nm corresponding to discharges of approximately 45 kA through 15-cm-long, 3-mm-diameter capillary without and with axial magnetic field of 0.15 T

The effects of the axial magnetic field on the intensity profile of the emission spectrum at wavelength of below 27 nm are illustrated in Fig. 5. As shown in Fig.5, the intensities of spectrum line at wavelengths below 6 nm and over 21 nm slightly increase by an axial magnetic field. However, intensity of spectrum line at wavelengths over 20 nm decreases.

Figure 6 shows radiation patterns recorded along the direction of the spectrometer slit under the condition of no external magnetic field applied.

(a) $\lambda=9$ nm

This line corresponds to spectrum of highly

ionized NVII state. The beam profile exhibits a double peak. Since electron temperature of $T_e \approx 150$ eV is needed in order to generate NVII ions, NVII state is considered to be obtained after maximum pinch. Therefore, this line may be affected by convex electron density distribution. The intensity of radiation in axis region obtained without axial magnetic field is lower than that with magnetic field. This result suggests that the ray of radiation is bended off the axial region by convex electron density distribution. With magnetic field, the radiation patterns sharpen and the intensity of radiation increases, suggesting the waveguide effect.

(b) $\lambda=13.4$ nm

This line corresponds to spectra of highly ionized NVI and NVII states. The beam profile also presents a double peak like that of $\lambda=9$ nm. However, the peak is not so clearly seen as that for $\lambda=9$ nm. This result suggests that NVII dominates this line, because discharge current is low (39kA) and this line is few affected by the convex electron density distribution.

(c) $\lambda=18$ nm, (d) $\lambda=27$ nm

These spectra correspond to line emissions from NIV and NIII. Ionization to NIV and NIII of low charge states, which have low ionization potentials, occurs before the maximum pinch. Therefore, these lines are not affected by the convex electron density distribution and the beam profiles also show a single peak. Change in radiation patterns of these lines caused by axial magnetic field is not thought to be induced by waveguide effect.

IV. Conclusion

To realize the SXRL, we studied the soft-x-ray amplification in a capillary discharge in an externally applied axial magnetic field.

The beam profile of $\lambda=6$ nm line (NVII) shows a double peak and the intensity of radiation increases in axis region when axial magnetic field is applied. This result suggests the waveguide effect caused by convex electron density distribution. However, soft-x-ray amplification is very low. One of the reasons may be unsatisfactory ionization by low discharge current. To realize lasing of a H-like N Balmer α soft X-ray laser, discharge current over 50kA is required [11]. In the

experiment, discharge current is only 38kA to prevent breakdown near the electrodes of equipment. In fact, spectrum of NVII which is needed for lasing at wavelength of 13.4 nm is observed even though the emission is weak. To observe the definite effect of axial magnetic field and to realize the x-ray laser, improvement of insulation near electrodes and increase of the discharge current are required.

Another reason is attributed to the low axial magnetic field. Externally applied axial magnetic field of 15 mT is negligibly low compared with the self-generated azimuthal magnetic field. F. G. Tomasel et al. reported the enough soft-x-ray amplification under an externally applied axial magnetic field of 150 mT [10]. By adopting a pulsed power supply for generating axial magnetic field, we would like to obtain a compressed axial magnetic field comparable to the azimuthal magnetic field generated by the Z-pinch discharge current.

Reference

- [1] J. J. Rocca, V. Shlyaptsev, F. G. Tomasel, O. D. Cortázar, D. Hartshorn, and J. L. A. Chilla, Demonstration of a Discharge Pumped Table-Top Soft-X-Ray Laser, *Phys. Rev. Lett.*, Vol. 73, pp. 2192-2195 (1994)
- [2] G. Niimi, Y. Hayashi, N. Sakamoto, M. Nakajima, A. Okino, M. Watanabe, K. Horioka, and E. Hotta, Development and characterization of a low current capillary discharge for X-ray laser studies, *IEEE Trans. on Plasma Science*, Vol. 30, pp. 616-621 (2002)
- [3] P. Vrba, M. Vrbova, N. Dezhda, A.

- Bobrova, and P. V. Sasorov, Modeling of a nitrogen x-ray laser pumped by capillary discharge, *Central European Journal of Physics*, Vol. 3, pp. 564-580 (2005)
- [4] N. S. Kampel, A. Rikanati, I. Be'ery, A. Ben-Kish, A. Fisher, and A. Ron, Feasibility of a nitrogen-recombination soft-x-ray laser using capillary discharge Z pinch, *Phys. Rev. E*, Vol. 78, 056404 (2008)
- [5] Y. Sakai, S. Takahashi, T. Hosokai, M. Watanabe, A. Okino and E. Hotta, The possibility of a capillary discharge soft X-ray laser with shorter wavelength by utilizing a recombination scheme, *Journal of Plasma and Fusion Research Series*, Vol. 8, pp. 1317-1312 (2009)
- [6] Liberman M A, De Groot J S, Toor A and Spielman R B, *Physics of High-density Z-pinch Plasmas*, New York, Springer, 1999
- [7] Y. Sakai, T. Komatsu, I. Song, M. Watanabe, G. H Kim and E. Hotta, High efficient pulsed power supply system with a two-stage LC generator and a step-up transformer for fast capillary discharge soft X-ray laser at shorter wavelength, *Review of Scientific Instruments.*, Vol. 81, 013303 (2010)
- [8] Y. Sakai, S. Takahashi, M. Watanabe, G. H. Kim and E. Hotta, Pulsed current wave shaping with a transmission line by utilizing superposition of a forward and a backward voltage wave for fast capillary Z-pinch discharge, *Review of Scientific Instruments*, Vol. 81, 043504 (2010)
- [9] R. A. London, Beam optics of exploding foil plasma x-ray lasers, *Phys. Fluids*, Vol. 31, p.184 (1988)
- [10] F. G. Tomasel, V. N. Shlyaptsev, and J. J. Rocca, Enhanced beam characteristics of a discharge-pumped soft x-ray amplifier by an axial magnetic field, *Phys. Rev. A*, Vol. 54, No. 3, pp.2474-2478 (1996)
- [11] 酒井雄祐: 修士論文 “高速Zピンチ放電による水素様窒素軟X線レーザー実現に向けた研究” (2010) 東京工業大学

Counter-facing Plasma Guns for Efficient Extreme Ultra-Violet Plasma Light Source

Yuusuke Kuroda¹, Kenji Hayashi¹, Hajime Kuwabara²,
Mitsuo Nakajima¹, Tohru Kawamura¹, and Kazuhiko Horioka^{1*}

Department of Energy Sciences, Tokyo Institute of Technology¹,

Nagatsuta 4259, Midori-ku, Yokohama, 226-8502, Japan

Yokohama Engineering Center, IHI Corporation²,

Shin-nakaharacho 1, Isogo-ku, Yokohama, 235-8501, Japan

A plasma focus system composed of a pair of counter-facing coaxial guns is proposed as a long-pulse and/or repetitive high energy density plasma source. Counter-facing plasma guns using Xe gas demonstrated that, with an assist of breakdown and outer electrode connection, current sheets evolved into a configuration for stable plasma confinement at the center of electrodes. However, low spectral efficiency of Xe plasma is not suitable for high power and highly repetitive operation. Therefore, we applied Li film as the source of plasma for improvement of the plasma conversion efficiency and repetition capability. This paper demonstrates a proof of plasma focus system for Li-based plasma light source, which is expected to have high spectral efficiency.

Keywords: Plasma confinement, EUV light source, Plasma focus, High energy density plasma

I. INTRODUCTION

Recently radiation from high-energy-density plasma is attracting our attention as an Extreme Ultra-Violet (EUV) light source for the next generation semiconductor process. Schemes of the plasma light source are classified as Laser Produced Plasma (LPP) and Discharge Produced Plasma (DPP).

Both high average power and high conversion efficiency are needed for a practical EUV light source. However, sources of light developed now have problems. The average output power is extremely low compared with the requirement. When we increase input power, life time of the device and the optical system are degraded by the huge quantities of thermal load. We should improve energy conversion efficiency ; that is the ratio of input electric energy and output EUV energy. To improve the energy conversion efficiency, we would like to extend the radiative time of source plasma. Then we intend to prolong the lifetime of plasma.

In this study, we applied a counter-facing plasma focus system as the plasma generation

device[1]. The plasma focus system has the possibility to prolong the life time of EUV plasma more than μ second. In addition, we adopt Lithium as the plasma source which has a narrow and strong spectrum at 13.5nm wavelength. By using the counter-facing plasma focus system and Lithium source, we would like to improve the energy conversion efficiency, spectral efficiency and repetition capability[2][3].

The purpose of this study is to improve the energy conversion efficiency by regulating the plasma parameters suitably. To control the plasma dynamics, we optimized the condition of insulator surface between cathode and anode and the discharge parameters.

II. OPERATING PRINCIPLE OF COUNTER-FACING PLASMA GUNS

Figure 1 shows operating principle of the counter-facing plasma guns. A pair of plasma focus electrodes are faced each other, and center electrodes are charged so as to have a reverse-polarity mutually. When electrode gaps are energized by a pulsed high voltage, breakdown occurs on the insulator surface of the coaxial elec-

*Electronic address: kuroda.y.ac@m.titech.ac.jp

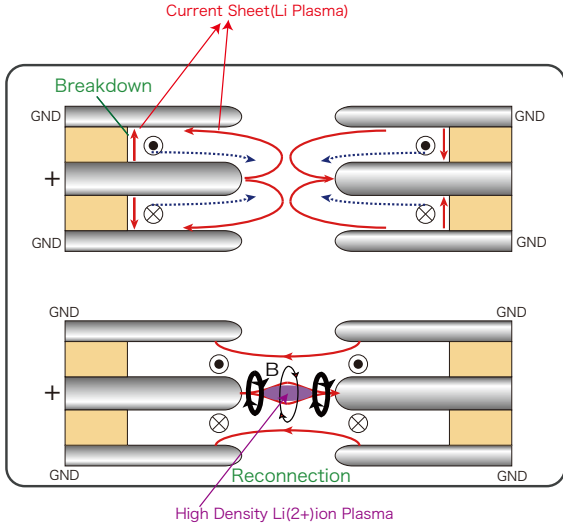


FIG. 1: Schematic diagram of counter-facing coaxial plasma focus system

trodes and current sheets are driven. The radial current carried by the plasma sheet produces magnetic field inside the coaxial electrodes. The magnetic pressure ($\mathbf{J} \times \mathbf{B}$) accelerates the plasma to the top of center electrodes. The plasma collides and is heated up in the center of electrode gaps. The plasma can be confined stably, if symmetry is maintained. When the current sheets reconnect smoothly, the dense, high temperature plasma can make bright EUV radiation for a long time[4][7].

III. EXPERIMENTAL SETUP

The device consisted of a pair of plasma-focus guns, produces high temperature and high density plasma. The vacuum deposition apparatus is used to evaporate and form a well-defined thin Li film on insulator surface for the plasma source. Details of the experimental arrangement are shown in the follow section.

A. Vacuum deposition apparatus for formation of Li-layer

Figure 2 shows the vacuum deposition apparatus for the Li-layer formation for the proof-of-principle experiments. The vacuum deposi-

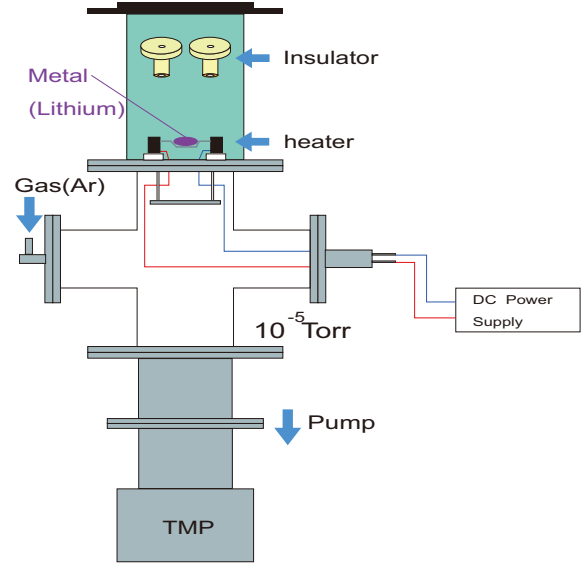


FIG. 2: Vacuum deposition apparatus for Li-layer formation on insulator surface

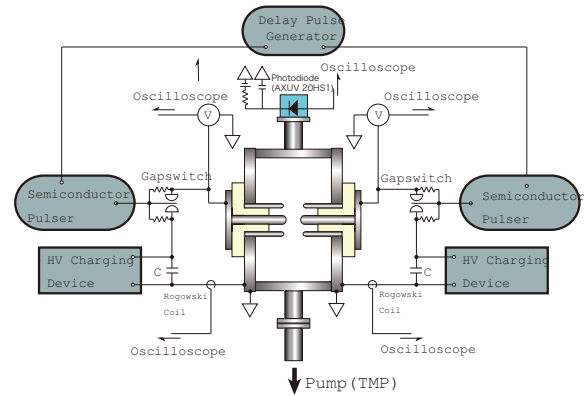


FIG. 3: Schematic of plasma focus and current drive systems

tion apparatus is consisted of a bell-jar made of glass and a vacuum pump[5]. Li is placed on the boat made of turgeten and heated in the vacuum. When the film is formed on the insulator surface by the vacuum deposition process, the boat heating is stopped and the insulator is taken out. The chamber was evacuated to 10^{-5} Torr or less with turbo-molecular pump (TMP).

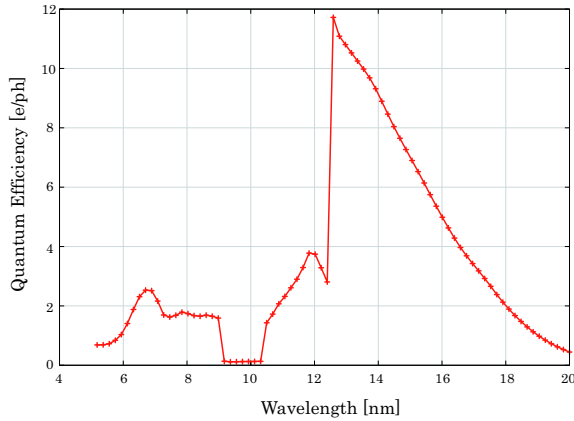


FIG. 4: Spectral sensitivity of the photodiode

B. Plasma focus guns and its operation

Figure 3 shows a schematic of the counter-facing coaxial plasma focus system. In the experiment, high voltage DC [direct-current] power sources charge the $0.8 \mu\text{F}$ capacitors. Trigger signals from pulse generators ignite the gap-switches. When flashover is induced on the insulator surface, current sheets are driven from the facing electrodes. They need to be collided in the center of electrode. We observed time development of the luminescence image by a high speed framing camera (IMACON468 DRS HADLAND). Rogowski coils measure the discharge current. A photodiode (AXUV20HS1) determined EUV light, has a sensitivity peak at the EUV zone. Figure 4 shows the spectral sensitivity of the Si/Zr-filtered photo-diode. The EUV photo-diode is placed at a port perpendicular to the axis of coaxial electrodes.

IV. EUV OPTICAL INSTRUMENTATION AND PLASMA BEHAVIOR

We confirmed that the counter-facing plasma focus system can prolong the EUV radiative time using Xe gas [1][7]. However, Xe plasma does not have enough spectrum efficiency and can not repeat the operation very often due to a finite recovery time of Xe gas. On the other hand, a plasma composed of hydrogen-like Li ions has high spectral efficiency compared with Sn and

Xe. So, thin film of solid Li was applied as the plasma source to the counter-facing plasma focus system. The counter-facing plasma focus system using Li solid thin film needs to be demonstrated whether Li plasma also works well like Xe gas plasma.

Figure 5 shows typical waveforms of the discharge current and EUV signal. The current waveforms were measured by the Rogowski coils and EUV signal using the photo diode. We observed about $1 \mu\text{sec}$ EUV radiative time as shown in Fig.5. The EUV signal is estimated to be corresponding to 72mJ output energy [6].

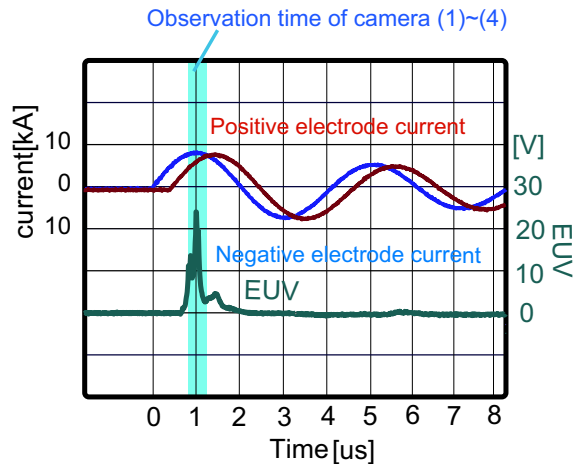


FIG. 5: Waveforms of discharge currents and EUV output power from the pinch plasma made from Li solid layer

The four pictures shown in Fig.6 were taken by the high speed framing camera. Figure 6 shows typical plasma dynamics in the counter-facing plasma focus system with Li plasma source. Behavior of the Li plasma in the plasma focus at discharge time $t=80\text{ns}$, $t=130\text{ns}$, $t=180\text{ns}$, and $t=230\text{ns}$ are shown in Fig.6. These pictures indicate plasma stagnation at the center of the two electrodes.

These results show that the scheme of counter-facing plasma focus is effective also in the system using Li solid thin film. The Li plasma has spectral efficiency intrinsically higher than Xe and Sn plasma. Then the result indicates that both high EUV output power and improvement of efficiency; that is conversion efficiency from input electric energy to output EUV energy, are possible with the Li-based plasma

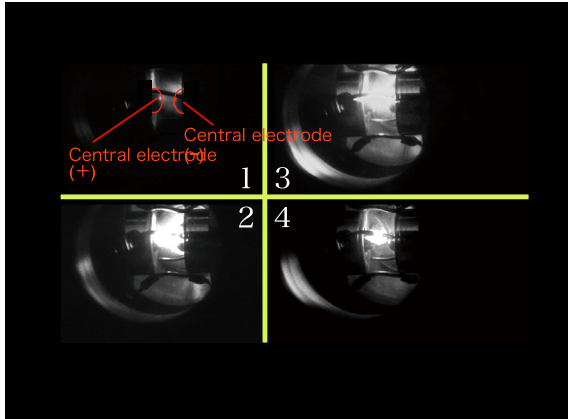


FIG. 6: Plasma dynamics in the counter-facing plasma focus system with Li plasma source

focus system. We confirmed that the counter-facing plasma focus system using Li solid thin film works as that based on Xe gas.

V. CONCLUSION

We operated the counter-facing plasma focus system using Li solid thin film. As a result, we obtained 72mJ output EUV energy. The experimental results show that the concept of counter-facing plasma focus system is also effective for EUV Li plasma confinement the μ -second level. Results also indicate that the system using Li thin film can be a high average power EUV source with high spectral efficiency.

We are going to optimize the experimental conditions such as the Li film thickness or the surface state in future and aim to prolong the EUV radiative time and increase average power of EUV emission.

We would like to express their thanks to Y.Aoyama for useful advice on the plasma formation process.

-
- [1] Yutaka Aoyama, Mitsuo Nakajima, and Kazuhiko Horioka, *Phys. of Plasmas*, 16, 110701 (2009).
 - [2] M.Masnavi, M.Nakajima, E.Hotta, and K.Horioka, *J. Appl. Phys.* 103, 013303 (2008).
 - [3] M.Masnavi, M.Nakajima, E.Hotta, and K.Horioka, *J.Appl. Phys. Lett.* 89, 031503 (2006).
 - [4] Yutaka Aoyama: Plasma Dynamics with Counter Coaxial Electrodes, Department of Energy Sciences, Tokyo Institute of Technology, Master thesis (2008)
 - [5] Daisuke Nunotani: Plasma Dynamics of Li-based EUV source with Counter-facing Electrodes, Department of Energy Sciences, Tokyo Institute of Technology, Master thesis (2009)
 - [6] H.Hayashi, Y.Kuroda, H.Kuwabara, M.Nakajima, K.Horioka, 71st Autumn Meeting, The Japan Society of Applied Physics, 14a-ZA-6 (2010).
 - [7] Yutaka Aoyama, Mitsuo Nakajima, and Kazuhiko Horioka: Plasma Dynamics in Counter-Facing Plasma Guns, NIFS-PROC-82 Mar.17, p.67-71 (2010)

Characterization of the pulsed ion beam in a plasma focus device for Al surface modification

H.M. Liu , D.X. Cheng , H. Ito , K. Masugata

Department of electric and Electronic system Engineering, university of toyama, 3190 Gofuku, toyama 930-8555, Japan

Abstract

Characteristics of the ion beams produced in a plasma focus device were studied. In the experiment, a Mather type plasma focus device was used and was pre-filled with N₂ gas. The plasma focus device capacitor bank of 41.6 μF was charged to 20 kV to get a peak current of 350 kA. Ion beam energy was measured with Time of Flight (TOF), and it showed that when the gas pressure was 15 Pa, ion beam energy reached up to the maximum about 190 keV, and optimum condition for nitrogen ion formation was found to be 15Pa. The XRD patterns of the material deposited at 0° 5° 10° 15° angular position for 3 focus shots were shown. The new peaks at angles $2\theta=26^\circ$ were assigned to the AlN <2 0 0> phase.

Keywords

Plasma focus, pinched plasma, ion beam, Al surface modification

1. Introduce

Plasma focus (PF) has been successfully used as a pulsed ionizing radiation source for many applications: pulsed neutron activation analysis [1], as a high flux X-ray source for lithography and radiography [2], as a highly energetic ion source for processing of materials in the form of thin films [3] and so on. It is an interesting phenomenon that high-energy ions of the order of MeV are produced in plasma focus devices. That energy level is sometimes more than one hundred times as large as bank voltage. The mechanism of the ion has been investigated for several ten years, and various theories have been considered. All the radiation is produced at the high-current discharge

in a vacuum chamber filled with different gases at the pressure of 0.1~10 mbar for nitrogen. The energetic ions emitted from the focus region are suggested for the surface treatment on materials. Kelly et al. found that a thin and well-adhered coating on metallic samples is possible by using a metallic insert in the anode tip. Masugata et al. proposed the pulsed ion beam emitted from DPF for surface treatment on semiconductors. It seems very attractive, especially for high melting point semiconductors such as aluminum nitride. Aluminum has been widely used in industry and in daily life, especially in aerospace applications. However, pure aluminum has a low tensile strength. Aluminum alloy, typically combined with Si, Fe, Cu, Mn, Mg, Cr, Zn, V, Ti, Bi, Ga,

Pb, Zr. AlN is a hard material with 11.8Gpa in Knoop hardness. AlN is the only stable compound in the binary system Al - N and exists in one crystal structure. Pure AlN has a density of 3.26 g/cm³ and dissociates under atmospheric pressure above 2500 °C. Pure AlN is colorless and translucent but is easily colored by impurities. Thus, carbon impurities cause the typical light gray color of AlN powder. AlN powder is susceptible to hydrolysis by water and humidity. This is the reason for its characteristic ammonia smell. Because AlN is a covalent compound, limited atomic mobility prevents complete densification of pure AlN. Thus, relatively high pressures or sintering aids are required to assist densification. Typical sintering additives are rare-earth or alkaline-earth oxides. To achieve high thermal conductivities mostly yttrium compounds are used. The formation and micro structural distribution of yttrium Al's garnet controls both densification and thermal properties.

2. Experiment set up

What we used was Mather type plasma focus device [4]. Mather type plasma focus device is a simple pulsed coaxial plasma accelerator that produces a short but finite two dimensional non cylindrical Z-pinch, at the end of the central electrode, and compresses the plasma to very high densities and temperatures of the order of 1-2KeV. Plasma focus also serves as a source of high energy density ion with energies from few keV to hundreds of keV, X-rays, neutrons and relativistic electrons. The plasma focus possesses the advantages of small size, easy maintenance, and technical simplicity of construction as well as

operation and considerably lower cost over continuous accelerators. Electron and ion beams emitted by PF devices have unique features for each device. The device accelerates the ions to high energy values by means of fast electric discharge of only tens of kilovolts. The energy profile of these ion beams is continuous from a few tens keV to some hundreds keV. The ions coming from the focus region are much more energetic than those present in other material processing reactors. These ions cause the heating of the substrate during a deposition process which eliminates the requirement of separate heating. Another distinct advantage of this technique is that the substrate needs not to be electrically conductive. Thus many of the insulators and semiconductors can be used for surface modification. This technique, when used for material processing purposes, especially in thin film deposition gives the advantages of labor savings, less treatment time, significant reduction in energy consumption and high deposition rates.

Plasma focus device is made up of electrodes and capacitor banks. Electrodes play the main role in the formation of plasma inside the chamber, where working gas is present. It provides the positive and negative polarity to ionize the gas atoms. The electrode arrangement of Mather type plasma focus is shown in Fig1. It consists a central rod which serves as the anode surrounded by 24 coaxial copper rods acting as the cathode. The length of anode rod is 242mm, and the length of each cathode rod is 230mm. A cylindrical insulator sleeve of glass of length 100mm with the inner diameter of 50mm and outer diameter 60mm is placed at the close end of the focus

system around the central anode.

The whole electrode system is kept inside a stainless steel vacuum chamber connected to other equipments with the steel chamber such as the vacuum pump, vacuum meter, gas inlet, etc. The suitable working gas according to the requirement of the experiment is entered in this evacuated steel chamber for the generation of plasma. The main energy system storage consists of a 20 kJ, Mather type PF device as shown in fig. The PF device is consisted of an inner electrode (anode) and an outer electrode (cathode), and is powered by a capacitor bank of 41.6 μ F, 20kV. At a 20kV operating voltage the capacitor bank delivers a maximum current of 600kA with 1.7 μ s quarter period.

Plasma focus operation

Plasma focus is a particular pinch device in which a high voltage is applied to a low pressure gas between two co-axial cylindrical electrodes, generating a short duration high density and high temperature plasma region, on axis at the end of the electrodes. This device is also a rich source of different types of radiation. It was considered as one of the most promising machines for achieving controlled nuclear fusion. The basic working principle of this device is first, to convert the stored electrical energy in the capacitor to magnetic energy that appears in the plasma focus tube and then to convert a part of the magnetic energy into the plasma energy. The plasma focus is operated with the inner electrode as the anode and the outer electrode as the cathode. When a high voltage pulse is applied between the two coaxial electrodes of the plasma focus device filled with an appropriate pressure of the working

gas, a high electric field is developed across the insulator. Initially, the gas breakdown occurs across the insulator sleeve surface and current sheath is developed within a fraction of a microsecond. The self-generated magnetic field detaches the current sheath from the insulator sleeve surface and accelerates it to the end of the central anode. Plasma collapsed for not stable and then X-ray and the ion beam was generated.

3. Result and discussion

3.1. System optimization--effect of nitrogen pressure

In this experiment, we measure the ion current density with different gas pressure. The anode is made of Al, and a bias ion collector (BIC) is set in front of the anode with the distance of 200mm, and a rogowski coil is set around the anode to measure the current discharge.

The fig. 2 shows the wave of discharge current and the ion current density, which is measured by rogowski coil and BIC. The discharge current reaches the max of 600 kA in 1.6 μ s and then have a dip to about 500 kA with 400ns. At the same time, the wave of BIC reaches the peak of 1.4 kA/cm² and the width of pulse τ = 200 ns.

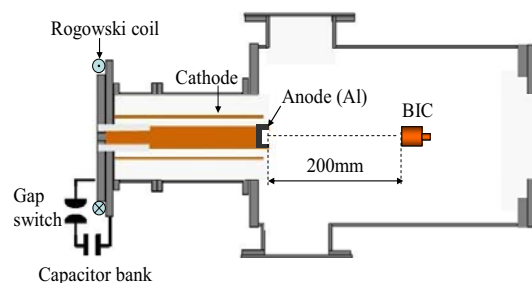


Fig. 1 Experiment set up for ion current density measure

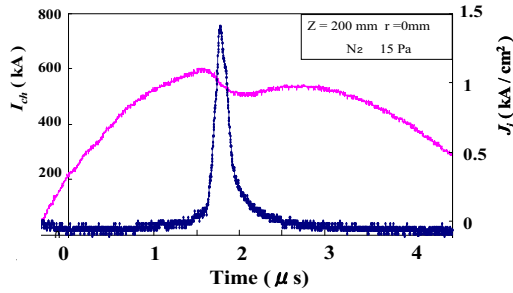


Fig.2 Discharge current and ion current density

With this method, we got the Ion current density with different gas pressure as fig.3. The average of current density were 1.1 kA/cm² when the gas pressure was 10 Pa and 1.7kA/cm² with 15Pa, 1.2kA/cm² with 20Pa, and 0.8kA/cm² with 25Pa. It shows the current density got the max when the gas pressure was 15 Pa.

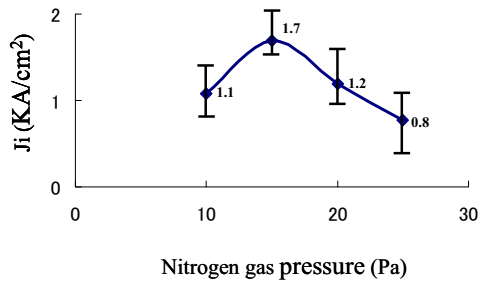


Fig.3 Ion current density with different gas pressure

Ion beam energy measurement: Time of Flight (TOF)

We can measure different ion beam energy in the different position, with the method of TOF. We can get the speed of ion beam peak, and the ion beam energy. The two BIC were set in the front of the anode with the distance of axis direction $z = 300$ mm, diameter direction $r = -30$

mm and another one with the distance of $z = 230$ mm, diameter direction $r = 30$ mm. Chamber pressure was pumped up to 5×10^{-3} Pa, and then inlet the nitrogen gas with 15 Pa to get a focus shot.

Figure 4 shows the ion current density at the two different points. From the figure, the time difference was shown about 64 ns. Then the nitrogen ion beam speed was about 1.1×10^5 m/s. And the ion beam energy was up to 176KeV.

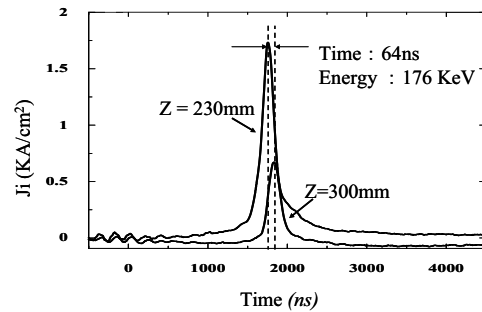


Fig. 4 Ion current density with T.O.F.

Figure 5 shows Ion beam energy in different gas pressure, with the increase of gas pressure the ion current density increased, and when the gas pressure at 15pa, it got a maximum value, and then decreased with the increase gas pressure.

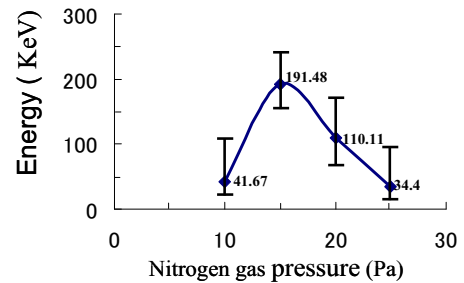


Fig.5 Ion beam energy in different gas pressure

3.2. Experiment of Al surface modification

Pure Al (99.99%), mechanically polished and ultrasonically cleaned was used as Modification target at the at 0° 5° 10° 15° angular position for focus shots 3 with the gas pressure of 15Pa.

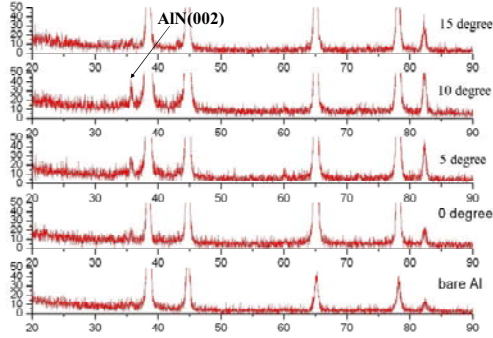


Fig. 6 XRD patterns of Al substrates at different angular positions

The XRD patterns of the thin films deposited at 0° 5° 10° 15° angular position for focus shots 3 are shown in Fig. 2. The new peaks at angles $2\theta=26^\circ$ are assigned to the AlN $\langle 2\ 0\ 0 \rangle$ phase, The XRD peaks identified for the AlN phase at the angular position of 0° , 5° , 10° , 15° for 3 deposition focus shots. These shifts show that an increase d values from angular position of 0° to 10° , however has a decrease in d values to angular position of 15° for the AlN phase. The reason for this decrease in d value for AlN phase is that a decrease Ion current density with the increase of angular, and at the low angular position, the Al ion density is much higher the nitrogen ion density. It is difficult to combine into AlN phase.

4. Conclusion

All of the above results show that a Mather

type plasma focus device, energized by a 20 kV capacitor, is a good technique for surface modification. And the optimum condition for nitrogen ion formation was found to be 15Pa. The XRD patterns of the substrates show that the peaks at angles $2\theta=26^\circ$ are assigned to the AlN $\langle 2\ 0\ 0 \rangle$ phase.

References

- [1] M. M. M. Bilek, K. N. Mc Gee, The Role of Energetic Ions from Plasma in the Creation of Nanostructured Materials and Stable Polymer Surface Treatments, *Nuc Instr. Methods Phys. Res. B* 242(2006)
- [2] H.R. Khan and H. Frey, Ion Beam Deposition of Nanocrystalline and Epitaxial Silicon Films Using Silane Plasma, *Surf. Coat. Technol.* (1999)
- [3] L. Soto, New Trends and Future Perspectives on Plasma focus Research, *Plasma Phys. Control. Fusion*, 47(2005) A 361
- [4] M.P. Srivastava, R. Gupta, *Advanced in Applied Plasma Sci.* 2, 161 (1999).
- [5] Li.Yang, et. al. *Journal of Industrial and Engineering Chemistry* 14, 22 (2008).

Characteristics of an atmospheric pulsed DBD plasma jet and its preliminary application for sterilization

Jia Li^a, Natsuko Sakai^a, Masato Watanabe^a, Eiki Hotta^a and Masaaki Wachi^b

^aDepartment of Energy Sciences, Tokyo Institute of Technology, 4259 Nagatsuta, Midori-ku, Yokohama, 226-8502 Japan

^bDepartment of Bioengineering, Tokyo Institute of Technology, 4259 Nagatsuta, Midori-ku, Yokohama, 226-8502 Japan

A novel plasma jet with a plane-to-plane DBD structure working at atmospheric pressure is developed. This jet is operated at a sub-microsecond pulsed voltage with a repetition rate of 1-10 kHz range. The working gas, helium, is fed into the plasma jet. The electrical property of the discharge has been studied by means of a classical DBD model. By fitting the fine structure of the emission bands of N₂, plasma gas is found to be cooled to be near room temperature (~ 300 K) at the position of 15 mm away from the jet nozzle exit, which is also verified by a thermocouple. Based on the analysis of the H_β Stark broadening, the electron density inside the plasma jet nozzle is evaluated to be in the order of 10¹⁴ cm⁻³. Finally, the feasibility of disinfecting E.coli cells was confirmed preliminarily.

Keyword: dielectric barrier discharge, plasma jet generation, gas temperature, electron density, sterilization

I. INTRODUCTION

Recently, non-thermal atmospheric pressure plasma jets operated at atmospheric pressure have been attracting significant attention due to some marked merits, such as without expensive vacuum units and promising potentials in a variety of applications like thermally sensitive materials treatment [1-3]. Especially, the biomedical applications using such plasma jets have become hot issues. To extend the plasma treatment to living tissue, one of the prerequisites is that the jet should be near the room temperature and carries a low current under moderate voltage. Moreover, at the point of applications, it is necessary to attain high plasma stability while maintaining efficient reaction chemistry.

The atmospheric pressure plasma jet can be realized in various configurations utilizing different types of excitation from DC to microwave frequency. Usually, their generation relies on several mechanisms: capacitively coupled discharge (CCP), corona discharge, and dielectric barrier discharge (DBD) [4-7]. Among them, the major advantage of DBD configuration is to effectively prevent spark-to-arc transition and hence to stabilize the discharge. Concerning power excitation, recent results by Laroussi M and Lu X [8] have shown that sub-microsecond pulsed voltages at kilohertz frequency can provide a great capability to control the plasma jet ignition and to reduce the gas temperature.

In this paper, a novel plasma jet with a plane-to-plane DBD structure driven by sub-microsecond pulsed power at atmospheric pressure is developed, whereby stable non-thermal plasma in helium can be generated. The main aim of this study is to understand the plasma characteristics by measuring and analyzing basic plasma parameters such as gas temperature and electron density. Finally, the possibility of bacterial inactivation was investigated preliminarily.

II. EXPERIMENTAL SETUP

Figure 1 shows the schematic illustration of the experimental setup. As shown in Fig.1 (a), it mainly consists of three parts: the plastic case, the main unit where discharges occur and the high voltage (HV) generator. The plastic case works as a pathway for plasma gas as well as fixing the main unit. The main unit, whose detailed structure is shown in Fig.1 (b), has a plane-to-plane DBD structure.

Two parallel glass plates (50×7×1 mm, $\epsilon_r=10$) are inserted into the square opening (7×3 mm) on the plastic case and stabilized by adhesive. They serve as dielectric barrier layers with 1 mm gap spacing. Electrodes are two right-angled copper plates with the longer parts (15×7×1 mm) attached to the surface of these glass plates tightly. The shorter parts are fastened to the plastic case by screws. To prevent the gas leaking from the sides, two parallel glass plates are stuck to the side faces. All the parts of the device are fixed to each other to prevent accidental displacement. The working gas of Helium (99.9%) with a flow rate (f) up to 20 liters per minute (l/min) is injected through the rear hole of plastic case controlled by a mass flow controller and flow out of the nozzle exit.

A homemade sub-microsecond HV pulse generator [9] was used in this work. This unipolar generator employs an inductive energy storage system with an SI Thyristor as a current interrupter. The typical characteristics are: voltage amplitude ~ 20 kV, pulse width ≤ 500 ns and pulse repetition rate (PRR) ~ 10 kHz. A current limiting resistor 2 kΩ is connected in series between the HV pulse generator and plasma jet device.

Once the helium gas is introduced and high voltage is applied, a discharge is fired in the gap between the parallel glass plates. The plasma gas of the discharge is spewed out from the jet nozzle and a plasma plume reaching length of about 3 cm at 4 l/min is ejected to open air, as shown Fig.1 (c). Here, the plasma jet images were recorded by Nikon digital camera D40X with an exposure time of 10 s. Also, the Reynolds number (Re) in such helium plasma jet device can be estimated from $Re = D \cdot v \cdot \rho / \mu$, where v is helium velocity, ρ is helium density (0.164 kg/m³), and μ is helium viscosity (2×10^{-5} kg/m s) at 20 °C and at 1 atm., D is the characteristic length or hole diameter. For rectangular ducts, as in the case of our experimental setup, D is defined as 4 times the cross-sectional area, divided by the wetted perimeter [10] and is calculated to be 1.75 mm. Then Re is calculated to be 136.66, showing the production of helium plasma jet in laminar flow [11].

An optical fiber is positioned radially at 1 cm away from the side face of main unit and can be freely moved along the axis. The optical emission collected by the optical fiber is recorded by two spectrometers: Ocean Optics Maya 2000 for wavelength in the range of 200-800 nm, and a UV-visible MD-25 spectrometer (Japan Spectroscopic Co.) with

a linear CCD multi-channel detector. The latter has a grating of 1800 g/mm and slit width of 100 μm and is used to measure the spectrum of $\text{N}_2 \text{ C}^3\Pi_u \rightarrow \text{B}^3\Pi_g$ (372-382.5 nm), $\text{N}_2^+ \text{ B}^2\Sigma_u^+ \rightarrow \text{X}^2\Sigma_g^+$ (387-392 nm) and H_β line.

III. RESULTS AND DISCUSSION

A. Electrical characteristic of the plasma

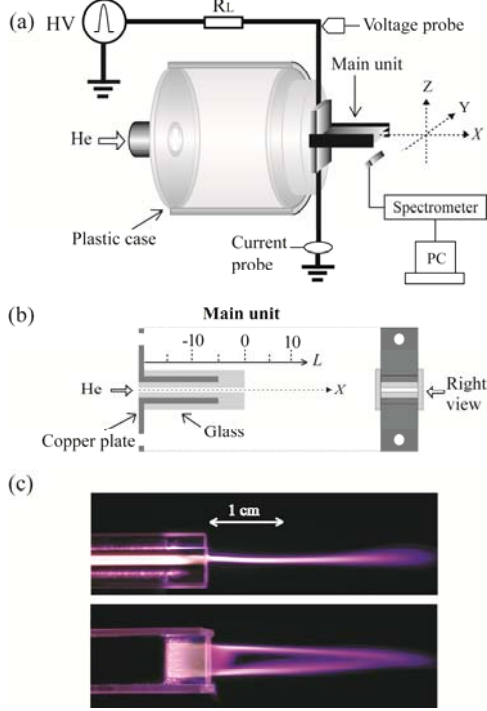


Figure 1. Schematic of the experimental setup. (a) DBD plasma jet (X , Y and Z are axes of rectangular coordinates.). (b) Detailed structure of main unit (L : axial position in mm). (c) Photographs of the He plasma plume in both Y and Z viewing directions under the conditions of $V_d = 13$ kV, PRR = 5 kHz and $f = 4$ l/min.

Employing a rather classical model, the equivalent circuit of our set-up is given in Fig.2. The DBD reactor, i.e. the main unit, is modeled by a capacitor C_d representing the solid dielectric connected in series with the gas gap. The latter is the parallel combination of a C_g capacitor and a R_p resistor, corresponding to the pure gas capacitance and the plasma resistance, respectively. Parallel to the DBD reactor, there is a C_c representing all the parasitic capacitances that can be deduced from measurements when plasma is off. A fictitious switch S is drawn on the circuit to denote that plasma occurs intermittently. The measured applied voltage and overall current flowing in the circuit are noted as $V_d(t)$ and $i_{total}(t)$, respectively. It is noted that $i_{total}(t)$ includes both a displacement $i_{dis}(t)$ and conduction components $i_z(t)$. Applying circuit theory to this equivalent circuit, basic electrical properties of the DBD plasma can be deduced, as shown in the following equations (S switch being on) [19]:

$$i_z(t) = \left(1 + \frac{C_g}{C_d}\right) i_{total}(t) - C_g \frac{dV_d(t)}{dt} \quad (1)$$

$$V_g(t) = V_d(t) - V_m(t) = V_d(t) - \frac{1}{C_d} \int_{t_0}^t i_{total}(\tau) d\tau \quad (2)$$

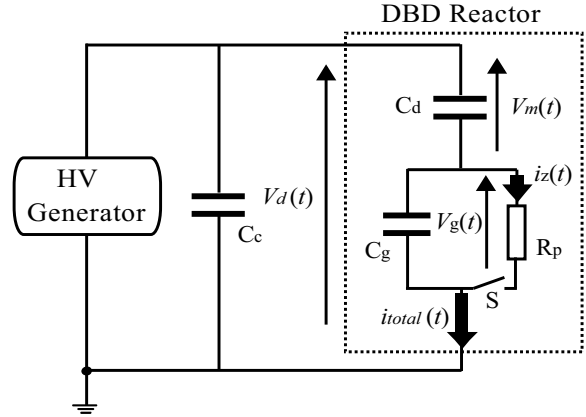


Figure 2. Equivalent electrical circuit.

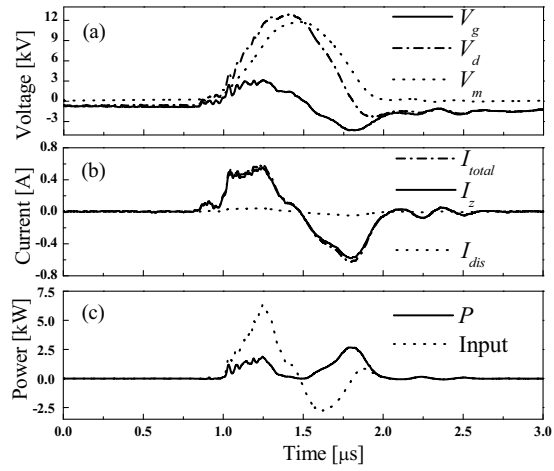


Figure 3. Voltage, current and power waveforms for the He plasma jet under the conditions of $V_d = 13$ kV, PRR = 10 kHz and $f = 2$ l/min.

$$P(t) = V_g(t) i_z(t) \quad (3)$$

where $P(t)$ is plasma power. For the electrical study, a program was made to solve numerically the above equations, where the experimentally obtained $V_d(t)$ and $i_{total}(t)$ waveform data are fed as input variables. For numerical stability reasons the experimental signals are fitted by means of cubic interpolating polynomials. Results are shown in Fig.3. It can be seen that though the applied voltage is unipolar pulse, the current appears bipolar and has both positive and negative pulses, indicating that two discharges started in the rising and falling phase of the applied pulse, respectively. Fig.3 (b) shows that initially the gap voltage V_g increases following the applied voltage V_d . Then, as the discharge onset voltage is attained, the positive conduction current pulse occurs. This charges the dielectric, i.e., V_m increases, as shown in Fig.3 (a), and induces a significant drop in V_g resulting in the positive discharge extinction. Next, during the falling flank of V_d , the already charged dielectric induces a significant negative gap voltage which is sufficient to ignite a negative discharge. It is noteworthy that, as shown in Fig.3 (c), during the negative discharge, some power stored during the primary discharge in the circuit's capacitive elements is actually returned to the HV generator [12-13].

B. Plasma emission

To investigate what kinds of excited species presented in the plasma, the aforementioned spectrometer (Maya 2000) is used to measure the optical emission of plasma plume. All spectral plots are the result of 5 data acquisitions. Spectral species identification, labeling and relative intensity measurements were done by using the Spectrum Analyzer (version 1.7) software [14].

A typical emission spectrum of the helium plasma in the range of 200-800 nm obtained at the nozzle exit ($L = 0$ mm) is shown in Fig. 4. It shows that there are strong nitrogen molecular lines as well as a few helium and oxygen atomic lines. The strongest emission is the excited He atom line at 706.5 nm, and N_2 ($C^3\Pi_u \rightarrow B^3\Pi_g$) band at 337.1 nm and excited oxygen line ($3p^5P \rightarrow 3s^5S$) at 777.3 nm are shown.

Oxygen and nitrogen species arise because the plasma is ejected into the ambient air where its energetic electrons and He metastables ionize and excite air molecules. The N_2^+ line at 391.4 nm is attributed to Penning ionization and charge transfer [15] followed by direct electron-impact excitation. Atomic oxygen is generally generated by a dissociative collision between an oxygen molecule and an electron. Atomic oxygen may also be generated though Penning ionization [16]. Moreover, the emission band of the OH radical at 308.9 nm is shown in the spectrum. The OH radicals represent the result of the dissociation of H_2O molecules from the humid back-diffused air caused by collisions with accelerated electrons or with long-lived species present in the plasma, especially helium metastables [17].

To observe qualitatively the behavior of the plasma species along the axial direction, we selected four representative lines: He – 706.5 nm as plasma gas, N_2 – 337.1 nm as the dominant component of the diffusing air, O – 777.4 nm as species crucial for biomedical treatment and N_2^+ – 391.4 nm as an indicator of helium metastable presence.

Figure 5 portrays the peak intensity of selected emission line as a function of axial position L . For better distinction, the emission intensity of the species other than He is normalized to 1/5 of the peak intensity of He 706.5 nm line. As can be seen, the He 706.5 nm decays as soon as the plasma plume propagates out of the discharge zone between parallel electrodes ($L \geq -5$ mm). The reason may be due to its high excitation energy (23.07 eV) and thus sensitive to the intensity of electric field. The emissions of the air originating species (N_2^+ , O) present peaks at the same position, the nozzle exit (i.e. $L = 0$ mm). This is the place corresponding to the most favorable combination between the electric field strength and the back-diffusion of air into the plasma column to excite the species. Inside the jet nozzle, although the electric field is very intense, the back-diffusion of air is low, and away from the jet nozzle the back-diffusion of air is high while the electric field strength decreases. The N_2 337.1 nm line increases slowly and reaches its maximum at about 5 mm away from the nozzle exit. This may be explained as follows. The threshold energy of N_2 ($C^3\Pi_u$) state is much lower than that of N_2^+ ($B^2\Sigma_u^+$) and O ($3p^5P$). Therefore, N_2 ($C^3\Pi_u$) state can still be generated through various processes such as step excitation and pooling reaction ($2N_2$ ($A^3\Sigma_u^+$) \rightarrow N_2 ($C^3\Pi_u$) + N_2 ($X^1\Sigma_g^+$)) [18]. This process was found to be the dominant production mechanism of the C-state in the afterglow of He/ N_2 plasmas in DBD at atmospheric pressure [19].

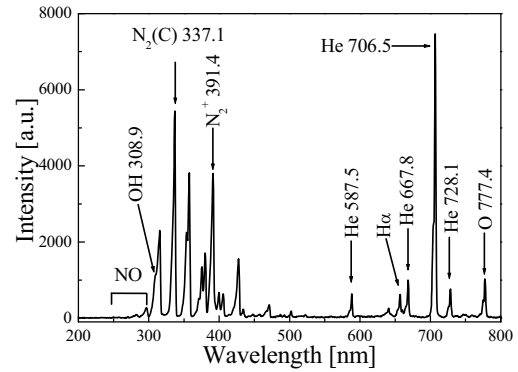


Figure 4. Emission spectra at the axial position $L=0$ mm under the conditions of $V_d = 13$ kV, PRR = 10 kHz and $f = 2$ l/min.

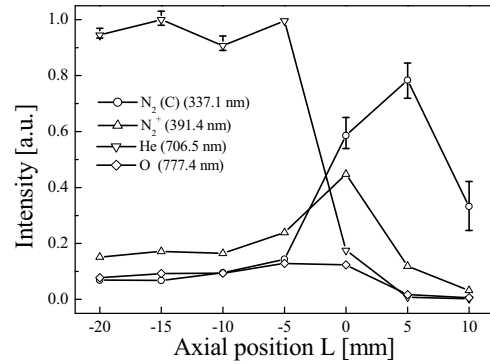


Figure 5. Dependence of selected N_2 (C), N_2^+ , He and O atom normalized line intensities on the axial position L . Experimental conditions are same as that of Fig.4.

C. Excitation temperature and Gas temperature

To have a further insight into the plasma characteristics, the excitation temperature is obtained provided that the population in the levels of atom follows the Boltzmann distribution for plasma in the local thermodynamic equilibrium. Based on the optical emission spectrum shown in Fig.4, the characteristic spectral lines 587.56, 667.82, 706.5, and 728.13 of He atoms are chosen for approximation. After calculation, the T_{exc} is found to be around 1123 K.

Gas temperature T_g is another important parameter to evaluate non-thermal plasma behavior and some parameters, like electron density, are dependent on T_g . Also, it is quite important when plasmas are to be applied to biomedical processing. Generally, T_g increases with applied voltage and pulse repetition rate while decreases with flow rate.

For non-thermal plasma, T_g can be usually deduced from the rotational temperature T_r of diatomic species, such as N_2 , N_2^+ and OH. The rotational temperature describes the population of the rotational levels in molecular species. The distribution, unlike that of vibrational levels, is not given by a pure Boltzmann distribution. Each rotational level has a different statistical weight due to the $(2J+1)$ -fold degeneracy of the states, where J is the total angular momentum of the molecule. Therefore, the thermal distribution of the rotational states will be given by the product of the Boltzmann factor $\exp(-E/kT)$ times the statistical weight $(2J+1)$ [20]. For most species it can be assumed that T_r is

close to the translational temperature T_t and is effectively considered to be T_g of the mixture because rotational-to-translational relaxation is fast at atmospheric pressure [15, 21, 22, 23]. Since the MD-25 spectrometer used in this paper does not resolve the rotational structure, in order to calculate the rotational temperature, we have fitted the experimental data with a theoretical calculation that takes into account the instrumental line broadening of the spectrometer.

In this work, to determine the gas temperature, the MD-25 spectrometer was used to measure the emission of N_2 $C^3\Pi_u \rightarrow B^3\Pi_g$ ($\Delta v = -2$) band at the position $L = 15$ mm and then the Specair program [22, 24] was used to generate the simulated spectra and for comparison, both experimental and simulated spectra were normalized. A least-square procedure was made to obtain the best fit, which gives the rotational temperature. A typical fitting of the measured band spectrum with the simulated one is shown in Fig.6. By this way, it is found that gas temperature is already cooled to be around room temperature (300 K) at the position 15 mm away from the nozzle outlet. The gas temperature obtained from this method is in good agreement with the value (301.75 ± 0.8 K) measured by the thermocouple (CIE 305P) with a nominal error of 0.1°C . By applying the same method to simulate the emission of N_2^+ ($B^2\Sigma_u^+ \rightarrow X^2\Sigma_g^+$) band,

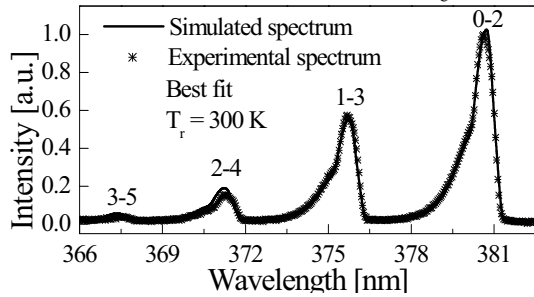


Figure 6. Experimental and simulated best-fit spectra of N_2 ($C^3\Pi_u \rightarrow B^3\Pi_g$) at $L = 15$ mm. Experimental conditions are: $V_d = 13$ kV, PRR = 10 kHz, $f = 2$ l/min.

the gas temperature inside the plasma jet was determined to be in the range of 360 ~ 400 K. These results will be used to calculate electron density in the next section.

D. Electron density

The spectral method for obtaining the electron density is based on the analysis of the profile broadening of the 486.13 nm H_β line. Compared to other hydrogen Balmer lines, the H_β line is often preferred because it has adequate emission intensity, higher sensitivity to electron density and lower susceptibility to self-absorption [25]. Besides the Stark broadening, the H_β line emitted from plasma (usually mixed with a little H_2) can be broadened by other mechanisms and the total broadening of the line profile is due to the combined contribution of all effects. Each broadening mechanism is independent and plays a different role on broadening the line depending on the plasma conditions. Under the experimental conditions of this work (1 atm, $T_g \sim 360$ -400K), the only relevant sources of broadening are the Stark broadening, the van der Waals broadening, the Doppler broadening and the instrumental broadening. Other less important effects such as resonance broadening can be ignored due to the small amount of H_2 addition.

The total H_β lineshape can be approximated with a Voigt function, resulting from a convolution of Gaussian and Lorentzian profiles. The full-width at half maximum

(FWHM) of both the Gaussian and Lorentzian components, $\Delta\lambda_G$ and $\Delta\lambda_L$, are given in Eq. (4) and (5), respectively

$$\Delta\lambda_G = \sqrt{\Delta\lambda_{Doppler}^2 + \Delta\lambda_{Instrument}^2} \quad (4)$$

$$\Delta\lambda_L = \Delta\lambda_{Van\ der\ Waals} + \Delta\lambda_{Stark} \quad (5)$$

where $\Delta\lambda_{Doppler}$, $\Delta\lambda_{Instrument}$, $\Delta\lambda_{Van\ der\ Waals}$ and $\Delta\lambda_{Stark}$ are the FWHM of Doppler, instrumental, Van der Waals and Stark broadening, respectively. The part of the line broadening corresponding only to the Stark broadening can be obtained from the total broadened profile.

During the experiment, a small amount of H_2 (0.02 mol%) was added into the He gas flow and the emission emitted from plasma was recorded. The instrumental broadening was calibrated with the He-Ne laser (5 mW) on steady glow 632.8 nm, using the same experimental set-up (1800 grooves/mm gratings) and was found to be a Gaussian of FWHM 0.359 nm. Doppler broadening is due to the thermal motion of excited hydrogen atoms and is determined from the gas temperature T_g by the expression of its FWHM

$$\Delta\lambda_{Doppler} = 7.16 \times 10^{-7} \lambda_0 \left(\frac{T_g}{M} \right)^{0.5} \quad (6)$$

where λ_0 is the emission wavelength in nm and M is the atomic weight of H atoms in g mol^{-1} . Van der Waals broadening is caused by collisions of excited H atoms (the emitters) with ground state He atoms (the perturbers). According to [21], the value of $\Delta\lambda_{Van\ der\ Waals}$ was estimated by formula

$$\Delta\lambda_{Van\ der\ Waals} \approx 4.09 \times 10^{-13} \lambda_0^2 (\alpha R^2)^{2/5} \left(\frac{T_g}{\mu} \right)^{3/10} n_{He} \quad (7)$$

where α is the average polarizability of He, given in cm^3 , and is equal to $1.38 \times a_0^3$ (a_0 is the Bohr radius in cm), the parameter $R^2 \approx 600 \times a_0^2 \text{ cm}^2$ is determined from the ionization energy of H and the upper and lower energy levels of the H_β , $\mu = 0.8$ is the emitter-perturber reduced mass, and n_{He} is the neutral He gas density in cm^{-3} . Stark broadening arises from the interaction between charged particles and excited H atoms, and the FWHM of Stark broadening is related to the electron density by [26]

$$\Delta\lambda_{Stark} \text{ (nm)} = 2 \times 10^{-11} (n_e)^{2/3} \quad (8)$$

where n_e is the electron density in cm^{-3} . The electron temperature is not considered since the electron density depends scarcely on the electron temperature for the H_β line.

The recorded H_β spectral profile was normalized to its area and then fitted to a Voigt function according to the Maquardt-Levenberg method. $\Delta\lambda_G$, calculated from equation (4), was kept constant at a given gas temperature. $\Delta\lambda_L$ was obtained from the best fit between the simulated Voigt profile and the experimental spectrum. Then, the Stark contribution, $\Delta\lambda_{Stark}$, was found from equation (5). A typical fitting is shown in Fig.7, where $n_e = 1.52 \times 10^{14} \text{ cm}^{-3}$ is obtained from $\Delta\lambda_{Stark} = 0.0571$ nm.

By this way, the effects of peak applied voltage, pulse repetition rate, flow rate and axial position on electron density are investigated. Results are shown in Fig.8. Electron density increases almost linearly with the pulse repetition rate and applied voltage, as shown in Fig.8 (a). With the increase of pulse repetition rate or applied voltage, electrons can gain more energy and cause more ionization collisions. On the other hand, from Fig.8 (b), it can be seen

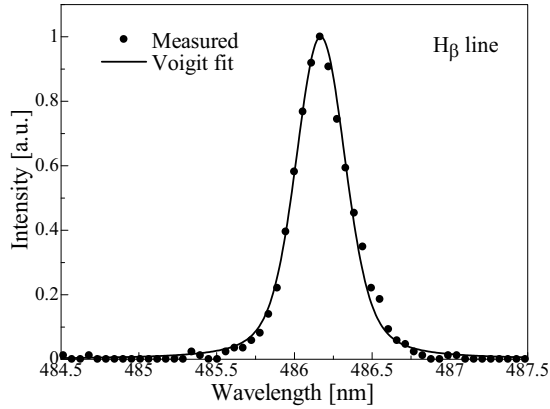


Figure 7. A typical line profile of H_{β} line at the position of $L = -10$ mm under the conditions of $V_d = 8$ kV, PRR = 10 kHz and $f = 2$ l/min. $\Delta\lambda_{\text{Stark}} = 0.0571$ nm and electron density $n_e = 1.52 \times 10^{14} \text{ cm}^{-3}$.

that electron density varies inversely with the He gas flow rate. A same behavior was also found in Ar plasma jet [26]. With the increased flow rates, the gas velocity increases and the residence time of the gas in the electrode gap decreases. Consequently, the electron density becomes lower.

Figure 8 (c) reveals the electron density as a function of axial position. The pulse repetition rate was set to be 5 and 10 kHz under the conditions of 13 kV and 2 l/min. As shown in Fig.8 (c), the electron density rapidly decreases as the position is approaching the nozzle exit, due to recombination and attachment. At the position of the nozzle exit, the electron density has been 3–4 times less than that in the center of jet nozzle. Electron density away from the nozzle exit could not be determined due to the limitation of the spectrometer used here; it is reasonable to estimate that the electron density in the plasma plume should be lower, probably in the order of 10^{13} cm^{-3} . However, its confirmation needs further investigations.

E. Sterilization experiment

To confirm the feasibility of disinfecting micro-organisms, we employed the *E.coli* bacterial cells as a model micro-organism. The plasma jet was directed to the center of the Petri dish perpendicularly to its surface. The distance between surface of agar and outlet edge of plasma nozzle was 2 cm. The operational conditions were set to be $f = 2$ l/min, PRR = 5 kHz and $V_d = 13$ kV. Figure 9 presents photos of Petri dishes of 90 mm diameter, showing the distribution of bacteria population of *E. coli* on agar. It was taken after incubation over 24 h at 37 °C. Before incubation, *E. coli* was treated with plasma jet under exposure time of 4 and 8 min, respectively. By contrast with untreated culture medium growing *E.coli*, the inactivation effect is clearly seen.

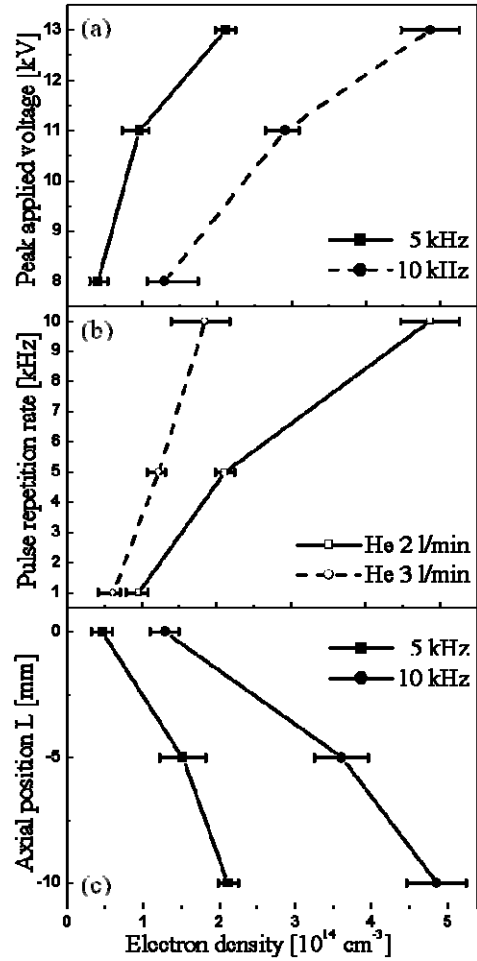


Figure 8. (a) The variation in the electron density with peak applied voltage at different pulse repetition rate. Experimental condition: $f = 2$ l/min; (b) The variation in the electron density with pulse repetition rate at serial of He gas flow rate of 2 and 3 l/min. Experimental condition: $V_d = 13$ kV; (c) The variation in the electron density with axial position at different pulse repetition rate. Experimental condition: $f = 2$ l/min and $V_d = 13$ kV.

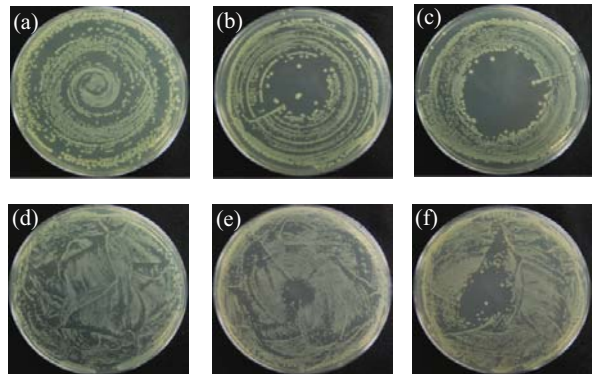


Figure 9. *E.coli* growth represented in terms of CFUs on agar plates, where (a) and (d) control without plasma treatment, (b) and (e) treated with 4 min and (c) and (f) treated with 8 min. CFU: (a) - (c) 5×10^3 (d)-(f) 5×10^4 .

IV. SUMMARY

A novel plasma jet with a plane-to-plane DBD structure working at atmospheric pressure is developed to create non-thermal plasma. This jet is operated at a pulsed voltage, produced by a homemade sub-microsecond pulsed power generator, with a repetition rate of 1-10 kHz range. The working gas, helium for the moment, is fed into the plasma jet. The electrical property of the discharge has been studied by means of a classical DBD model. By fitting the fine structure of the emission bands of N_2^+ and N_2 , plasma gas is found to be heated inside the jet nozzle up to ~ 400 K but is cooled during transport from the nozzle exit. At the position of 15 mm away from the jet nozzle exit, the gas has been cooled to be near room temperature (~ 300 K), which is also verified by a thermocouple. The electron density is evaluated from the analysis of the Stark broadening of $H\beta$ emission and found to be in the order of 10^{14} cm^{-3} inside the plasma jet nozzle. It is shown that the electron density increases almost linearly with the applied voltage and pulse repetition rate while decays rapidly as plasma moves towards the nozzle exit. Finally, preliminary results show that this jet has potential in bacterial inactivation.

REFERENCES

- [1] F. Iza, G. J. Kim, S. M. Lee, J. K. Lee, J. L. Walsh, Y. T. Zhang and M. G. Kong: "Microplasmas: Sources, particle kinetics, and biomedical applications", *Plasma Processes Polym.*, Vol.5, No.4, pp.322-344 (2008)
- [2] M. Laroussi and T. Akan, "Arc-Free Atmospheric Pressure Cold Plasma Jets: A Review", *Plasma Processes Polym.*, Vol.4, No.9, pp.777-788 (2007)
- [3] X. Zhang, M. Li, R. Zhou, K. Feng, and S. Yang: "Ablation of liver cancer cells *in vitro* by a plasma needle", *Appl. Phys. Lett.*, Vol.93, No.2, pp. 021502 (2008)
- [4] T. L. Ni, F. Ding, X. D. Zhu, X. H. Wen, and H. Y. Zhou: "Cold microplasma plume produced by a compact and flexible generator at atmospheric pressure", *Appl. Phys. Lett.*, Vol.92, No.2, pp. 241503 (2008)
- [5] H. S. Park, S. J. Kim, H. M. Joh, T. H. Chung, S. H. Bae and S. H. Leem: "Optical and electrical characterization of an atmospheric pressure microplasma jet with a capillary electrode", *Phys. Plasmas*, Vol.17, No.3, pp. 033502 (2010)
- [6] M. Teschke, J. Kedzierski, E. G. Finantu-Dinu, D. Korzec, and J. Engemann: "High-speed photographs of a dielectric barrier atmospheric pressure plasma jet", *IEEE Trans. Plasma Sci.*, Vol.33, No.2, pp. 310-311 (2005)
- [7] A. Fridman, A. Chirokov, and A. Gutsol: "Non-thermal atmospheric pressure discharges", *J. Phys. D: Appl. Phys.*, Vol.38, No.2, pp. R1-R24 (2005)
- [8] Laroussi M and Lu X: "Room-temperature atmospheric pressure plasma plume for biomedical applications", *Appl. Phys. Lett.*, Vol.87, No. 11, pp.113902 (2005)
- [9] J. Li, N.Sakai, M. Watanabe and E. Hotta: "A 10 kHz Sub-microsecond High-voltage Pulse Generator Using SI Thyristor for Micro-plasma Jets Generation", *IEEJ Trans.FM*, Vol.130, No.6, pp.573-578 (2010)
- [10] http://en.wikipedia.org/wiki/Reynolds_number
- [11] John F.O'Hanlon: *A User's Guide to Vacuum Technology*, 2nd ed, p. 23, New York: John Wiley (1980)
- [12] E. Panousis, N. Merbahi, F. Clement, A.Ricard, M. Yousfi, L.Papageorghiou, J.F. Loiseau, O.Ficheald, B.Held and N.Spyrou: "Atmospheric Pressure Dielectric Barrier Discharges Under Unipolar and Bipolar HV Excitation in View of Chemical Reactivity in Afterglow Conditions", *IEEE Trans. Plasma Sci.*, Vol. 37, No. 6, pp. 1004-1015 (2009)
- [13] Laroussi M and Lu X: "Power consideration in the pulsed dielectric barrier discharge at atmospheric pressure", *J.Appl. Phys.*, Vol.96, No. 5, pp.3028-3030 (2004)
- [14] Z.Navratil, D. Trunc, R. Smid and L. Lazar: "A software for optical emission spectroscopy-problem formulation and application to plasma diagnostics", *Czech. J. Phys.*, Vol. 56, pp.B944-B951 (2006)
- [15] G.Nersisyan and W. G. Graham: "Characterization of a dielectric barrier discharge operating in an open reactor with flowing helium", *Plasma Sources Sci. Technol.*, Vol. 13, No.4, pp. 582-587 (2004)
- [16] R.Oikari, V. Hayrinen and R. Hernberg: "Influence of N-O chemistry on the radiative emission from a direct current nitrogen plasma jet", *J. Phys. D: Appl. Phys.*, Vol. 35, No.11, pp. 1109-1116 (2002)
- [17] S. D. Anghel, A. Simon and T. Frentiu: "Spectroscopic investigations on a low power atmospheric pressure capacitively coupled helium plasma", *Plasma Sources Sci. Technol.*, Vol. 17, No.4, pp. 045016(2008)
- [18] I. Stefanovic, N.K. Bibinov, A.A. Deryugin, I.P. Vinogradov, A.P. Napartovich and K. Wiesemann: "Kinetics of ozone and nitric oxides in dielectric barrier discharges in O₂/NO_x and N₂/O₂/NO_x mixtures", *Plasma Sources Sci. Technol.*, Vol.10, No. 3, pp. 406-416 (2001)
- [19] N.K. Bibinov, A.A. Fateev and K. Wiesemann: "On the influence of metastable reactions on rotational temperatures in dielectric barrier discharges in He-N₂ mixtures", *J.Phys.D: Appl.Phys.*, Vol.34, No.12, pp.1819-1826 (2001))
- [20] G. Herzberg: *Molecular Spectra and Molecular Structure*, 2nd ed, p. 124, New York: Van Nostrand(1950)
- [21] Q.Wang,I. Koleva, V. M. Donnelly and D. J. Economou: "Spatially resolved diagnostics of an atmospheric pressure direct current helium microplasma", *J. Phys. D: Appl. Phys.*, Vol.38, No.11, pp. 1690-1697(2005)
- [22] D.Staack, B. Farouk, A.F. Gutsol and A.A. Fridman: "Spectroscopic studies and rotational and vibrational temperature measurements of atmospheric pressure normal glow plasma discharges in air", *Plasma Sources Sci. Technol.*, Vol. 15, No.4, pp. 818-827 (2006)
- [23] D. M. Phillips: "Determination of gas temperature from unresolved bands in the spectrum from a nitrogen discharge", *J. Phys. D: Appl. Phys.*, Vol. 9, No.3, pp. 507-521 (1976)
- [24] C.O. Laux, T.G. Spence, C.H. Kruger and R.N. Zare: "Optical diagnostics of atmospheric pressure air plasmas", *Plasma Sources Sci. Technol.*, Vol.12, No., pp.125-138(2003)
- [25] J.M. Luque, M.D. Calzada and M. S'aez: "Experimental research into the influence of ion dynamics when measuring the electron density from the Stark broadening of the H α and H β lines", *J. Phys. B: At. Mol. Opt. Phys.*, Vol.36, No.8, pp.1573-1584 (2003)
- [26] M. Y. Qian, C. S. Ren, D. Z. Wang, J. L. Zhang and G. D. Wei: "Stark broadening measurement of the electron density in an atmospheric pressure argon plasma jet with double-power electrodes", *J.Appl. Phys.*, Vol.107, No. 6, pp.063303 (2010)

Treatment of Zooplankton in Water by Pulsed Power – An Effect of NaHCO₃ Additive for Micro Bubble Production –

Kouhei Satoh¹, Masayuki Onda¹, Shin-ichi Sakai², and Go Imada^{2,3,*}

¹ Graduate School of Engineering, Niigata Institute of Technology, Japan

² Department of Information & Electronics Engineering, Niigata Institute of Technology, Japan

³ Extreme Energy Density Research Institute, Nagaoka University of Technology, Japan

ABSTRACT

Enhancement of inactivation of zooplankton in ballast water is experimentally proved in pulsed power method. A large number of micro bubbles are successfully produced by applying the pulsed power to the water with sodium hydrogen carbonate (NaHCO₃) additive. The diameter and number density of bubbles are estimated to be 25 μm and 20 mm⁻², respectively. Shock wave generated by burst of the bubbles inactivates the larvae of Artemia. We found that 12.5 % of the larvae of Artemia are inactivated by firing 20 shots of the pulsed power exposure, which is 2.6 times as high as that obtained for the water solution without NaHCO₃ additive.

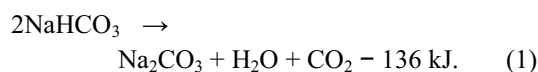
Keyword

Pulsed power, Zooplankton, Ballast water, Micro bubble, Sodium hydrogen carbonate, Additive

1. Introduction

Ballast water is necessary to stabilize ship's hulls during navigation. The total amount of ballast water reaches 3 to 5 billion tons a year, which is transferred internationally. Japan exports approximately 0.3 billion tons of the ballast water a year and imports 0.017 billion. The ballast water includes bacilli, microbes, eggs and larvae of marine organisms, which are undesirably discharged at a port of call. To prevent the migration of these organisms and conserve the marine environment, a international convention for the control and management of ships ballast water and sediments was adopted by the International Maritime Organization in 2004 [1]. It obligates the ships to manage their ballast water by using devices not later than 2006. Many methods for treatment of the ballast water have been studied; such as chemical, heat, sonic, magnetic, biological, radioactive and electrical treatments, however, more methods and techniques are required to develop the feasible devices.

In this study, we propose a new technique on the treatment of the larvae of zooplankton in the ballast water, which uses pulsed-power method [2]. Micro bubbles are produced by applying the pulsed power to the water. Shock wave generated by burst of the bubbles affects the life of the larvae of zooplankton. A large number of bubbles and the bubbles in small diameter are effective for the treatment of the zooplankton. To increase the number of bubbles and decrease the diameter of bubbles, in this study, sodium hydrogen carbonate, NaHCO₃, is added to the water. If some energy is injected to NaHCO₃ in the water, gaseous H₂O and CO₂ are generated as follows.



The reactions (1) and (2) tend to increase the number of bubbles. The solubility in water of NaHCO₃ is 94 g/L at 25 °C. In addition, NaHCO₃ is harmless

* imada@iee.niit.ac.jp

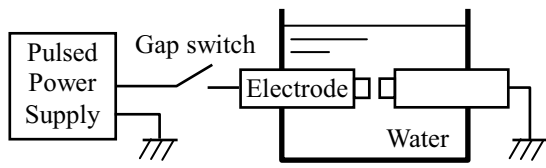


Fig. 1. Experimental setup.

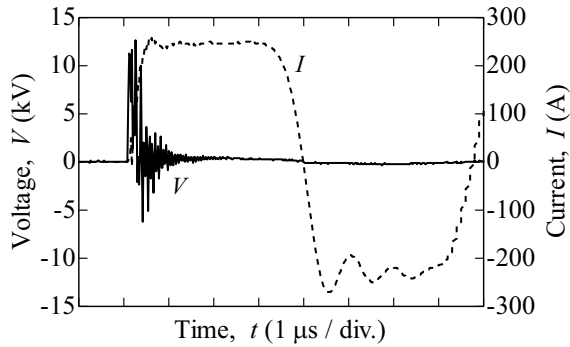


Fig. 2. Typical voltage and current of pulsed power supply into short-circuited load.



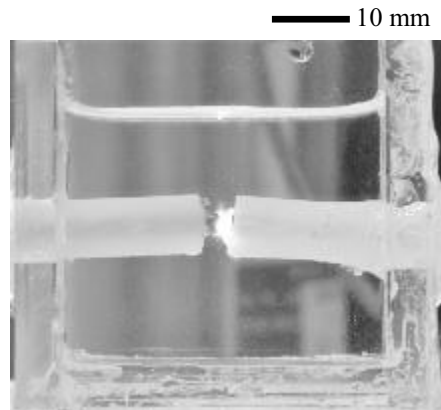
Fig. 3. Example of Artemia larva.

compound used as food additives such as baking soda.

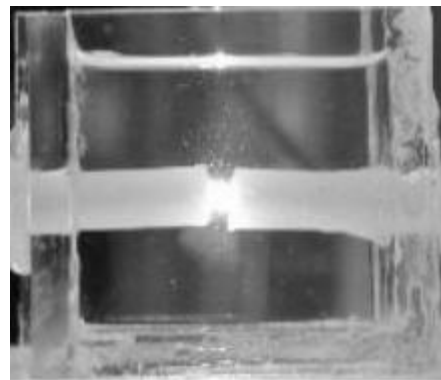
The purpose of this study is to investigate the properties of the bubble production in the water with NaHCO_3 additive. The treatment of the larvae of Artemia is also investigated.

2. Experimental setup

Figure 1 shows the experimental setup. It consists of a pulsed power supply, a gap switch and a water vessel with electrode. The pulsed power supply, pulse forming network ($4000 \text{ pF} - 10 \text{ μH} \times 8$ stages, 3.6 J), generates a rectangular pulsed power with 13 kV , 250 A and 4 μs into short-circuited load (see Fig. 2). This pulse is applied to the electrode through the gap switch. The water vessel is made of clear acrylic-resin sheet with the inner dimensions of $40 \times 40 \times 40 \text{ mm}^3$ and is filled with tap water (21 °C , 310 μS/cm , $\text{pH } 7.1$). The electrode, made of copper,



(a)



(b)

Fig. 4. Light emission from pulsed power exposure. (a) tap water and (b) tap water with 3.8-wt% NaHCO_3 additive.

is located at 15 mm above the bottom of the vessel. Its gap diameter and distance are 2.4 and 0.3 mm , respectively. If the stored energy in the pulsed power supply is consumed to heat the water in the vessel, the water temperature rises to 21.03 °C . The bubbles are photographed through a microscope with back light.

Artemia larvae are added to the water as the zooplankton (see Fig. 3). The Artemia is a species of brine shrimp, which can live in 25-% salt water and its egg has frozen and dry resistance. The larvae of Artemia immediately after the incubation are used in this experiment. These are observed using a microscope. We assume that the Artemia larvae which stop moving in a minute are inactivated because of pulsed power exposure. To accurately determine the inactivation of the zooplankton in the water vessel, the inactivation rate of the Artemia larvae is observed without pulsed power exposure.

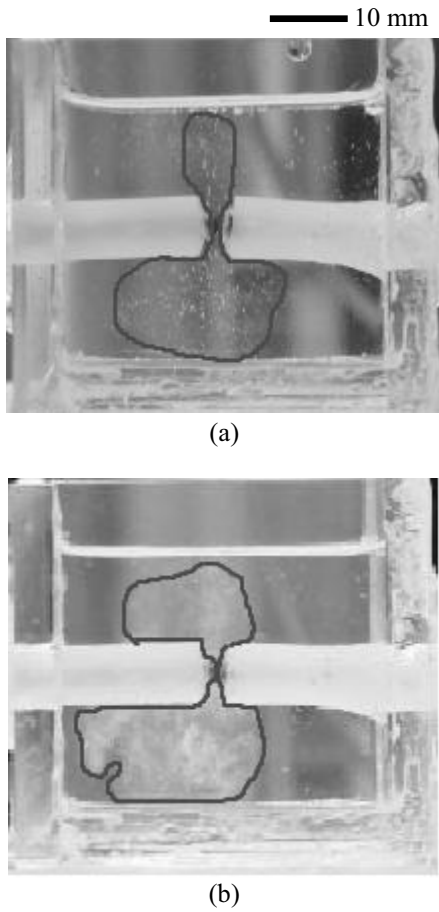


Fig. 5. Production and expansion of bubbles. (a) tap water and (b) tap water with 3.8-wt% NaHCO_3 additive. Solid line indicates extent of bubbles.

The inactivation rate η is defined as

$$\eta = \frac{\text{Number of inactivated Artemia}}{\text{Total number of Artemia}}. \quad (4)$$

The inactivation rates on both the tap water with and without NaHCO_3 additive are in the range of 0 to 5 % without pulsed power exposure.

3. Results and Discussion

3.1 Bubble production by pulsed power in water with NaHCO_3 additive

Figure 4 shows the light emission from the pulsed power exposure. It is taken as a time-integral photograph with the exposure time of 3 s. We find that the light intensity in the tap water with NaHCO_3 additive is more intense than that without NaHCO_3 . It indicates that more energy can be injected into the

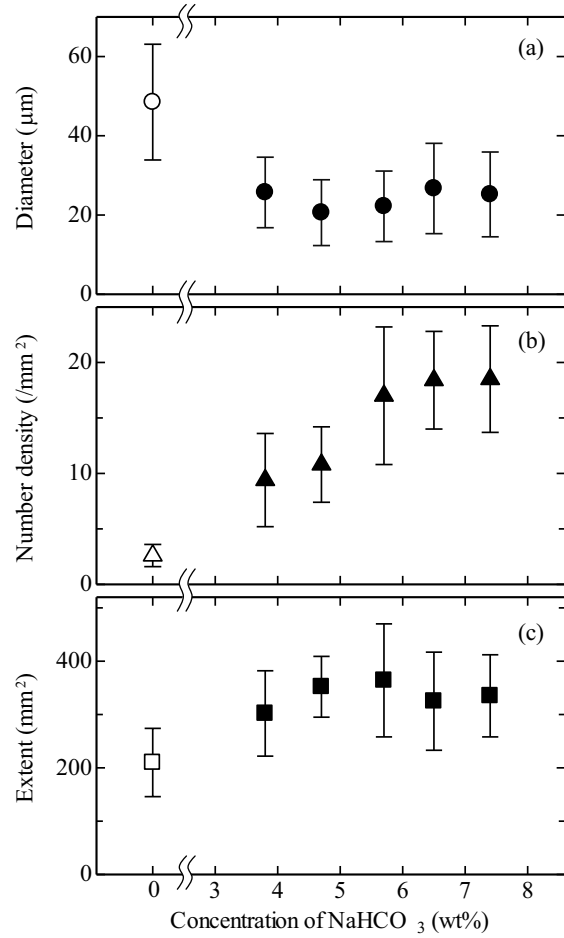


Fig. 6. Diameter (a), number density (b), and extent (c) of bubble as a function of concentration of NaHCO_3 additive in tap water.

water with NaHCO_3 additive and many bubbles will be produced.

Figure 5 shows the photograph of the bubbles produced by the pulsed power exposure. It is taken immediately after the pulsed-power applying with the exposure time of 40 ms. The expansion of bubbles into the water is seen as white fog around the electrode. We define that the sectional area of the fog is the extent of the bubble. It is found that the number of bubbles in the water with NaHCO_3 additive is much more than that without additive. We also find that the bubbles are widespread in the water with NaHCO_3 additive, especially above the electrode.

3.2 Optimum concentration of NaHCO_3 additive in water

Figure 6 shows the diameter, the number density,

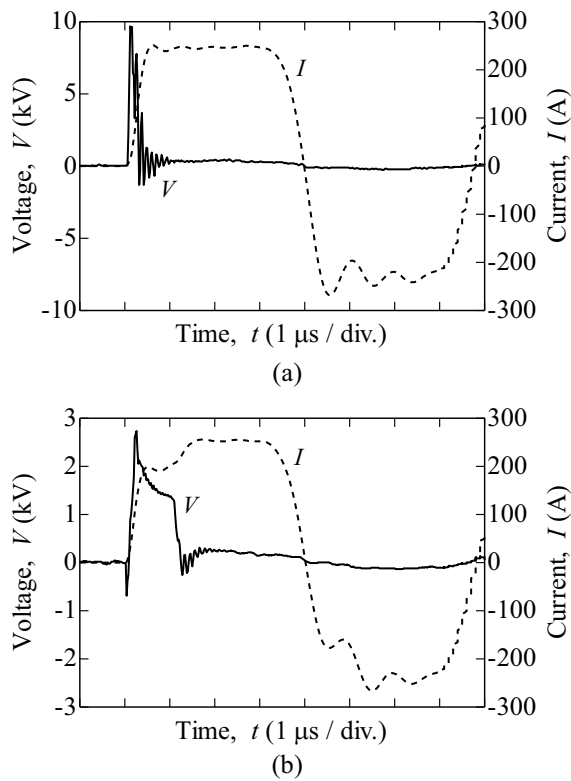


Fig. 7. Voltage and current at electrode. (a) tap water and (b) tap water with 5.7-wt% NaHCO_3 .

and the extent of bubble as a function of concentration of NaHCO_3 additive in the tap water. The diameter of bubble decreases to 20–30 μm in the water with NaHCO_3 additive, which is half of that obtained without the additive. The diameters are almost independent of the concentration of NaHCO_3 additive in our experimental conditions. In comparison with the tap water, moreover, the number density of bubble increases significantly to 18 bubbles/ mm^2 in the high concentration of NaHCO_3 additive. The extent of bubble in the water with the additive is 1.5 times as high as that obtained without the additive.

From the above mentioned results with taking account of less amount of the additive, 5.7-wt% of NaHCO_3 is adopted as an optimum concentration of the additive for the treatment of the larvae of *Artemia*.

3.3 Treatment of larvae of *Artemia*

Figure 7 shows the voltage and current at the electrode in the tap water with and without 5.7-wt%

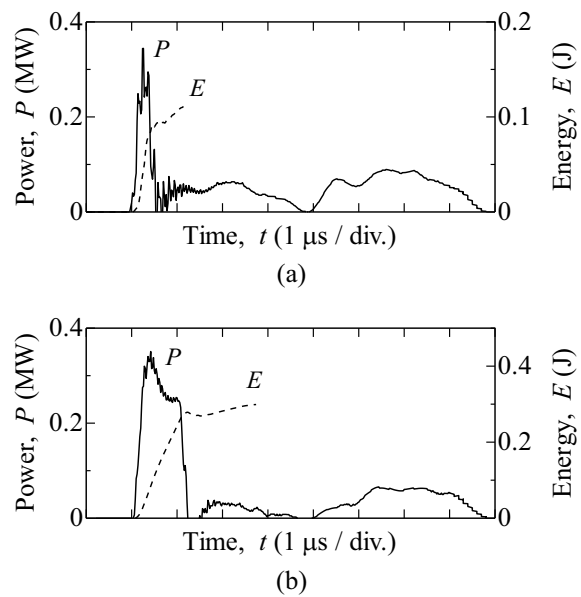


Fig. 8. Power and energy injected into water. (a) tap water and (b) tap water with 5.7-wt% NaHCO_3 .

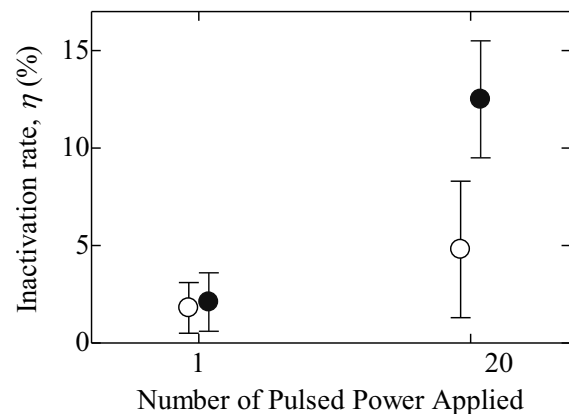


Fig. 9. Inactivation rate of larvae of *Artemia* in tap water (O) and tap water with 5.7wt-% NaHCO_3 (●).

of NaHCO_3 additive. Figure 8 shows the power and energy injected into the water. It is found from Fig. 7(a) that discharge occurs in the tap water with no additive, because the voltage decreases rapidly. The resistance across the electrode is estimated to be lower than 2Ω after the discharge. Hence, the bubble is hardly produced due to an insufficient energy injection into the water. In the water with NaHCO_3 additive, on the other hand, the plateau of voltage is confirmed during $1 \mu\text{s}$, where the resistance and

injected energy are estimated to be 8 Ω and 0.28 J (see Fig. 8(b)), respectively. Since 9.4×10^{-7} mol of NaHCO_3 exists within the gap of the electrode ($2.4 \text{ mm}^{\phi} \times 0.3 \text{ mm}^{\text{W}}$), the maximum applied energy to the NaHCO_3 molecules corresponds to 298 kJ/mol. It indicates that enough energy to decompose the NaHCO_3 molecules is injected and a large number of a H_2O and a CO_2 bubbles are produced in the water (cf. Eq. 1). This much energy injection might cause the decrease in diameter of bubble.

Figure 9 shows the inactivation rate of the larvae of *Artemia* as a function of number of pulsed power applied in the tap water with and without 5.7-wt% of NaHCO_3 additive. Here, around 50 *Artemia* larvae are contained in the water vessel. The pulsed power is applied with 1 s time interval. Although the difference in the inactivation rate between the tap water and the water with NaHCO_3 additive is small at 1 shot of the pulsed power exposure, 12.5 % of the larvae of *Artemia* are inactivated by firing 20 shots of pulsed power exposure in the water with NaHCO_3 additive, which is 2.6 times as high as that obtained for the tap water. The net energy efficiency for inactivation reaches 3.8 million larvae a kWh. It indicates that the larvae of *Artemia* are inactivated by

the shock wave generated by the burst of bubble, because the rise of the water temperature is estimated to be only 0.04 K.

4. Conclusions

A large number of micro bubbles are successfully produced by applying the pulsed power to the water with NaHCO_3 additive. It is found that 12.5 % of the larvae of *Artemia* are inactivated by firing 20 shots of the pulsed power exposure in the water with NaHCO_3 additive, which is 2.6 times as high as that obtained for the tap water.

Acknowledgement

The authors appreciate Assoc. Prof. T. Kikuchi and Mr. H. Kondo of Nagaoka University of Technology for providing the eggs and the counting kit of the *Artemia*.

This work was partly supported by The Uchida Energy Science Promotion Foundation.

References

- [1] GloBallast, <http://globallast.imo.org/> (2011).
- [2] I. V. Lisitsyn et al., "Streamer Discharge Reactor for Water Treatment by Pulsed Power", *Rev. Sci. Instrum.*, **70**, 8, pp.3457-3462 (1999).

Applications of Pulsed Intense Relativistic Electron Beam to Aquatic Conservation

Takashi Kikuchi, Hironobu Kondo, Toru Sasaki,
Hiroshi Moriwaki*, Go Imada****, Nob. Harada

Department of Electrical Engineering, Nagaoka University of Technology, Niigata 940-2188, Japan

**Division of Applied Biology, Faculty of Textile Science and Technology, Shinshu University,
Nagano 386-8567, Japan*

***Department of Information and Electronics Engineering, Niigata Institute of Technology, Niigata
945-1195, Japan*

****Extreme Energy-Density Research Institute, Nagaoka University of Technology, Niigata
940-2188, Japan*

ABSTRACT

In this study, we propose aquatic conservations by using a pulsed intense relativistic electron beam (PIREB). Treatments of introduced species and toxics azo dyes by irradiating PIREB are investigated in this report. Zooplankton contained in water have been inactivated by irradiation of PIREB. A treatment chamber is filled with a solution of 3-wt% salt in water containing Artemia larvae as zooplankton samples, and is irradiated using the PIREB (2 MeV, 0.4 kA, 140 ns). We found that up to 24 % of the Artemia are inactivated by firing 10 shots of PIREB irradiation. It is found that pH changes did not affect to inactivate the Artemia larvae during the time scale of PIREB irradiation. The reaction of congo red, a well-known toxic azo dye, occurred after irradiation by PIREB. An aquation of congo red was irradiated by PIREB (2 MeV, 0.36 kA, 140 ns). After PIREB irradiation, the solution was measured by electrospray ionization-mass spectrometry and liquid chromatography/mass spectrometry. It was found that congo red underwent a reaction (77 % conversion after five shots of PIREB irradiation) and the hydroxylated compounds of the dye were observed as reaction products.

Keywords

pulsed intense relativistic electron beam (PIREB), ballast water, pulsed power, zooplankton, ocean ecosystem, azo dyes, congo red

1. Introduction

A pulsed intense relativistic electron beam (PIREB) has been applied as a technology for environmental cleanup. For example, multi-shot PIREB irradiation reportedly decreased the NO_x concentration in a chamber, treated the volatile organic compounds contained in soil [1]. PIREBs

have great potential for various treatment effects because they not only provide electrons with high kinetic energy but also generate radicals and X-ray emission. The safety of water supplies and aquatic conservation are pressing problems. Therefore, it is important to develop technologies for the decomposition of the pollutants in water; various

water cleanup techniques have received much attention [2].

In comparison with the treatment method using a DC electron beam, the PIREB method has the advantage of offering brief treatments because the beam current is on the order of kA with short pulse duration.

In this study, we propose the aquatic conservation by using PIREB irradiation. Treatments of introduced species and toxics azo dyes by irradiating PIREB are investigated in this report.

2. Inactivation of Zooplankton by Irradiation with Pulsed Intense Relativistic Electron Beam

Ships such as cargo ships use ballast water to stabilize their hulls during navigation. The ballast water is carried around the world and is dumped at a port of call, causing an undesirable propagation of microbes, bacilli and eggs and larvae of marine organisms and the growth of marine plankton in ocean ecosystems. To conserve the ocean environment, a convention was adopted by the International Maritime Organization in 2004 [3]. It specifies that ships must manage their ballast water by using devices such as a ballast water treatment device, not later than 2016 [3].

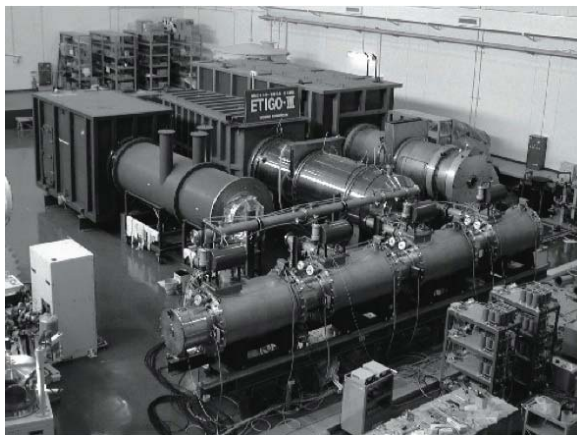


Fig.1 PIREB generator ETIGO-III at Extreme Energy-Density Research Institute, Nagaoka University of Technology

In this study, we propose a new method of

treatment, which uses irradiation by PIREB [4]. In this method, chemicals and/or additives are unnecessary for treatment. The purpose of this paper is to investigate the properties of PIREB injection into ballast water and the effects of irradiation by the PIREB on zooplankton

The PIREB with a kinetic energy of up to 2 MeV is generated using a field-emission foilless electron-beam diode, in which a hollow cathode and a ring anode are set at the first acceleration cell of the pulsed power generator ETIGO-III [5] as shown in Fig.1. The diode gap is vacuumed to 0.02 Pa.

Figure 2 shows a side view of the treatment chamber for PIREB irradiation. The chamber was made of a polypropylene pipe with an inner diameter of 110 mm, a length of 86 mm, and a capacity of 0.8 L, where an end flange of the chamber was floated from the ground. The chamber was separated from the vacuum part of the electron-beam diode by an air bulkhead and was filled with a 3-wt% salt solution as ballast water. The salt solution was made from distilled water and common salt. Artemia larvae were added to the salt solution as zooplankton.

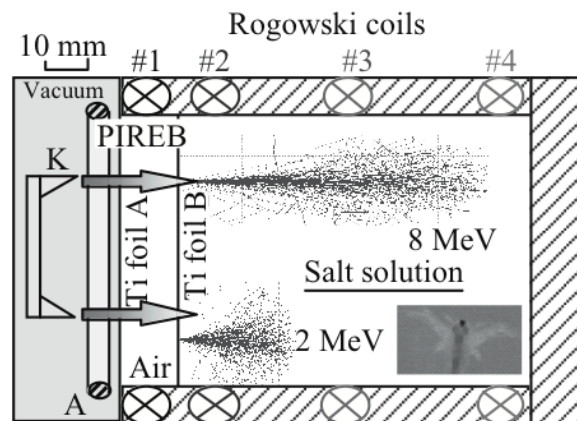


Fig.2 Side view of treatment chamber. Calculated electron trajectories are also indicated

Figure 2 also shows the measurement setup for the PIREB. The irradiated and injected PIREB current in the salt solution was measured with Rogowski coils placed at the inlet (#1), front (#2), middle (#3), and end (#4) of the treatment chamber. Rogowski coil #1 was placed at the front of titanium foil B and the coils #2, #3, and #4 were placed behind titanium foil B at a

distance of 5 mm, 35 mm, and 77 mm, respectively. The zooplanktons, *Artemia* larvae, were observed using a stereoscopic microscope. We assumed that the *Artemia* larvae that stop moving in one minute were inactivated because of irradiation.

Electron trajectories in the solution simulated using the CASINO [6] are also shown in Fig.2. The maximum penetration depth of 8 MeV electrons was found to reach 70 mm. Although the depth was reduced to 17 mm for 2 MeV electrons, the electrons spread over 30 mm. This indicates that the 2 MeV PIREB is suitable for treatment over a large area.

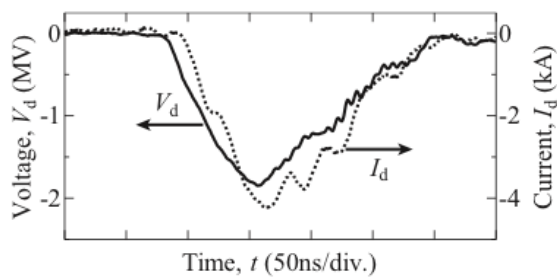


Fig.3 Typical voltage and current waveforms at diode

Figure 3 shows the typical time evolution of the electron-beam diode voltage V_d and current I_d . Results show that the V_d and I_d corresponding to the acceleration voltage and the beam current of the PIREB reach -2 MV and -4 kA within 70 ns.

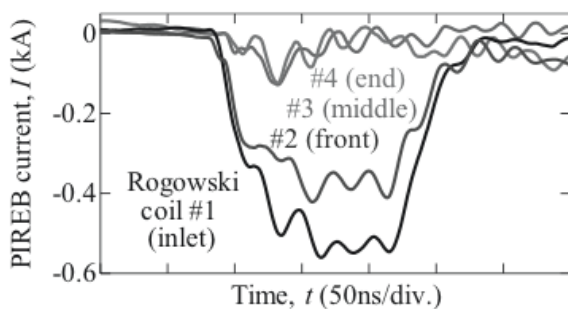


Fig.4 PIREB current in treatment chamber at various positions

Figure 4 shows the typical time evolution of the PIREB current in the treatment chamber at each depth. The results indicate that a PIREB with a

current of -0.55 kA was irradiated into the chamber. We also estimated that the current injected by the PIREB into the solution was more than -0.4 kA. Because the PIREB deposits energy within the solution, the current decreased drastically at the middle and end of the chamber.

The inactivation ratio is defined as (Number of inactivated *Artemia* / Total number of *Artemia*). 10 and 65 minutes correspond to the minimum time required for irradiation by using one and 10 shots of PIREB irradiation, respectively. Few *Artemia* larvae were inactivated without PIREB irradiation.

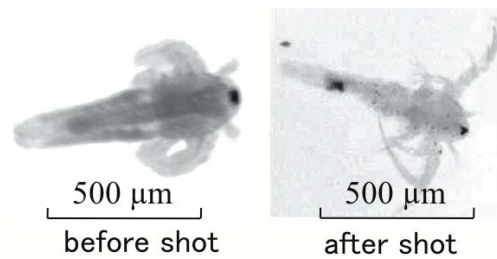


Fig.5 Example of *Artemia* larvae before irradiation (left) and after irradiation (right)

Figure 5 shows the example of the *Artemia* larvae before and after PIREB irradiations. The *Artemia* larvae move their legs actively and swim in the solution before irradiation, whereas the inactivated *Artemia* turn pale and stop moving after irradiation.

No increase in the inactivation ratio was found with one shot of PIREB irradiation compared to that without PIREB irradiation during 10 min. On the other hand, with 10 shots of PIREB irradiation, the inactivation ratio was in the range of 11-24 %. This indicates that the zooplanktons are successfully treated using PIREB irradiations.

The changes of pH of the solution are considered as one of the reasons for the inactivation mechanism. The *Artemia* larvae are incubated in salt water with pH of 5.5~5.9. After the irradiation of PIREB, pH of the solution was changed from 5.5~5.9 to 6.8~7.0. For this reason, we investigate the inactivation effect by the pH change to understand the mechanism.

Tables 1 and 2 show the inactivation ratios of the

Artemia larvae without PIREB irradiation in the solution at each time, respectively.

Table 1 Inactivation ratio of Artemia and pH of solution at each state of Artemia during 1 day

Incubation	pH of solution		Inactivation Ratio
	Throw-in	1 day	
5.5	7.0	7.1	18 %
5.5	7.0	7.4	17 %
5.5	7.0	7.3	23 %

Table 2 Inactivation ratio of Artemia and pH of solution at each state of Artemia during 10 minutes

Incubation	pH of solution		Inactivation Ratio
	Throw-in	10 min	
5.6	6.9	7.0	0 %
5.6	6.9	7.0	0 %
5.6	6.9	7.0	0 %

After the incubation, the Artemia larvae were thrown into the salt water of adjusted pH. We left the Artemia larvae unattended during 1 day or 10 minutes. Although, the Artemia larvae were inactivated after 1 day as shown in Table 1, the Artemia larvae did not be inactivated during 10 minutes as shown in Table 2. For this reason, pH changes did not affect to inactivate the Artemia larvae during the time scale of PIREB irradiation.

3. Reaction of Congo Red in Water after Irradiation by Pulsed Intense Relativistic Electron Beam

We demonstrated the degradation of congo red, a well-known toxic azo dye, by the PIREB treatment. Azo dyes are widely used in various products and leak out with industrial wastewater into the environment. Therefore, the development of a treatment technique for the removal or decomposition of azo dyes is very important.

Figure 6 shows the experimental setup. The electrons emitted from the cathode are accelerated by the applied voltage in the diode gap. The ring anode generates an electron beam with a hollow shape. Because the applied voltage is 2 MV in the diode gap

in a vacuum (0.02 Pa), PIREB can be extracted to the outside of the diode. PIREB travels through air space after passing through a Ti foil and irradiates 45 mL of a congo red aqution (0.10 mM) in a reactor containing Ti foil. The reactor was spatially isolated from the diode. To generate PIREB, we used the first acceleration cell of the pulsed power generator ETIGO-III, which is an electron induction accelerator.

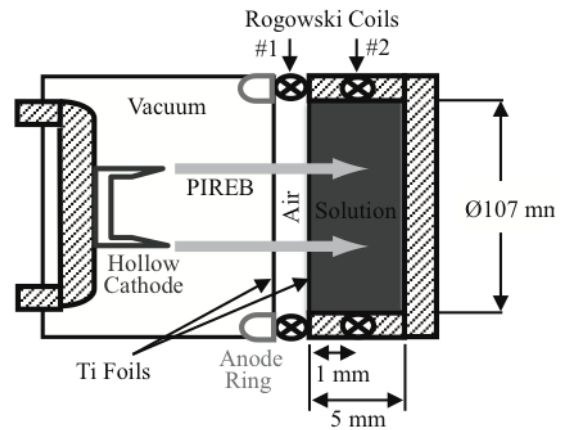


Fig.6 Experimental setup of PIREB irradiation of a reactor containing a congo red solution

Figures 7 and 8 show the typical voltage and beam current waveforms at the electron-beam diode and Rogowski coils, respectively. As shown in Fig.7, the voltage and current corresponding to the extraction voltage and the beam current of PIREB reached -2 MV and -4 kA at the diode, respectively. As shown in Fig.8, PIREB with a peak current of -0.36 kA entered the solution in the reactor.

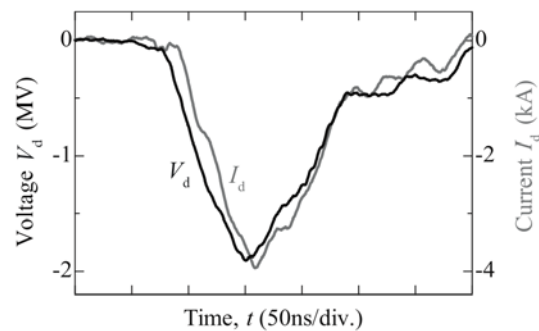


Fig.7 Typical waveforms of voltage and current at the diode

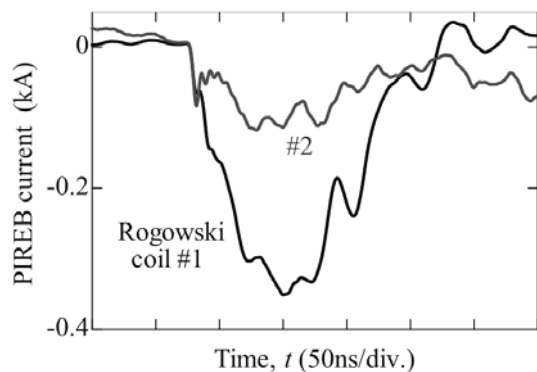


Fig.8 Typical waveforms of PIREB current detected at each Rogowski coil as shown in Fig.6

After PIREB irradiation, the congo red solution changed color from red to dark red. The color of a congo red aqutation is well known to deepen with decreasing pH. Therefore, the color change is believed to result from change in pH.

After irradiation, the solution was analyzed by electrospray ionization-mass spectrometry (ESI/MS) and liquid chromatography/mass spectrometry (LC/MS) in order to identify the reaction products and to quantify the amount of congo red, respectively. An LC/MS 2010A mass spectrometer (Shimadzu, Kyoto, Japan) was used for the ESI/MS measurement (negative ion mode). The ESI/MS conditions were as follows: scan range, m/z 100-800; heat block temperature, 200°C; interface voltage, 4.5 kV; CDL voltage, 20 V. The solutions (10 μ L) were injected into the LC/MS system; the flow rate of the mobile phase (acetonitrile) was 0.20 mL/min. In addition, the LC/MS 2010A instrument was used to quantify the amount of congo red. Amide-80 (Tosoh, Tokyo, Japan: 2.0 x 150 mm i.d.) was used for LC separation. High-performance LC separation was performed at 40°C using a gradient composed of solution A (6.5 mM ammonium acetate solution adjusted to pH 5.5) and solvent B (acetonitrile). The gradient conditions were as follows: 0-5 min, 100 % solvent B; 5-12 min, a linear decrease from 100 to 25 % B; 12-15 min, hold at 25 % B. The flow rate was 0.20 mL/min. The ESI conditions were the same as those described above. The reaction solutions were diluted 100 times

and injected into the LC/MS system. LC/MS acquisition was performed in the selected ion monitoring mode at m/z 325.

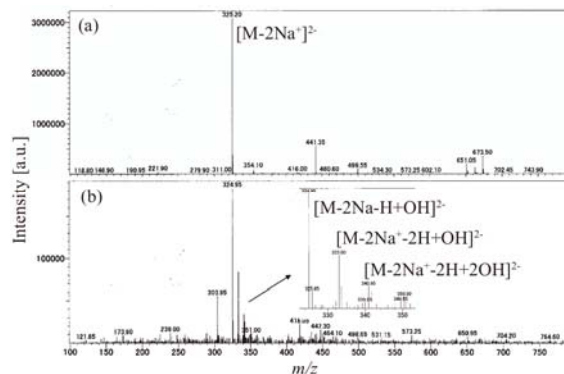


Fig.9 Mass spectrum of congo red solution before (a) and after (b) PIREB irradiation (five shots)

Figure 9 shows the ESI mass spectra of the solutions before and after PIREB irradiation (five shots). The ion peaks assignable to the hydroxylated compounds of congo red (the divalent ion of the monosubstituted compound, m/z 333; the divalent ion of the disubstituted compound, m/z 340) were observed by ESI/MS. The ion peaks corresponding to the products were not observed by ESI/MS in the positive ion mode. The hydroxylated compounds of congo red have reportedly been formed by gamma-ray irradiation [7]. Radiation-induced oxidative or reductive species such as OH radicals or aqueous electrons degraded congo red in the aqueous solution.

It is also well known that hydroxyl radicals are formed by the radiolysis of water [8]. Therefore, a similar reaction is believed to have occurred in the PIREB reaction. In addition, the absorption spectra of the congo red solution were measured before and after PIREB irradiation after adjusting the pH value to 6. The adjustment of pH was required because the color of the congo red solution changes with pH.

The peak at 500 nm was decreased by PIREB irradiation as shown in Fig.10. This result indicates that the π -electron conjugated system of congo red was broken by the attack of the reaction species formed by PIREB irradiation on the azo group of

congo red.

That is, it is possible that the products, which consist of the broken azo group and cannot be detected by ESI/MS, resulted from PIREB irradiation. The LC/MS results indicated congo red conversion rates of 45 % after one shot of PIREB irradiation and 77 % after five shots.

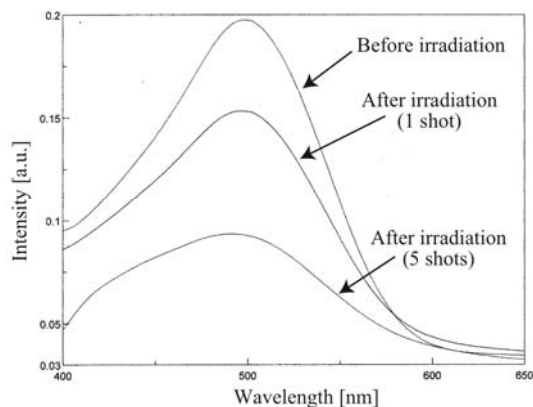


Fig.10 Changes in the UV spectra of congo red aqution after PIREB irradiation

4. Conclusions

In conclusion, we have demonstrated that the inactivation ratio of zooplankton can reach 24 % by firing 10 shots of PIREB irradiation. Increasing the inactivation ratio and elucidating the mechanism of the inactivation are the subjects of our future study. It is found that pH changes did not affect to inactivate the *Artemia* larvae during the time scale of PIREB irradiation.

A combined electron beam and biological treatment was previously used to purify dyeing wastewater [9]. In this report, we found that congo red was reacted by PIREB irradiation. PIREB irradiation is expected to be applied to the decomposition of azo dyes other than congo red and other environmental pollutants in water. However, there is no evidence that PIREB irradiation decreased the toxicity of the congo red solution. It is necessary to explore any change in the toxicity of the solution after PIREB irradiation in order to apply the technique to the decomposition of pollutants in water. In addition, downsizing of the PIREB irradiation equipment and reducing the initial cost of the

equipment are important problems for the widespread application of PIREB as an environmental technology.

References

- [1] G. Imada and K. Yatsui, *IEEE Trans. Plasma Sci.* 31, 295 (2003).; G. Imada, *IEEJ Trans.* 6, 88 (2011).
- [2] H. Moriwaki, et al., *J. Hazard. Mater.* 185, 725 (2011).
- [3] GloBallast, <http://globallast.imo.org/>
- [4] H. Kondo, et al., *Plasma Fusion Res.* 5, 036 (2010).
- [5] A. Tokuchi, et al., *Proc. 12th Int'l Conf. High Power Particle Beams*, (1998) p.175.
- [6] D. Drouin, et al., *Scanning* 29, 92 (2007).
- [7] H. Ma, et al., *Chemosphere* 68, 1098 (2007).
- [8] C. D. Jonah and J. R. Miller, *J. Phys. Chem.* 81, 1974 (1977).
- [9] B. Han, et al., *Radiat. Phys. Chem.* 64, 53 (2002).

Development of Exploding Wire Ion Source for Intense Pulsed Heavy Ion Beam Accelerator

Y. Ochiai, T. Murata, H. Ito, and K. Masugata

Department of Electrical and Electronic Engineering, University of Toyama,
3190 Gofuku, Toyama 930-8555, Japan

ABSTRACT

A Novel exploding wire type ion source device is proposed as a metallic ion source of intense pulsed heavy ion beam (PHIB) accelerator. In the device multiple shot operations is realized without breaking the vacuum. The basic characteristics of the device are evaluated experimentally with an aluminum wire of diameter 0.2 mm, length 25 mm. Capacitor bank of capacitance 3 μF , charging voltage 30 kV was used and the wire was successfully exploded by a discharge current of 15 kA, rise time 5.3 μs . Plasma flux of ion current density around 70 A/cm² was obtained at 150 mm downstream from the device. The drift velocity of ions evaluated by a time-of-flight method was 2.7×10^4 m/sec, which corresponds to the kinetic energy of 100 eV for aluminum ions. From the measurement of ion current density distribution ion flow is found to be concentrated to the direction where ion acceleration gap is placed. From the experiment the device is found to be acceptable for applying PHIB accelerator.

Key word; pulse power, intense pulsed ion beam, pulsed heavy ion beam, exploding wire, metallic ion source, aluminum ion source

1. Introduction

Intense pulsed heavy ion beam (PHIB) technology [1] is expected to be applied to materials processing including pulsed ion beam implantation, surface modification, and thin film deposition [1-5]. For those applications, it is very important to develop the accelerator technology to generate ion beams with various ion species. For the purpose we have developed various types of intense pulsed ion sources for the generation of

PHIB [1, 6, 7]. Gas puff plasma gun [6], vacuum arc ion source [7] and wire explosion ion sources. In those sources, wire explosion ion source [8] is very useful since the system is very simple and various ion species can be produced only by changing the wire. In our experiment, sufficiently high current density is obtained with good reproducibility. However, conventional wire plasma ion source can produce only one shot without braking the vacuum since the wire is evaporated in each shot.

In the paper we have proposed a new type of wire plasma ion source to realize the multi-shot operation without breaking the vacuum. The detail of the proposed ion source system is introduced with the results of preliminary experimental results of the characteristics of the ion source.

2. PHIB accelerator

Figure 1 shows the cross sectional view of the PHIB accelerator system used in our laboratory. [1, 6, 7] It consists of a high voltage pulsed power generator, an ion source of pulsed plasma gun, and a B_y type magnetically insulated acceleration gap (ion diode). The diode consists of a cylindrical anode of 60 mm ϕ and a cathode of grid structure. The gap length (d_{A-K}) is adjusted to 10 mm. Inside the anode active ion source is installed to supply

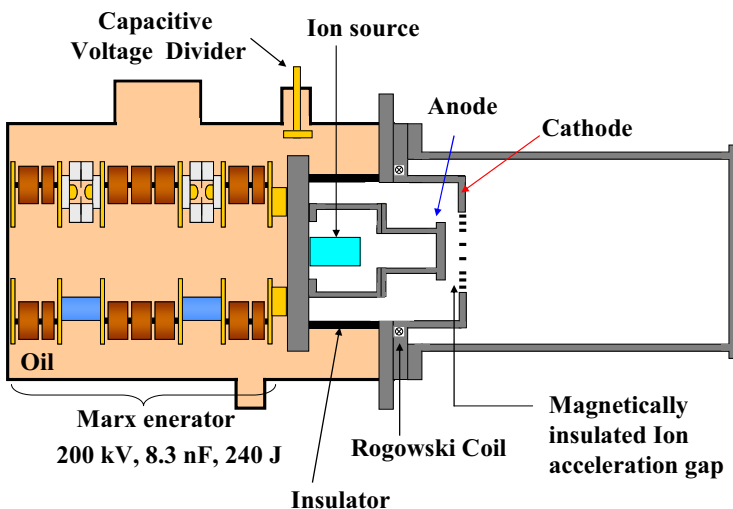


Fig.1. Schematic of the PHIB accelerator.

source plasma to the acceleration gap. The top of the anode has a punching board structure and the source plasma can penetrate to the A-K gap. The cathode acts a multi-turn magnetic field coil. The coil is powered by a capacitor bank of 250 μF , 5 kV and uniform, transverse magnetic field of 0.7 T is produced in the A-K gap, which insulate the electron flow.

A Marx generator of 200 kV, 240 J is used to apply the acceleration voltage. Typical diode voltage, diode current and pulse duration are 200 kV, 15 kA, 100 ns (FWHM), respectively.

Two types of pulsed plasma guns have been used to generate ion beams of nitrogen and aluminum. For nitrogen ion beam gas puff plasma gun is used, whereas for aluminum ions a vacuum arc discharge plasma gun is used, both of the guns we have successfully produced a PHIB of current density around 100 A/cm^2 . [6, 7]

Wire explosion ion source have also developed in our laboratory as the aluminum ion source. In the experiment more than 100 A/cm^2 of ion flux has been observed with good reproducibility. However, since repetitive operation is not realized, the ion source has not been installed in the accelerator.

3. Proposed ion source.

Figure 2 shows the proposed metallic wire plasma ion source to realize the multi-shot operation of plasma generation without breaking the vacuum. A Pair of 50 mm diameter metallic disk is used as a cathode whereas a rod electrode is used as an anode. The anode is placed in the center of the gap of cathode wheels. Between the cathode wheels thin wire of aluminum is strained in zigzag. Capacitor bank is connected between the cathode discs and the rod anode, which provide the discharge current.

The procedure of the plasma production is as follows; By rotating the cathode wheels, the anode rod contacts with the aluminum wire. Capacitor bank is discharged and the discharge current flows from the anode to the cathode wheels through the aluminum wire and both side of the wire is exploded and produces aluminum vapor. The vapor is beaked down and produces aluminum plasma. After the shot one pass of the wire disappears, however, by rotating the wheels, the cathode will contact to the next span of the wire. The wire will be automatically strained in the upstream of the wheels, which make possible the multiple shot operations without breaking the vacuum.

To develop the proposed plasma source we have evacuated the characteristics of the wire explosion ion source.

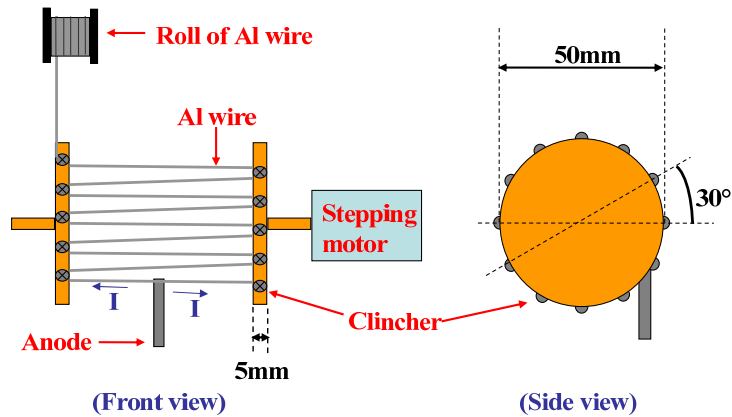


Fig.2 Schematic of wire explosion ion source proposed to realize multi-shot operation.

4. Experiment

A) Basic characteristics of wire explosion

To evaluate the basic exploding process of the wire explosion, single wire system is used. Capacitor bank of 1.0 μF 30 kV is used to explode the pure aluminum wire of 0.1 mm diameter, 30 mm in length.

Fig.3 shows the rise phase of the discharge current waveform. By the kilo-ampere of current flow, the wire is ohmic heated, melted and vaporized. After the vaporization the resistance between the electrode increases and the discharge current dips steeply. By the steep decrease of the current, inductive voltage is generated across the electrodes, providing the discharge in the aluminum vapor and the current again increases.

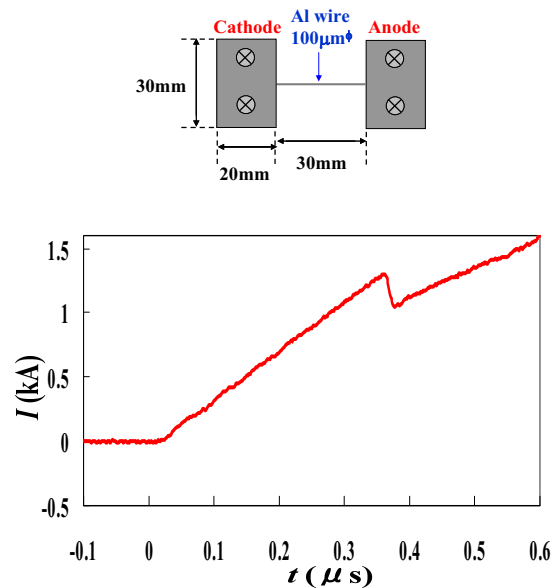


Fig.3(a). Experimental arrangement. (b) Discharge current waveform (the rising phase)

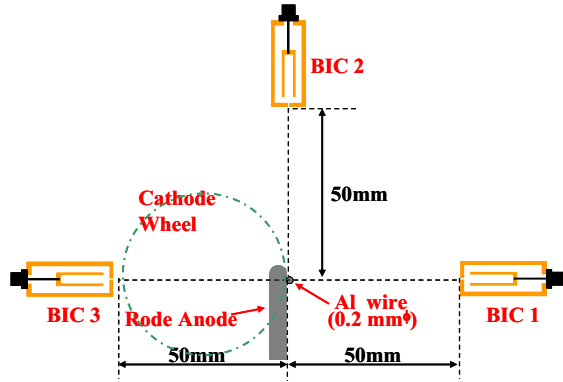


Fig. 4. Experimental setup to evaluate the ion current density distribution

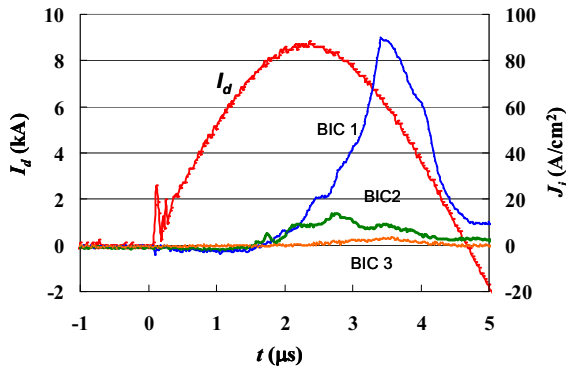


Fig. 5. Typical waveforms of discharge current and ion current density

The discharge current will heat the plasma and produces dense aluminum plasma.

B) Characteristics of the ion source

By using the ion source system described in section 2 we have evaluated the characteristics of produced plasma, as well as the discharge characteristics in repetitive operation. Capacitor bank of 1.0 μF , 30 kV is used with aluminum wire of 0.2 mm diameter. The separation between the cathode wheels was 20 mm; hence the wire length between the wheels is around 45 mm.

Figure 4 shows the experimental setup to evaluate the ion current density distribution of expanding plasma. Three Biased ion collectors (BIC1, BIC2, BIC3) are installed as shown in the figure to evaluate the ion current density distribution. The charging voltage of the capacitor bank was 30 kV in the experiment.

Figure 5 shows the typical waveform of discharge current (I_d) and ion current densities (J_i) observed by each BICs. As seen in the figure I_d rises in 2.3 μs and reaches the peak value of 8.8 kA. About 1.5 μs after the rise of I_d , J_i begin to be observed. Assuming that the

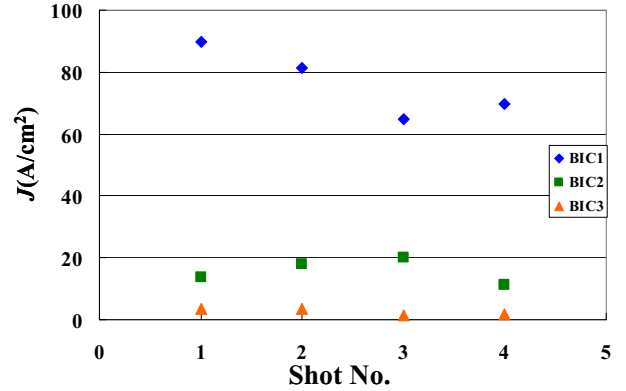


Fig. 6. History of the peak values of J_i measured by the three BICs. For four of continuous shot was evaluated.

plasma begins to expand at $t = 0$, the expansion velocity of the plasma is estimated to be 3.3×10^4 m/s. If assuming the aluminum plasma the kinetic energy of the ions is estimated to be 150 eV.

For BIC1, J_i rises in 2 μs and obtained a peak value of 90 A/cm^2 , whereas in BIC2 and BIC3, the peak values were 13.6 A/cm^2 and 3.6 A/cm^2 , respectively. The result suggests that the plasma is mainly expands to the front side of the ion source. This un-isotropic expansion is considered to be caused by the magnetic pressure produced by the discharge current.

Figure 6 shows the history of the peak values of J_i in each shot. From the figure we confirmed the reproducibility of the ion source.

Figure 7 shows the experimental arrangement to evaluate the transport of the plasma to the acceleration gap of the PHIB diode. Three BICs are used to evaluate the ion current density at 150 mm downstream from the ion source. The arrangement of the ion source was same as that shown in Fig. 4, however, to enhance the ion flux to the downstream, capacitor bank of 3.3 μF was used, which was charged to 30 kV

Figure 8 shows the results of the experiment. As seen in the figure, discharge current (I_d) rises in 5 μs and the peak current of 15 kA is obtained. The ion current

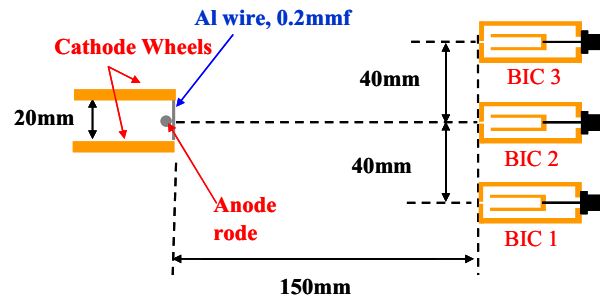


Fig. 7. Experimental arrangement.

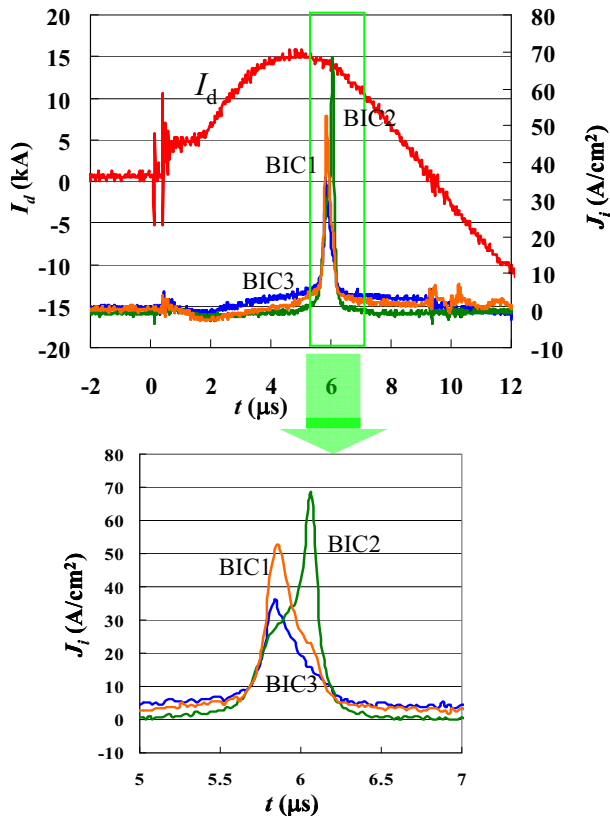


Fig.8. Typical waveforms of discharge current and ion current density

densities (J_i) observed in 3 BICs rise at $t = 5.5 \mu\text{s}$ and have a peak at t around $6 \mu\text{s}$. From the time of flight delay the drift velocity of the plasma is estimated to be $2.7 \times 10^4 \text{ m/s}$, which corresponds to the kinetic energy of 100 eV for aluminum atoms. The peak values of J_i are 36 A/cm^2 , 69 A/cm^2 and 53 A/cm^2 for BIC1, BIC2 and BIC3, respectively.

5. Conclusion

An exploding wire type of intense pulsed metallic ion source device is proposed as the ion source of HPIB accelerator. In the device multiple shots operation is realized without breaking the vacuum. Characteristics are evaluated experimentally using thin aluminum wire. The device is successfully operated with acceptable reproducibility. Plasma flux of ion current density around 70 A/cm^2 was obtained at 150 mm downstream from the device. The drift velocity of ions evaluated by a time-of-flight method was $2.7 \times 10^4 \text{ m/sec}$, which corresponds to the kinetic energy of 100 eV if assuming aluminum ion beam. From the measurement of ion current density distribution ion flow is found to be concentrated to the direction where ion acceleration gap is placed.

Acknowledgments

This work is supported from the ministry of Education, Science, Sports and culture, Japan.

References

- [1] K. Masugata and H. Ito, Intense pulsed heavy ion beam technology, The Trans. of IEE of Japan, A, 130(10) pp.879-884 (2010)
- [2] H A. Davis, G. E. Remnev, R. W. Stinnett and K. Yatsui, Mater.Res.Bull. **21**, 58 (1996).
- [3] H. Akamatsu, Y. Tanihara, T. Ikeda, K. Azuma, E. Fujikawa and M. Yatsuzuka, Jpn. J. Appl. Phys., **40**, 1083 (2001).
- [4] C. A. Meli, K. S. Grabowski, D. D. Hinshelwood, S. J. Stephanakis, D.J. Rej and W.J. Wagnaar, J.Vac.Sci. Technol. **A13**, 1182(1995).
- [5] K.Masugata, et al., Proc. 25th Int. Power Modulator Symposium, 2002 (Hollywood, CA, USA, 2002) pp.552-555.
- [6] H. Ito, H. Miyake and K. Masugata, Diagnosis of high-intensity pulsed heavy ion beam generated by a novel magnetically insulated diode with gas puff plasma gun, Rev. Sci. Instrum. **79**, 103502 (2008).
- [7] H. Ito, K. Fujikawa, H. Miyake and K. Masugata, Characteristic observation of intense pulsed aluminum ion beam in magnetically insulated ion diode with vacuum arc ion source, IEEE Transactions on Plasma Science **37**, pp.1879-1884 (2009).
- [8] I. I. Beilis, A. Shashurin, R. B. Baksht, and V. Oreshkin, Density and temperature distributions in the plasma expanding from an exploded wire in vacuum, Journal of applied physics **105**, 033301 (2009)